VILNIUS UNIVERSITY

Jūras Mickevičius

CARRIER RECOMBINATION IN WIDE-BAND-GAP NITRIDE SEMICONDUCTORS

Doctoral thesis
Physical Sciences, Physics (02 P), Semiconductor Physics (P 265)

Vilnius, 2009

The research work has been carried out in 2005-2009 at the Semiconductor Physics Department and Institute of Applied Research, Vilnius University.

Scientific supervisor:

Prof. Habil. Dr. Gintautas Tamulaitis (Vilnius University, Physical Sciences, Physics 02 P, Semiconductor Physics P 265)

VILNIAUS UNIVERSITETAS

Jūras Mickevičius

KRŪVININKŲ REKOMBINACIJA PLAČIATARPIUOSE NITRIDINIUOSE PUSLAIDININKIUOSE

Daktaro disertacija
Fiziniai mokslai, fizika (02 P), puslaidininkių fizika (P 265)

Vilnius, 2009

Disertacija rengta 2005-2009 metais Vilniaus universiteto Puslaidininkių fizikos katedroje bei Taikomųjų mokslų institute.

Mokslinis vadovas:

Prof. Habil. Dr. Gintautas Tamulaitis (Vilniaus universitetas, fiziniai mokslai, fizika – 02 P, puslaidininkių fizika – P 265)

Reziumė

III-grupės nitridiniai puslaidininkiai yra plačiai tyrinėjami pastaruosius du dešimtmečius. Tokį didelį susidomėjimą lėmė svarbūs praktiniai nitridinių puslaidininkių taikymai optoelektronikoje, ypač gaminant šviesos šaltinius, spinduliuojančius mėlynojoje ir ultravioletinėje spektro srityse bei saulės neakinamus fotojutiklius.

Šiuo metu InGaN junginių pagrindu sukurti mėlyni šviestukai jau gaminami masiniu būdu, o pagrindinis mokslinių tyrimų dėmesys krypsta link ultravioletinėje spektrinėje srityje veikiančių optoelektroninių prietaisų. Nepaisant didelių pastangų, tebelieka neišspręsta nemažai fundamentinių problemų, susijusių su nepusiausvyrųjų krūvininkų spinduline bei nespinduline rekombinacija, lokalizacijos bei vidinio elektrinio lauko įtaka krūvininkų rekombinacijos dinamikai.

Šis darbas yra skirtas eksitonų bei krūvininkų rekombinacijos dinamikos tyrimams plačiatarpiuose GaN ir AlGaN junginiuose plačiose temperatūros bei žadinimo galios tankio ribose. Nepusiausvirųjų krūvininkų dinamikai tirti buvo naudojami fotoliuminescencijos ir fotoliuminescencijos su laikine skyra spektroskopiniai metodai, taip pat šviesa indukuotų dinaminių gardelių bei liuminescencijos gesimo trukmės matavimų su dažnine skyra metodikos. Kelių skirtingų eksperimentinių metodikų naudojimas tiriant tą patį objektą leido išplėsti matavimų ribas bei susieti skirtingus medžiagos parametrus, šitaip giliau atskleidžiant krūvininkų dinamikos medžiagoje ypatumus.

Tyrinėjant GaN epitaksinius sluoksnius, buvo nagrinėjamos kelios problemos. Pastebėta koreliacija tarp geltonosios liuminescencijos juostos intensyvumo ir krūvininkų gyvavimo trukmės leidžia susieti geltonosios liuminescencijos juostą su struktūriniais medžiagos defektais: teigiame, kad dislokacijų ir priemaišų sudaryti kompleksai sąlygoja tiek spindulinę, tiek nespindulinę rekombinaciją. Krūvininkų dinamika GaN sluoksniuose buvo

tiriama, esant dviem ribiniams sužadinimų atvejams – labai žemų ir aukštų. Aukštų sužadinimų atveju buvo pasiūlytas naujas liuminescencijos gesimo interpretavimo metodas – gesimo kinetikos aprašymas biekspontentine funkcija, kurios charakteringos trukmės yra lygios krūvininkų gyvavimo trukmei, nustatytai dinaminių gardelių metodika, bei pusei jos. Buvo parodyta, kad panašios kokybės GaN bandiniuose didesnis krūvininkų judrumas sąlygoja mažesnę gyvavimo trukmę, kadangi krūvininkai greičiau pasiekia prie dislokacijų esančius nespindulinės rekombinacijos centrus. Buvo nustatytos aukštos optinio stiprinimo koeficiento vertės GaN sluoksniuose bei aptarti eksperimentinės kintamo ilgio juostelės metodikos ypatumai. Krūvininkų dinamikos labai žemų sužadinimų sąlygomis tyrimai atskleidė skirtingų rekombinacijos mechanizmų konkurenciją.

AlGaN sluoksnių su skirtinga aliuminio koncentracija tyrimai parodė, kad ir AlGaN sluoksniuose krūvininkų gyvavimo trukmė yra nulemta krūvininkų difuzijos link dislokacijų, kur įvyksta nespindulinė rekombinacija. Tuo tarpu spindulinės rekombinacijos sparta priklauso nuo aliuminio koncentracijos sluoksnyje, tačiau yra pastovi, esant tai pačiai AlGaN sluoksnio sudėčiai, bet skirtingam dislokacijų tankiui jame. Buvo atliktas dviejų tos pačios sudėties sluoksnių, augintų skirtingomis technologijomis, palyginimas, lyginant krūvininkų gyvavimo trukmes bei juostos potencialo fliuktuacijų profilį. Potencialo fliuktuacijų profilis buvo įvertintas, naudojant eksitonų šokavimo Monte Karlo modeliavimą ir jo rezultatus tapatinant su eksperimentiniais duomenimis. Modeliavimas parodė, kad juostos potencialo fliuktuacijų profilis nepriklauso nuo auginimo technologijos, o krūvininkų gyvavimo trukmės skirtumas yra nulemtas vien tik nespindulinės rekombinacijos centrų tankio skirtumo.

Krūvininkų dinamikos daugialakštėse AlGaN/AlGaN kvantinėse duobėse tyrimai atskleidė stiprią vidinio elektrinio lauko ekranavimo bei krūvininkų lokalizacijos įtaką. Buvo atskirti šių procesų indėliai į liuminescencijos gesimo spartą. Parodyta lokalizacijos įtaka krūvininkų gyvavimo trukmės priklausomybei nuo kvantinės duobės pločio.

Acknowledgments

I would like to thank my supervisor Prof. Gintautas Tamulaitis for the shown trust and given opportunity to work in the field of III-nitrides.

Also I wish to thank Prof. Artūras Žukauskas for the possibility to do the research work in the Institute of Applied Research.

I acknowledge doctors Karolis Kazlauskas and Ramūnas Aleksiejūnas for valuable advices and sharing their experience on measurement equipment and experimental techniques.

My best thanks to all my colleagues for help and friendly atmosphere at the Institute.

Finally, I would like to thank my family and girlfriend for their encouragement, care and support in my everyday life.

This work has been supported by the Lithuanian State Science and Study Foundation.

Table of Contents

List of abbreviations

BEL	band-edge luminescence
BGR	band gap renormalization
BL	blue luminescence (band)
CW	continuous wave
DAP	donor-acceptor pair
EHP	electron-hole plasma
ELO	epitaxial lateral overgrowth
FDLM	frequency domain luminescence lifetime measurements
FWM	four wave mixing
HVPE	hydride vapor phase epitaxy
LED	light-emitting diode
LITG	light-induced transient grating (technique)
LT	low-temperature (buffer)
MELEO	migration enhanced lateral epitaxial overgrowth
MEMOCVD™	migration enhanced MOCVD
MOCVD	metal-organic chemical vapor deposition
MQW	multiple quantum well
NBE	near-band-edge (luminescence)
PALE	pulsed atomic layer epitaxy
PL	photoluminescence
QCSE	quantum-confined Stark effect
SE	stimulated emission
TRPL	time-resolved photoluminescence
UV	ultraviolet
UVL	ultraviolet luminescence (band)
VSL	variable stripe length (technique)
YL	yellow luminescence (band)

Introduction

The group-III nitride semiconductor alloys have been widely investigated during the last two decades due to their exceptional material properties. These wide-band-gap materials form the basis, upon which the optoelectronic devices, emitting light in blue to UV spectral regions, visible- and solar-blind photodetectors, high-power and high-temperature electronic devices are developed.

Currently, the blue InGaN-based light-emitting diodes (LEDs) have already been successfully commercialized, and the main emphasis in III-nitride research has shifted to UV optoelectronic devices. The UV LEDs are required for a large number of applications in a variety of fields: detection of hazardous biological and chemical agents, water-and-air purification, short-range covert communication, high-efficiency lighting, and high-density optical data storage.

Despite the large interest in nitride materials, their further development needs a deeper understanding of physical origins of structural, electrical and optical properties. There still exist fundamental problems concerning radiative and nonradiative recombination of nonequilibrium carriers, their localization, and the influence of the built-in electric fields in heterostructures.

The successful commercialization of nitride-based devices relies on novel techniques developed for growth of epitaxial layers and quantum structures. The improving material quality allows investigating the intrinsic properties of the material. However, even now several of the old issues are still not resolved. In particular, the origin of the famous yellow luminescence band in GaN and its relation to the structural defects is still unanswered. On the other hand, the improving material quality raises new questions: the increasing lifetime of nonequilibrium carriers is related to the nonexponentiality of the luminescence decay, and the interpretation on carrier dynamics becomes ambiguous.

While the GaN and AlGaN epilayers have been widely investigated, there is a lack of studies on AlGaN quantum structures, in particular, AlGaN/AlGaN multiple quantum wells (MQWs) with high aluminum content, which are necessary for deep-UV devices. The low quantum efficiency of such devices requires a deeper understanding of the carrier dynamics in AlGaN/AlGaN structures, which is affected both by carrier localization and built-in electric field.

The experimental work in this thesis is based on optical characterization methods. The combination of several experimental techniques allowed extending the measurement ranges and also provided an opportunity to correlate different material properties, thus, getting deeper insight into carrier dynamics in these materials.

Main goals

The thesis is aimed at gaining new knowledge on exciton and carrier dynamics in GaN and AlGaN epilayers and their quantum structures. The experimental studies that were performed by means of photoluminescence (PL) and time-resolved PL (TRPL) spectroscopy, light-induced transient grating (LITG) technique, and frequency domain lifetime measurements (FDLM) are targeted at extracting important parameters characterizing carrier/exciton dynamics in GaN and AlGaN alloys.

Main objectives

1. To reveal the correlation between yellow luminescence intensity and nonequilibrium carrier lifetime in GaN epilayers.
2. To suggest a method for interpreting TRPL decay kinetics by linking PL and LITG transients.
3. To apply FDLM technique for investigation of carrier dynamics in GaN epilayer under extremely low excitations.

4. To evaluate the optical gain coefficient in high-quality GaN by using variable stripe length technique for comparative characterization of different GaN samples.
5. To distinguish the influence of band potential profile fluctuations and density of nonradiative recombination centers on carrier dynamics in AlGaN epilayers grown by different techniques.
6. To investigate the influence of carrier localization and built-in electric field on carrier dynamics in AlGaN/AlGaN MQWs.
7. To confirm the MEMOCVD^{TM} growth technique as a novel method for improving material quality of GaN and AlGaN.

Novelty and importance of the thesis

Even though there are already commercially available devices based on GaN and related alloys, the interest in this materials group is still high. The research direction has slightly shifted the focus towards the GaN-AlGaN material system and deep-UV devices, however, the constant improvement of layer growth technology allow reviewing some of the previously established material properties as well as getting deeper understanding of processes taking place in these materials.

Combination of various characterization techniques (photoluminescence, time-resolved PL, light-induced transient grating, and frequency domain luminescence lifetime measurements) and new high-quality materials and structures (GaN epilayers, AlGaN epilayers, AlGaN/AlGaN structures) provided by world-wide leading companies, ensured an extensive experimental basis for our study. Investigations of GaN epilayers under extremely low excitation conditions enabled to look deeper in carrier dynamics when different recombination channels are not saturated. Also the new approach for studies of yellow band in GaN was shown by linking the carrier lifetime with yellow band intensity. A new method for interpreting PL decay kinetics was suggested by interrelating PL and LITG transients. Two AlGaN epilayers grown by

different novel growth techniques were compared and the factors limiting carrier lifetime were identified. Moreover, more evidence on alloy mixing and band potential fluctuations in AlGaN was provided by our study. Also, essential knowledge was attained about carrier dynamics in high-Al-content AlGaN/AlGaN multiple quantum well structures, which are the key structures for the laser diodes and light-emitting diodes operating in deep-UV spectral region. Most of the samples under study were grown by MEMOCVD^{TM} growth technique, and our study confirmed the high potential of this innovative growth technique for improving material quality.

The points to be maintained

1. Carrier lifetime in GaN epilayers with similar dislocation densities is shorter in the epilayers with higher carrier mobility, which results in faster reaching the nonradiative recombination centers at dislocations.
2. The carrier lifetime in AlGaN is primarily limited by the carrier travel to the dislocations, where the nonradiative recombination occurs. The carrier lifetime is determined not by band gap fluctuations, but by the density of nonradiative recombination centers.
3. The fast initial component in PL intensity decay of AlGaN/AlGaN MQWs is caused by vanishing screening of the built-in electric field, which recovers with decreasing nonequilibrium carrier density. The slow decay component is determined by recombination of localized carriers with the localization due to well width fluctuations. The lifetime of localized carriers decreases with increasing well width due to decreasing potential fluctuations.
4. MEMOCVD^{TM} growth technique enabled the growth of high-quality GaN epilayers on sapphire exhibiting carrier lifetimes up to 2 ns at room temperature, and optical gain values as high as ~7500 cm^{-1}, and AlGaN epilayers on sapphire with increased PL intensity (by a factor of 6) and

carrier lifetime (by a factor of 6.5), compared to the epilayers grown by conventional MOCVD.

Layout of the thesis

The thesis is organized as follows. In chapter 1, an overview of some basic GaN and AlGaN materials properties is presented. Some more advanced issues such as yellow band, stimulated emission and optical gain in GaN, and carrier dynamics in GaN and AlGaN are discussed in more detail.

In chapter 2, the experimental setups used for optical characterization of the samples under study are described. These include photoluminescence under continuous wave and pulsed excitation, time-resolved PL, light-induced transient grating technique, and frequency domain luminescence lifetime measurements.

Chapter 3 deals with the investigations of carrier dynamics in GaN epilayers. Several problems on the optical properties of GaN are discussed: first, the yellow luminescence band in GaN and its relation with the nonequilibrium carrier lifetime is studied; second, the carrier dynamics in GaN under high excitation and extremely low excitation conditions are discussed; third, the optical gain in GaN epilayers is analyzed.

In chapter 4, the carrier dynamics in AlGaN epilayers with different aluminum content is investigated. The carrier lifetime dependence on aluminum content in epilayer is discussed. Two AlGaN epilayers with the same aluminum content but grown by different techniques are compared, and band gap fluctuation profile in them is analyzed. The factors limiting the lifetime of nonequilibrium carriers are discussed.

Chapter 5 deals with the study of carrier dynamics in AlGaN/AlGaN multiple quantum wells. A set of structures with different well width is investigated and the dependence of carrier lifetime on well width is demonstrated. The investigation of photoluminescence dynamics in quantum wells are supported by theoretical calculations of the potential profile in the

quantum well, which have been carried out by taking into account the built-in field screening and many-body effects.

The thesis is finalized with a concluding summary.

The results presented in the thesis were obtained in the Luminescence research group at the Institute of Materials Science and Applied Research, Vilnius University, leaded by Prof. A. Žukauskas, and at Prof. M. S. Shur‘s group at Rensselaer Polytechnic Institute, Troy, New York, USA. All of the experimental work presented here was performed by the author, except for the results obtained using frequency domain lifetime measurements. The investigations were performed on the samples provided by Sensor Electronic Technology, Inc. (Columbia, South Carolina, USA). The further analysis of experimental results was done by the author. The interpretation was discussed with the thesis advisor Prof. G. Tamulaitis. Most of the paper manuscripts were prepared by the author of the thesis.

All the presented results were also presented at international conferences and summer schools, and later published in conference proceedings and/or international journals.

List of publications related to the thesis

List of papers related to the thesis

P1. **J. Mickevičius**, R. Aleksiejūnas, M. S. Shur, S. Sakalauskas, G. Tamulaitis, Q. Fareed, and R. Gaska, Correlation between yellow luminescence intensity and carrier lifetimes in GaN epilayers, Appl. Phys. Lett. **86**, 041910 (2005).

P2. **J. Mickevičius**, R. Aleksiejūnas, M.S. Shur, G. Tamulaitis, R.S.Q. Fareed, J.P. Zhang, R. Gaska, and M.A. Khan, Lifetime of nonequilibrium carriers in high-Al-content AlGaN epilayers, phys. stat. sol. (a) **202**, 126-130 (2005).

P3. K.Kazlauskas, A.Žukauskas, G.Tamulaitis, **J.Mickevičius**, M.S.Shur, R.S.Qhalid Fareed, J.P.Zhang, and R.Gaska, Exciton hopping and nonradiative decay in AlGaN epilayers, Appl. Phys. Lett. **87**, 172102 (2005).

P4. **J.Mickevičius**, M.S.Shur, R.S.Qhalid Fareed, J.P.Zhang, R.Gaska, G.Tamulaitis, Time-resolved experimental study of carrier lifetime in GaN epilayers, Appl. Phys. Lett. **87**, 241918 (2005).

P5. G.Tamulaitis, **J.Mickevičius**, M.S.Shur, R.S.Qhalid Fareed, J.P.Zhang, R.Gaska, Carrier lifetime and diffusion in GaN epilayers grown by MEMOCVDTM, phys. stat. sol. (c) **3**, 1923 (2006).

P6. **J.Mickevičius**, G.Tamulaitis, M.S.Shur, Q.Fareed, J.P.Zhang, R.Gaska, Saturated gain in GaN epilayers studied by variable stripe length technique, J. Appl. Phys. **99**, 103513 (2006).

P7. K.Kazlauskas, G.Tamulaitis, A.Žukauskas, **J.Mickevičius**, M.S.Shur, R.S.Qhalid Fareed, J.P.Zhang, R.Gaska, Study of exciton hopping in AlGaN epilayers by photoluminescence spectroscopy and Monte Carlo simulation, Lithuanian Journal of Physics, **46**, 73 (2006).

P8. G.Tamulaitis, **J.Mickevičius**, P.Vitta, A.Žukauskas, M.S.Shur, Q.Fareed, R.Gaska, Time- and frequency-domain measurements of

carrier lifetimes in GaN epilayers, Superlattices and Microstructures **40**, 274 (2006).

P9. **J.Mickevičius**, G.Tamulaitis, E.Kuokštis, K.Liu, M.S.Shur, J.P.Zhang, R.Gaska, Well-width-dependent carrier lifetime in AlGaN/AlGaN quantum wells, Appl. Phys. Lett. **90**, 131907 (2007).

P10. **J.Mickevičius**, G.Tamulaitis, P.Vitta, A.Žukauskas, M.S.Shur, J.Zhang, J.Yang, R.Gaska, Carrier dynamics in GaN at extremely low excited carrier densities, Solid State Communications **145**, 312 (2008).

P11. **J.Mickevičius**, P.Vitta, G.Tamulaitis, A.Žukauskas, M.S.Shur, J.Zhang, J.Yang, R.Gaska, Luminescence decay kinetics in GaN studied by frequency domain measurements, Acta Physica Polonica A **113**, 833 (2008).

P12. **J.Mickevičius**, G.Tamulaitis, E.Kuokštis, M.S.Shur, J.Yang, R.Gaska, Influence of electric field and carrier localization on carrier dynamics in AlGaN quantum wells, Acta Physica Polonica A **114**, 1247 (2008).

P13. G.Tamulaitis, **J.Mickevičius**, E.Kuokštis, K.Liu, M.S.Shur, J.P.Zhang, R.Gaska, Carrier dynamics in wide-band-gap AlGaN/AlGaN quantum wells, physica status solidi (c), **5**, 2096 (2008)

P14. G.Tamulaitis, **J.Mickevičius**, K.Kazlauskas, A.Žukauskas, E.Kuokštis, M.S.Shur, J.Yang, R.Gaska, Carrier localization and decay in wide-band-gap AlGaN/AlGaN quantum wells, AIP Proceedings (accepted)

P15. **J.Mickevičius**, E.Kuokštis, V.Liuolia, G.Tamulaitis, M.S.Shur, J.Yang, and R.Gaska, Photoluminescence dynamics of AlGaN quantum wells with built-in electric fields and localized states, physica status solidi (a) (accepted).

List of conference contributions related to the thesis

C1. G. Tamulaitis, **J. Mickevicius**, R. Aleksiejunas, M. S. Shur, J. P. Zhang, Q. Fareed, R. Gaska, Dislocation-limited lifetime of nonequilibrium carriers in AlGaN epilayers, Program of the 27th

International Conference on the Physics of Semiconductors (ICPS-27), July 26-30, 2004, Flagstaff, AZ, USA, p. 357.

C2. **J. Mickevicius**, R. Aleksiejunas, M. S. Shur, J. P. Zhang, Q. Fareed, R. Gaska, G. Tamulaitis, Lifetime of nonequilibrium carriers in AlGaN epilayers with high Al molar fraction, Abstract Book of the 2004 IEEE Lester Eastman Conference on High Performance Devices, August 4-6, 2004, Troy, NY, USA, p. 61.

C3. G.Tamulaitis, K.Kazlauskas, A.Žukauskas, **J.Mickevičius**, M.S.Shur, R.S.Qhalid Fareed, J.P.Zhang, R.Gaska, Study of exciton hopping in AlGaN epilayers by photoluminescence spectroscopy and Monte Carlo simulation, Abstract Book of the 6th International Conference on Nitride Semiconductors (ICNS-6), August 28-September 2, 2005, Bremen, Germany.

C4. G.Tamulaitis, **J.Mickevičius**, M.S.Shur, R.S.Qhalid Fareed, J.P.Zhang, R.Gaska, Carrier lifetime and diffusion in GaN epilayers grown by MEMOCVD^{TM}, Abstract Book of the 6th International Conference on Nitride Semiconductors (ICNS-6), August 28-September 2, 2005, Bremen, Germany.

C5. G.Tamulaitis, **J.Mickevičius**, M.S.Shur, Q. Fareed,.P.Zhang, R.Gaska, Study of optical gain in thick GaN epilayers by variable stripe length technique, Materials research society (MRS) symposium proceedings, Rare-earth doping for optoelectronic applications. ISSN 0272-9172. 2005, vol. 866, p. 125-130.

C6. K.Kazlauskas, G.Tamulaitis, A.Žukauskas, **J.Mickevičius**, M.S.Shur, Q.Fareed, J.P.Zhang, R.Gaska, Eksitonų šokavimo AlGaN sluoksniuose tyrimas fotoliuminescencinės spektroskopijos ir Monte Carlo modeliavimo pagalba, 36-oji Lietuvos nacionalinė fizikos konferencija (LNFK-36) : programa ir pranešimų tezės, Vilnius, 2005 m. birželio 16-18. ISBN 9986-9284-5-1. Vilnius, 2005, p. 64.

C7. G.Tamulaitis, **J.Mickevičius**, P.Vitta, A.Žukauskas, M.S.Shur, Q.Fareed, J.P.Zhang, R.Gaska, Time- and frequency-domain measurements of carrier lifetimes in GaN epilayers, European Materials Research Society 2006 Spring Meeting (E-MRS 2006), May 29-June 2, 2006, Nice, France.

C8. P.Vitta, A.Žukauskas, **J.Mickevičius**, G.Tamulaitis, M.S.Shur, Q.Fareed, J.P.Zhang, R.Gaska, Carrier dynamics in GaN epilayers revealed by time- and frequency-domain measurements, Blue lasers and light emitting diodes: the 6th international symposium (ISBLLED 2006): programme and abstract book. May 15-19, 2006, Montpellier, France, p. 72.

C9. G. Tamulaitis, **J. Mickevicius**, P. Vitta, M. S. Shur, Q. Fared, J. P. Zhang, R. Gaska, Study of yellow luminescence in GaN using photoluminescence spectroscopy in time and frequency domains, European Workshop on III-Nitride Semiconductor Materials and Devices (EW3NS), September 18-20, 2006, Heraklion, Crete, Grece, p.85.

C10. G. Tamulaitis, **J. Mickevičius**, P. Vitta, A. Žukauskas, M.S. Shur, K. Liu, Q. Fareed, J.P. Zhang, R. Gaska, Carrier Lifetimes in GaN Revealed by Studying Photoluminescence Decay in Time and Frequency Domains, Abstracts of 210th ECS 2006 Joint International Meeting, October 28 – November 3, 2006, Cancun, Mexico, p. 1314.

C11. **J.Mickevičius**, E.Kuokštis, G.Tamulaitis, M.S.Shur, J.Zhang, R.Gaska, Krūvininkų gyvavimo trukmė AlGaN/AlGaN kvantinėse duobėse, 37-oji Lietuvos nacionalinė fizikos konferencija (LNFK-37): programa ir pranešimų tezės, 2007 m. birželio 11-13, Vilnius

C12. **J.Mickevičius**, P.Vitta, G.Tamulaitis, A.Žukauskas, M.S.Shur, J.Zhang, J.Yang, R.Gaska, Luminescence decay kinetics in GaN studied by frequency domain measurements, Abstract Book of 13th International Symposium on Ultraphast Phenomena in Semiconductors (UFPS-13), August 26-29, 2007, Vilnius, Lithuania, p. 79.

C13. **J.Mickevičius**, G.Tamulaitis, E.Kuokštis, M.S.Shur, J.P.Zhang, R.Gaska, Carrier lifetime and its well-width dependence in AlGaN/AlGaN quantum wells, Abstract Book of the 9th International Conference-School „Advanced Materials and Technologies“, August 27-31, 2007, Palanga, Lithuania, p. 109.

C14. G.Tamulaitis, **J.Mickevičius**, E.Kuokštis, K.Liu, M.S.Shur, J.P.Zhang, R.Gaska, Carrier dynamics in wide-band-gap AlGaN/AlGaN quantum wells, Abstract Book of the 7th International Conference on Nitride Semiconductors (ICNS-7), September 16-21, 2007, Las Vegas, Nevada, USA.

C15. **J.Mickevičius**, G.Tamulaitis, K.Kazlauskas, A.Žukauskas, E.Kuokštis, M.S.Shur, J.Yang, R.Gaska „Influence of electric field and carrier localization on carrier dynamics in AlGaN quantum wells“. Pranešimas (stendinis) tarptautinėje konferencijoje: XXXVII International School on the Physics of Semiconducting Compounds, Jažovecas, Lenkija.

C16. G.Tamulaitis, **J.Mickevičius**, K.Kazlauskas, A.Žukauskas, E.Kuokštis, M.S.Shur, J.Yang, R.Gaska „Carrier localization and decay in wide-band-gap AlGaN/AlGaN quantum wells“. Pranešimas (stendinis) tarptautinėje konferencijoje: 29th International Conference on the Physics of Semiconductors (ICPS-29), Rio de Žaneiras, Brazilija.

C17. **J.Mickevičius**, G.Tamulaitis, E.Kuokštis, M.S.Shur, J.P.Zhang, R.Gaska „AlGaN quantum wells: electric field and carrier localization“. Pranešimas (stendinis) tarptautinėje konferencijoje: 10th International School-Conference Advanced Materials and Technologies, Palanga, Lietuva.

C18. **J.Mickevičius**, E.Kuokštis, V.Liuolia, G.Tamulaitis, M.S.Shur, J.Yang, R.Gaska, „Carrier localization and built-in electric field in AlGaN/AlGaN quantum wells“. Pranešimas (žodinis) tarptautinėje konferencijoje: 15th Semiconducting and Insulating Materials Conference, Vilnius, Lithuania.

C19. **J.Mickevičius**, G.Tamulaitis, E.Kuokštis, V.Liuolia, M.S.Shur, J.Yang, R.Gaska, „Influence of built-in electric field and many-body effects on photoluminescence dynamics in AlGaN/AlGaN quantum wells“. Pranešimas (stendinis) tarptautinėje konferencijoje: XXXVIII International School on the Physics of Semiconducting Compounds, Jažovecas, Lenkija.

1. III-nitride material properties and device issues

Group III-nitrides (InN, GaN, AlN and their ternary and quaternary alloys) are a unique semiconductor alloy system with band gaps covering an extremely wide spectral range: from infrared (1600 nm InN) to near ultraviolet (365 nm GaN) to deep ultraviolet (200 nm AlN). Since all of these alloys have a direct band gap, they could be used to fabricate light-emitting devices operating at, in principle, any wavelength within this spectral range. The sub-series of the nitride system, $Al_xGa_{1-x}N$ ($x = 0 \div 1$) alloys, cover a wide region in UV from 365 nm down to 200 nm which makes them practically a rival-free choice of material for the development and fabrication of deep UV light emitters and photodetectors.

1.1. Basic properties of nitride materials

1.1.1. Growth issues

One of the main problems in growth of nitrides is their extreme melting conditions. Gallium nitride melts at high nitrogen pressure (6 GPa) and high temperature (2497 K) [1]. Due to such melting conditions of GaN, the nitrides cannot be grown from their stoichiometric melt by the standard Czochralski or Bridgman methods commonly used for Si or GaAs, and methods allowing lower pressures and temperatures have to be used. Small GaN crystals in the form of hexagonal platelets (up to 3 cm^2 in diameter) or needles (up to 1 cm in length) can be grown from the solution of atomic nitrogen in liquid gallium at high temperature (~2000 K) and high nitrogen pressure (~2 GPa). Such GaN crystals contain very low dislocation density (10-100 cm^{-2}) [2,3], and can be used as substrates for homoepitaxy of nitrides. However, the small crystal size and high production costs limit the use of GaN grown by high-pressure technologies.

Due to the lack of high-quality native substrates, nitride thin films and device structures are commonly grown on foreign substrates, a process known as heteroepitaxy. All foreign substrates differ in lattice parameters and thermal expansion coefficients from nitride materials. The lowest lattice mismatch with GaN is provided by ZnO (2% mismatch) and 6H-SiC (3.5% mismatch) crystals, however, most of the nitride technology has been developed using sapphire (Al_2O_3) substrates. The lattice mismatch between GaN and sapphire is ~15%, but its wide availability in high-quality, compatibility with high temperature growth, UV transparency and low cost results in sapphire being the preferred substrate for nitride growth. The SiC substrates, which have a higher thermal conductivity compared to sapphire, are commonly used for fabrication of high-power electronic devices, but are often not suitable for optoelectronic devices due to lack of UV transparency. The substrate UV transparency and high thermal conductivity could be combined by using AlN substrates, which would also provide an excellent lattice match to GaN and, especially, to AlGaN materials. The growth of bulk AlN with low dislocation density ($<10^4$ cm^{-2}) has been reported [4,5], however, again, the size and cost limit the use of these substrates so far.

The difference in lattice parameters and thermal expansion coefficient between substrate and epilayer results in formation of large density of threading dislocations (10^9-10^{11} cm^{-2}). This large density of dislocations in GaN drastically limits the performance and operating lifetime of nitride-based devices. Therefore, most of the technological efforts are directed to reduce these defects, and a variety of approaches has been developed.

The most widely used technique for growth of nitrides is metalorganic chemical vapor deposition (MOCVD) [6], while the standard growth of GaN is usually a multistep process, which includes nitridation of the substrate and/or deposition of a low-temperature (LT) buffer layer and heat treatment of this nucleation layer. Introduction of LT buffer layers at the first stage of growth has been shown to dramatically improve the quality of GaN epilayers already more than 20 years ago [7]. The optimization of buffer layer thickness and

growth conditions allowed reducing the dislocation density in GaN epilayers down to 10^7-10^8 cm^{-2} [8]. A further improvement was achieved by developing the epitaxial lateral overgrowth (ELO) technique, which enabled one to reduce dislocation densities down to 10^6 cm^{-2}. However, even the best material achieved using ELO provides limited area of defect-free material [8].

The growth of AlGaN has proved to be even more complicated compared with that of GaN [9]. The problem arises from the fact that Al adatoms have a much larger sticking coefficient than Ga adatoms. Because of that, the Al adatoms are much less mobile on the surface, and instead of incorporating at the most energetically favorable lattice sites such as a step, they tend to cause islands to nucleate, thus disturbing the epitaxial growth. As a result, higher densities of extended defects are easier to generate as these growth islands coalesce. In addition to formation of threading dislocations, nitride films also tend to bow and even crack [9]. The cracking evolves from the strain introduced by lattice mismatch, and since the LT buffer has proved to be very successful in reducing the strain [7], similar growth approaches were developed, based on the idea of compliant-layer insertion. The periodic insertion of LT-grown AlN or AlGaN layers was shown to effectively reduce the strain in the AlGaN films, thus reducing cracking [10,11], however, this method was argued to introduce dislocations after insertion of each LT-layer, while there are also too many thermal cyclings during one growth [10]. Another approach was suggested to reduce the strain by using superlattice buffers. The theoretical calculations of GaN/AlN and GaN/AlGaN superlattices [12], and experimental results on use of AlN/AlGaN superlattices [13] confirmed that these superlattices are efficient in increasing AlGaN material quality.

The quality of AlGaN epilayers was also improved by developing new growth techniques based on pulsed introduction of group III and group V precursors: pulsed atomic layer epitaxy (PALE) [14,15] and its further upgrade – migration-enhanced MOCVD (MEMOCVD^{TM}) [16-18]. Using these growth techniques, the precursors are sequentially modulated, thus enhancing

the surface migration of Al and Ga adatoms. While the duration of each pulse and succession of pulses are fixed in PALE, in MEMOCVD^{TM} growth technique, the duration and waveforms of precursor pulses are optimized and the pulses overlap, thus allowing for a continuum of growth techniques ranging from PALE to conventional MOCVD.

The advantages of both ELO and MEMOCVD techniques were later combined in migration-enhanced lateral epitaxial overgrowth (MELEO) [19]. During the growth process, the optimization of precursor pulses allows controlling the ratio of lateral/vertical growth and the smooth coalescence of adjacent growth fronts can be achieved [19].

1.1.2. The crystal structure of nitrides

The group III-nitrides GaN and AlN can crystallize in the following three crystal structures: hexagonal wurtzite and cubic zinc-blende and rock-salt. However, the wurtzite structure is a thermodynamically stable phase [20], and the highest quality crystals and epilayers are grown in the wurtzite crystal structure. Therefore, the majority of work on nitrides concerns with the hexagonal form.

The crystal structure of wurtzite GaN is shown in Fig. 1.1. It consists of two interpenetrating hexagonal close-packed lattices, which are shifted with

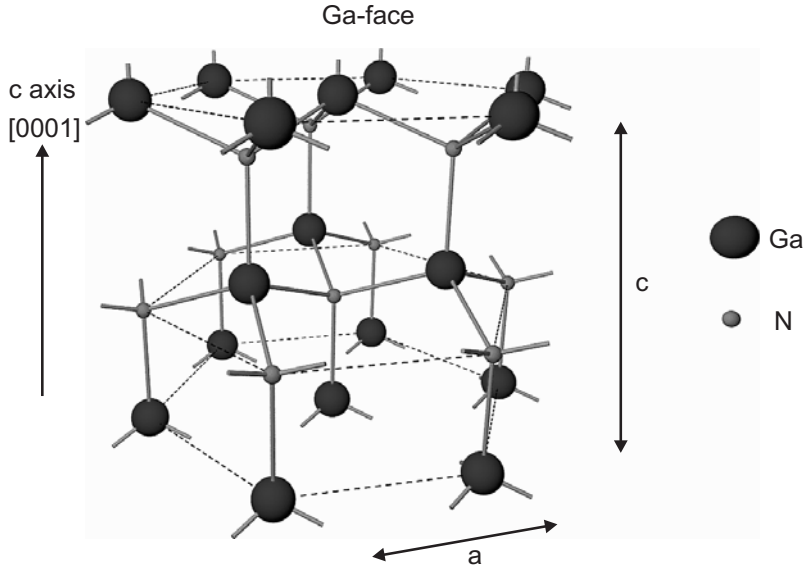

Fig. 1.1. Crystal structure of wurtzite GaN. [http://alexandria.tue.nl/extra2/200611998.pdf]

respect to each other along **c** axis, ideally by $3/8 \cdot c$, where c is the height of the hexagonal lattice cell. Such crystals are anisotropic: they can be characterized by two lattice constants (c and a), and most of the crystal parameters have different values parallel to **c** axis and perpendicular to it. The lattice constants for GaN are $a(\mathrm{GaN}) = 3.189$ Å and $c(\mathrm{GaN}) = 5.186$ Å, and for AlN: $a(\mathrm{AlN}) = 3.112$ Å and $c(\mathrm{AlN}) = 4.982$ Å [21]. The lattice constants for ternary $Al_xGa_{1-x}N$ alloys can be estimated using Vegard's law, i.e. supposing a linear change with composition:

$$\begin{aligned} c\left(Al_xGa_{1-x}N\right) &= x \cdot c\left(AlN\right) + \left(1-x\right) \cdot c\left(GaN\right) \\ a\left(Al_xGa_{1-x}N\right) &= x \cdot a\left(AlN\right) + \left(1-x\right) \cdot a\left(GaN\right) \end{aligned}. \tag{1.1}$$

There is no inversion symmetry in wurtzite lattice along the [0001] direction or **c** axis, since the inversion results in replacement of group III atoms by nitrogen atoms and vice versa. As a result, wurtzite GaN crystals have two distinct faces, commonly known as Ga-face and N-face, which correspond to the (0001) and $(000\bar{1})$ crystalline faces. The atomic arrangement in Ga-face GaN crystal is shown in Fig. 1.1, while for N-face material this can be obtained by flipping the Ga-face material upside-down.

The strong electronegativity of nitrogen enhances the ionicity of the bond between gallium and nitrogen. The ionicity, which is a microscopic polarization, together with the lack of inversion symmetry results in a macroscopic polarization of the crystal. Since this polarization occurs in the equilibrium lattice of III-nitrides at zero strain, it is called spontaneous polarization [22]. In bulk crystals, the charges occuring due to spontaneous polarization compensate each other. However, in heterostructures, consisting of layers with different polarizations, the charges are uncompensated at interfaces and internal electric fields emerge.

1.1.3. Electronic band structure of nitrides

GaN, AlN and their ternary alloys are all direct semiconductors. The consequence of the wurtzite crystal structure is that the valence band

degeneracy at the Γ point is lifted and the band is split to three sub-bands: A, B, and C. The spin-orbit interaction causes the split between heavy and light hole sub-bands A and B, while the "split-off" C band appears due to the interaction with crystal field.

The schematic band structures of GaN and AlN near the Γ point are shown in Fig. 1.2. The splittings between sub-bands have been estimated both experimentally and theoretically. For GaN, the split between A and B valence bands, E_{AB}, is about 6 meV [23], while E_{AC} values show some scattering, however, the latest results seem to converge on the value around 22 meV [21]. The symmetry of the GaN valence sub-bands is Γ_9, Γ_7, and Γ_7 for A, B, and C band, respectively [24].

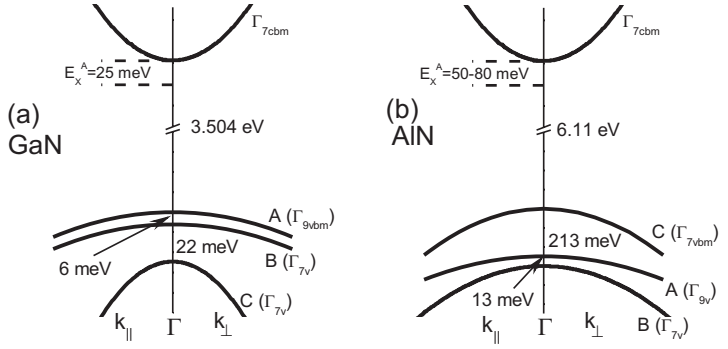

Fig. 1.2. The schematic electronic band structure near Γ point of GaN (a) and AlN (b).

For AlN valence band structure [see Fig. 1.2(b)], only few experimental data are reported, and the values of splits are tentative. The reported values were: $E_{AB} = 13$ meV, and $E_{AC} = -213$ meV [25]. The symmetry of the AlN valence sub-bands is Γ_9, Γ_7, and Γ_7 for A, B, and C band, respectively [24].

The main distinction in AlN valence band structure, if compared to GaN, is the negative crystal-field splitting. Due to this negative value, the crystal-field sub-band becomes the highest valence sub-band in AlN, and participates in optical transitions. Since the polarization of emitted light is determined by the symmetry of conduction and valence bands, such change in the top most sub-band directly affects the light emission. In GaN, the recombination between the electrons in conduction band (Γ_{7c} symmetry) and the holes in the top most valence band (Γ_{9v} or A) is almost prohibited for $E \| c$, and the emission is

polarized in $E \perp c$ [26]. Whereas in AlN, the recombination between the electrons in conduction band (Γ_{7c}) and the holes in the top most valence band (Γ_{7v} or C) is almost forbidden for $E \perp c$, and the emission is polarized in $E \| c$ [25].

When Al content is increased from 0 to 1 in $Al_xGa_{1-x}N$ alloys, the crystal-field splitting decreases from +22 to -213 meV, and the crystal-field sub-band moves up to be the top most valence band, with the crossover taking place at $x \approx 0.25$. This has a fundamental effect on the polarization properties of the radiative emission of AlGaN materials [27]. The crystal-field splitting and crossover point were later shown to be influenced by the strain [28]. In AlGaN-based quantum wells, the emission polarization and its switching could also be affected by the internal field [29], and quantum confinement [30].

The band gap at room temperature is 3.439 eV for GaN [21] and ~6.03 eV for AlN [31]. The traditionally used AlN bandgap value of 6.2 eV at 300 K has been recently reevaluated due to the availability of higher quality AlN crystals, and a lower bandgap value has been estimated [31]. The band gap of ternary AlGaN alloys is not a linear function of Al content and is usually expressed using the following expression:

$$E_g\left(Al_xGa_{1-x}N\right) = x \cdot E_g\left(AlN\right) + \left(1-x\right) \cdot E_g\left(GaN\right) - bx\left(1-x\right), \qquad (1.2)$$

where b is the bowing parameter. The bowing parameter was shown to depend on strain, buffer layer properties, and growth conditions, and several different values were reported. Most of them were analyzed by Lee et al., and an intrinsic value of $b = 0.7$ eV was suggested [32].

An important parameter, which must be taken into account when designing devices, is the valence band offset in GaN/AlN heterostructure. A number of calculations and experimental works have been reported, and the majority of them seem to fall in the 0.7-0.8 eV range [21] corresponding to approximately 30%/70% ratio of the valence band/conduction band offsets [33].

The exciton binding energy in GaN has been estimated with high accuracy as 25 meV [23], while for AlN, it is not accurately known so far. Values between 50 and 80 meV have been suggested [25,34].

1.1.4. Internal fields in nitride heterostructures

The direct consequence of the wurtzite crystal structure of nitrides is the existence of spontaneous polarization, as already mentioned in section 1.1.2. Also, the piezoelectric tensor of wurtzite has three nonvanishing independent components. Therefore, the polarization in nitride material system will have both spontaneous and piezoelectric polarization components [22].

The piezoelectric component appears when the crystal lattice is changed externally from its ideality. One way to change the crystal lattice ideality is through strain. In heterostructures, the thin layers of different content are grown layer by layer. The content difference results in small difference of lattice constants, which introduces strain. This strain results in the piezoelectric polarization component.

The values of spontaneous polarization for GaN and AlN materials are P_{sp}(GaN) = -0.034 C/m^2, and P_{sp}(AlN) = -0.090 C/m^2 [21], while the strain-depending piezoelectric polarization must be calculated for the particular case, using the following expression:

$$P_{pe} = 2 \cdot \frac{a - a_0}{a_0} \cdot \left[e_{31} - e_{33} \frac{C_{13}}{C_{33}} \right], \tag{1.3}$$

where a and a_0 are the strained and unstrained lattice constants, e_{31} and e_{33} are piezoelectric constants of the strained material, C_{13} and C_{33} are elastic constants of the strained material.

The electrical polarization in nitride alloys was usually estimated by a linear interpolation between the values of the binary compounds [22]. However, later theoretical calculations suggested a nonlinearity of macroscopic polarization in nitride alloys [35], which was also confirmed experimentally [36].

In bulk or thick quasi-bulk layers, the strain is relaxed via dislocations and, thus, piezoelectric component equals zero, while the charge due to spontaneous polarization self compensates. In heterostructures, the difference of spontaneous polarization at the heterojunction, in addition to the strain-induced piezoelectric component, results in the creation of the internal electric field [37].

The effect of internal electric field on optical properties is schematically illustrated in Fig. 1.3. Two types of quantum well structure are shown: without the internal field [Fig. 1.3(a)] and with the internal field [Fig. 1.3(b)]. As can be observed, the internal electric field induces band tilting and, thus, reduces an effective band gap. This effect is called quantum-confined Stark effect (QCSE) [38]. The confined carriers become spatially separated, the overlap between electron and hole wavefunctions reduces, therefore the luminescence intensity decreases, while the carrier lifetime increases [39,40].

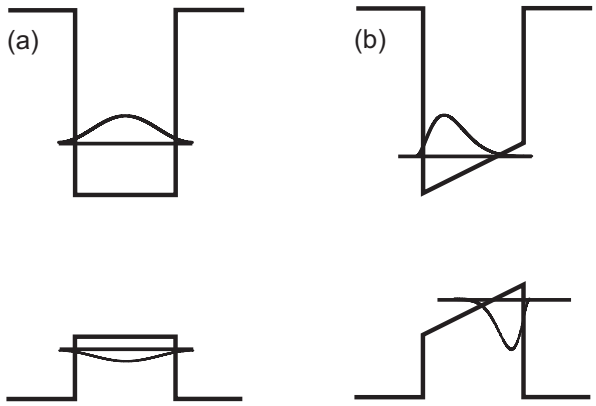

Fig. 1.3. The band diagram and lowest energy levels of the quantum well without the built-in field (a) and with built-in electric field (b).

The presence of the internal electric field in nitride heterostructures is unwanted, since it introduces the variation in emission wavelength and carrier lifetime with carrier injection density [41] and time [42]. The influence of the internal field can be reduced by making quantum wells narrower. In that case, the quantum-confined levels are higher than the triangular bottom of the well, and the QCSE effect becomes negligible [43]. The internal electric field could also be reduced by doping the barrier layers [40], or, for quaternary AlInGaN-based structures, both the barrier and well layer composition could be selected such as to minimize the difference in spontaneous polarization and lattice constants [40]. The most radical way to reduce the internal electric field is growth on nonpolar

substrates, e.g. sapphire *r*-plane or GaN *m*-plane [41]. Since in that case the growth direction is perpendicular to the polar axis in GaN [0001], there is no electric field in structures grown on nonpolar substrates. However, the quality of such structures is worse [41,44].

1.2. Yellow band in GaN

In addition to the luminescence bands due to band-to-band, excitonic and other near-edge transitions, the photoluminescence spectrum from GaN layers almost always contains a broad yellow luminescence (YL) band peaking at 2.2-2.3 eV. The YL band appears to be universal: it has been observed in unintentionally and intentionally doped GaN layers grown by various techniques on different substrates and under different growth conditions. The intensity of the YL can vary over a wide range, and it might be used as a figure of merit to assess the quality of GaN epilayer with good samples showing almost no YL.

The YL band has been the topic of hundreds of publications and is by far the most studied band in GaN. Despite this inordinate effort, the origin and properties of the YL band are still not completely resolved. The main YL band features in undoped and doped GaN were summarized in a comprehensive review by Reshchikov and Morkoc [45], and the most important questions discussed in literature can be classified to three groups: i) the type of transition responsible for the YL [45-50]; ii) the identity of the YL-related defect(s) [45,51-58]; iii) the relation between the YL and structural defects (dislocations) [54,59-64].

Two substantially different models of radiative transition responsible for YL had been proposed: recombination between shallow donor and deep acceptor [46], and an alternative model involving deep donor and shallow acceptor [47]. Even though the latter model appeared very improbable and most of the published reports argued against it, it was seemingly confirmed by several experimental groups [48]. Later on, however, the similar experimental

results were reinterpreted in favor of the first YL model [49], and it was firmly established that the YL band in all *n*-type GaN samples is related to transitions from a shallow donor (or conduction band) to a deep acceptor [45]. The position of shallow donor level was estimated at ~30 meV below conduction band [46,50], and the position of deep acceptor level was estimated at 0.8-0.9 eV above valence band [45,46].

The identity of the shallow donor could be any, since most of the donor impurities result in energy levels 20-30 meV below conduction band [51,52]. The identity of deep acceptor is still somewhat ambiguous, and two models are suggested: i) in undoped *n*-type GaN, the YL band emission has been assigned to a native defect, and it is widely agreed that gallium vacancies (V_{Ga}) or its complexes with unintenional donors (V_{Ga}-D, or most often V_{Ga}-O_N) are involved [45,53-55]; ii) in C-doped GaN, the YL-related defect is assigned to C impurity related levels [45,55-57].

Recently, the luminescence and photoconductivity investigations on high-quality GaN samples allowed separating two distinct transitions between deep levels and conduction band contributing to the YL band. Different configurations of V_{Ga}-O_N defect complex were assigned to these transitions [45,54,58].

The relation between YL and structural defects is also still a subject for discussion, since both correlation [54,59-61] and anticorrelation [62-64] have been reported. Theoretical calculations showed that formation of V_{Ga} and its complexes with O_N near dislocations is energetically favorable [59], and experimental results from GaN samples with different dislocation densities confirmed the correlation [54,60,61]. However, there are also experimental results published, which do not see any dislocation-induced enhancement of the YL band [62-64].

1.3. Stimulated emission and optical gain in GaN

The stimulated emission (SE) in GaN was first observed from optically pumped single-crystal needles by Dingle et al. already in 1971 [65]. Two processes were pointed out as the most probable origin of stimulated emission in GaN: inelastic exciton-exciton/carrier scattering resulting in radiative recombination of the exciton colliding with another exciton [66] or electron (hole), and recombination in electron-hole plasma (EHP), which occurs at high-density and/or high-temperature regime [67]. The competition of these two SE mechanisms depends mainly on carrier density and temperature. Later reports concerning SE mechanisms mainly reported on the increase of temperature at which the exciton-related SE could still be observed: from 80 K in GaN needle crystals [68], up to 150 K in MOCVD-grown GaN [69], up to 180 K in HVPE-grown GaN [70], and up to 440 K in homoepitaxial GaN [71]. Generally, the higher is the temperature for exciton-related SE to manifest itself, the higher is the quality of the crystal. At high temperature, the exciton- and EHP-related bands were shown to co-exist due mainly to spatial separation of EHP located at the sample surface and the dense exciton system located deeper from the surface [71].

An important parameter characterizing stimulated emission is the threshold of the SE. However, the reported SE threshold values for the separate GaN samples were scattered in a wide range from ~0.1 MW/cm^2 [72] to ~4 MW/cm^2 [73], depending on temperature and growth conditions. Generally, it is expected that higher quality GaN epilayers should exhibit lower SE threshold, however Malinauskas et al. reported a contrary correlation: a lower SE threshold was found for layers with higher dislocation density [74]. Such correlation was attributed to the formation of favorable conditions for triggering SE in the vicinity of dislocations [74]. This result, however, is somewhat doubtful, since the SE threshold was estimated not from direct observation of SE band in PL spectra, but indirectly from four-wave-mixing (FWM) experiments.

Measurements of SE do not allow estimating the optical gain coefficient, which is an important parameter for development of GaN-based laser diodes. The theoretically predicted optical gain values for GaN were up to 10^4 cm^{-1} [75], with such large optical gain due to the high joint density of states due to three close sub-bands forming the valence band edge and the large electron effective mass in the conduction band minimum [75].

There are several different experimental techniques for measuring the optical gain and its spectrum, each with its own advantages and limitations. The pump-and-probe [76,77] spectroscopy is the most straightforward technique, however, thin samples with the thickness on the order of 1 μm to ensure sufficient transparency have to be used in the experiments. In structures with laser cavities, the Hakki-Paoli technique [78,79], based on the Fabry-Perrot longitudinal modes, is usually employed. However, need for samples specially prepared for application of this experimental technique makes the Hakki-Paoli technique less attractive.

The most popular method for measuring optical gain is the variable stripe length (VSL) technique [80]. This method is based on exciting a narrow stripe on a surface perpendicular to sample edge and collecting luminescence coming out from the stripe end at the sample edge (see Fig. 2.2; experimental details are given in section 2.1). In a one-dimensional model, the edge luminescence intensity can be expressed as [80]:

$$I_{st}(h\nu, l) \propto \frac{I_{sp}(h\nu, l)}{g}\left[\exp(gl) - 1\right], \tag{1.4}$$

where I_{sp} is the spontaneous emission intensity, l is the excited stripe length, and g is the optical gain coefficient, including optical losses. The optical gain coefficient is a material parameter and depends on excitation intensity, excitation wavelength, and radiative recombination efficiency. An important factor when considering gain coefficient is a type of structure under study, i.e. whether it is an epilayer or a heterostructure. The reported gain coefficient values vary in a wide range from ~100 cm^{-1} in GaN epilayer on sapphire [81] to ~2000 cm^{-1} in GaN on SiC [82], and up to ~7200 cm^{-1} in homoepitaxial GaN

[83]. The increase of gain coefficient is related to the increase in GaN material quality and nonequilibrium carrier lifetime, as it was shown by comparing heteroepitaxial and homoepitaxial GaN layers [83].

The equation (1.4), however, is valid only for unsaturated gain. The optical gain saturation occurs when the propagating light is strong enough to reduce the photoexcited carrier density. The gain saturation can be observed when the product of optical gain coefficient and stripe length reaches a critical value [84-86]. The critical saturation value was studied in the nitride laser structure and found to be between 4 and 10, depending on the number of quantum wells and the modal peak gain value [84]. For most semiconductor materials, the critical saturation value is typically assumed to be ~5. In this case, the maximum stripe length which can be used for unsaturated gain measurements is equal to 500 μm for 100 cm^{-1} gain, and 10 μm for 5000 cm^{-1} gain. Thus, the gain saturation drastically limits the meaningful stripe lengths used in the VSL experiments for high-gain-material measurements.

1.4. Carrier dynamics in GaN

Carrier dynamics in semiconductors is usually characterized by a single parameter: the nonequilibrium carrier lifetime. It is even considered as a figure of merit describing the material quality [83,87]. The dynamics of nonequilibrium carrier density in GaN is strongly affected by recombination involving donor and acceptor levels, and carrier trapping. Thus, certain recombination mechanisms usually have to be investigated separately under specific experimental conditions. According to the studied recombination mechanisms, the reports can be classified to the following groups: i) defect-level-related PL band dynamics [45,88-90]; ii) exciton lifetime [91]; and iii) free carrier lifetime at room temperature [74,87,92-106].

The results on decay transients of defect-related PL bands, such as yellow luminescence, blue luminescence (BL) and ultraviolet luminescence (UVL) are summarized by Reshchikov and Morkoc [45]. For all these PL bands, the

decays were reported to be nonexponential at low temperatures [88], which indicate the recombination between donor and acceptor pairs (DAPs). In this case, the radiative recombination rate W is not constant but depends exponentially on the separation, R, between the donor and acceptor involved [89]:

$$W(R) = W_{\max} \exp\left(-\frac{2R}{a_D}\right), \tag{1.5}$$

where W_{max} is the transition probability in the limit $R \to 0$ and a_D is the Bohr radius for a more weakly bound particle (an electron on the shallow donor in GaN). It is evident from Eq. (1.5) that the lifetime of the bound hole, $\tau = W^{-1}$, is much longer for distant pairs than for close ones. This results in an increase of the instantaneous lifetime of the measured PL with the time delay, and the PL decay curve becomes nonexponential. If it is assumed that the same shallow donor participates in all transitions causing YL, BL, and UVL [90], the decay of defect-level-related PL bands at low temperature can be characterized by a single parameter, W_{max}. It was found to be of the order of 10^8 s^{-1} for UVL band, 10^7 s^{-1} for BL band, and 10^6 s^{-1} for YL band [90].

With increase in temperature, the shallow donor participating in DAP transitions becomes thermally ionized, and the transition changes to conduction band-acceptor. The PL decay was shown to become exponential with characteristic time of the order of 3 μs for UVL band, 10 μs for BL band, and 50 μs for YL band [88].

The exciton dynamics is usually investigated at low temperatures. The studies of exciton lifetime were limited by a lack of high-quality GaN samples, which became available only recently. The properties of free and bound excitons in GaN were reviewed by Monemar et al. [91]. The free exciton radiative lifetime at 2 K was estimated to be ~1.5 ns, the decay time of donor bound exciton was reported in the range of 1.1-1.8 ns, and the decay time of acceptor bound exciton was ~0.9 ns [91].

Since most of the optoelectronic devices are operated at 300 K temperature and under high excitation conditions, it is important to investigate carrier

dynamics under such conditions. The high excitation ensures that the trapping centers and deep levels are saturated and do not significantly affect the carrier lifetime. The reported values of room-temperature lifetimes in GaN show a considerable increase over the last few years due to innovative growth

Table 1.1. Evolution of nonequilibrium carrier lifetime at 300 K in GaN epilayers

Carrier lifetime or PL decay time	Sample	Year	Reference
38 ps	MOCVD GaN/sapphire	1997	[92]
130 ps; 400 ps;	GaN on ELO GaN/sapphire template	1999	[87]
500 ps	MBE GaN on HVPE GaN template	2004	[93]
530 ps	HVPE GaN/sapphire	1999	[94]
150 ps; 740 ps	MOCVD GaN/sapphire	2000	[95]
98 ps; 722 ps	bulk GaN on ELO GaN	2000	[96]
890 ps	homoepitaxial GaN	2001	[97]
0.26 ns; 0.9 ns	ELO GaN/sapphire	2006	[98]
0.91 ns	a-plane ELO GaN/sapphire	2005	[99]
100 ps; 1 ns	ELO GaN/sapphire	2005	[100]
1.1 ns	MOCVD GaN with SiN interlayer	2006	[101]
1.25 ns	high-pressure grown bulk GaN	2009	[102]
0.47 ns; 1.86 ns	MOCVD GaN on TiN network template	2005	[103]
2.0 ns	MOCVD GaN on MEMOCVD buffer	2005	[P4]
2.2 ns	HVPE GaN on GaN template	2006	[104]
0.53 ns; 2.67 ns	MOCVD GaN on SiN network template	2007	[105]
3.0 ns	high-pressure grown bulk GaN	2009	[102]
3.3 ns	freestanding HVPE GaN	2009	[102]
5.4 ns	HVPE GaN, 400 μm thick	2006	[101]

techniques and improving material quality. The evolution of carrier lifetime in GaN at room temperature is given in Table 1.1.

As can be seen in Table 1.1, in many cases nonexponential PL decay was observed, which was approximated by a sum of two exponential components [87,95,96,98,100,103,105]. The biexponential decay was assigned to capture and recombination processes in a multilevel system, and were related to

capture into deeper (nonradiative) centers, either in the bulk or at the surface of the layer, followed by recombination [103]. Later on, by comparison of FWM and TRPL results and numerical calculations it was shown that in thick GaN layers with high carrier lifetime the nonexponentiality of PL decay appears to be due to the influence of carrier diffusion to the depth, surface recombination and PL reabsorbtion [101,104,106].

The carrier lifetime is strongly related to the material quality. By comparing a number of differently-grown GaN samples with wide range of dislocation densities, it was shown that the decrease of dislocation density from ~10^{10} cm^{-2} to ~10^{6} cm^{-2} resulted in increase of carrier lifetime from ~150 ps to ~5.1 ns [74].

1.5. Optical properties of AlGaN epilayers and structures

The optical properties of ternary AlGaN materials, obtained from binary GaN and AlN compounds, are already affected due to the random mixing of Ga and Al atoms. Statistical fluctuations in the composition of a random alloy lead to potential fluctuations capable of spatially localizing excitons. Spatial localization improves the quantum efficiency by preventing nonradiative recombination. However, spatial localization causes broadening of the excitonic emission of the alloy compared to that of a binary compound. An additional source of broadening can be phase separation, where large-scale inhomogeneities in the composition cause potential energy fluctuations on a larger spatial scale. Exciton localization due to clustering and phase separation is thought to be essential for the high luminescence efficiencies observed in InGaN [107].

Even though the theoretical estimations predict no phase separation for AlGaN alloys [108,109], AlGaN has a larger band gap than InGaN and should exhibit stronger potential energy fluctuations for the same percentage of compositional inhomogeneity. Compositional fluctuations and Al segregation, in particular around the dislocations [110], have been directly evidenced by

transmission electron microscopy and spatially resolved cathodoluminescence [110,111]. The phase separation and spontaneous modulation, depending on AlN mole fraction, have been reported to vary across the full alloy series [112].

The optical properties of AlGaN materials have been widely investigated using luminescence spectroscopy [113-118]. Similar to InGaN, anomalous temperature dependence of the PL band peak energy (redshift-blueshift-redshift, the so-called S-shape; or blueshift-redshift) [113-118] and W-shaped temperature dependence of PL band width [113] have been observed. These results indicated the presence of density-of-state tails, which originate from fluctuations of potential due to alloy disorder and can localize excitons. The S-shaped temperature dependence could be described using the modified Varshni equation based on a band-tail-filling model [115,116]. The parameter describing potential fluctuations, σ, was shown to increase with increase in aluminum content. Meanwhile, the temperature of transition from the blueshift to the redshift of the PL band peak energy also increases [113,114]. Such behavior pointed out to the increase of carrier localization depth with increasing aluminum content, however, it also revealed potential fluctuations somewhat larger than those predicted by model of perfectly random alloy broadening, thus indicating possible alloy clustering [115].

The PL decay kinetics in AlGaN materials has been mostly investigated at low temperatures [113-115,118,119]. The PL decay times were shown to increase with increasing aluminum content [113-115,118,119], with the values ranging from ~200 ps for low Al content up to ~3 ns for high Al content [114,119], again indicating stronger localization for higher aluminum content. The PL decay time was observed to depend on localization depth: the decay time increased with decreasing energy of the emitted ptoton [113,114,118]. Such behavior also indicates exciton localization when the decay of excitons is not only due to radiative recombination, but is also affected by exciton transfer to lower energy states. The increase of temperature up to 300 K resulted in strong decrease of PL decay time to <50 ps, while the decay time dependence on emission energy disappeared [120].

The carrier dynamics in AlGaN-based structures has been mostly investigated in AlGaN/GaN structures, and there are only a few reports on AlGaN/AlGaN quantum wells [42,121-124]. Carrier localization in QW structures was shown to be caused not only by compositional inhomogeneity, but also by well width fluctuations [121]. Additionally, the strong effect of internal electric field on optical properties was observed [42,122-124]: the time-dependent [42] and excitation-dependent [123] shift of the PL peak energy due to electric field screening/recovery processes, and the dependence of PL decay time on QW width [124]. The PL decay time was shown to become longer for wider QWs [124].

2. Experimental setup

2.1 Steady- and quasi-steady-state photoluminescence spectroscopy

Photoluminescence spectroscopy is one of the most informative and versatile techniques for optical characterization of semiconductor materials and structures. Photoluminescence measurements under steady- and quasi-steady-state conditions were carried out by using continuous-wave (CW) and pulsed laser excitation, respectively. To achieve extremely low excitation conditions, LEDs were used as excitation sources.

Figure 2.1 shows the sketch of the experimental setup used for PL measurements under pulsed excitation. Flashlamp-pumped Q-switched solid-state Nd:YAG laser (1) serves as a pulsed excitation source. The laser operates at a repetition rate of 10 Hz and generates 4 ns pulses with peak power up to

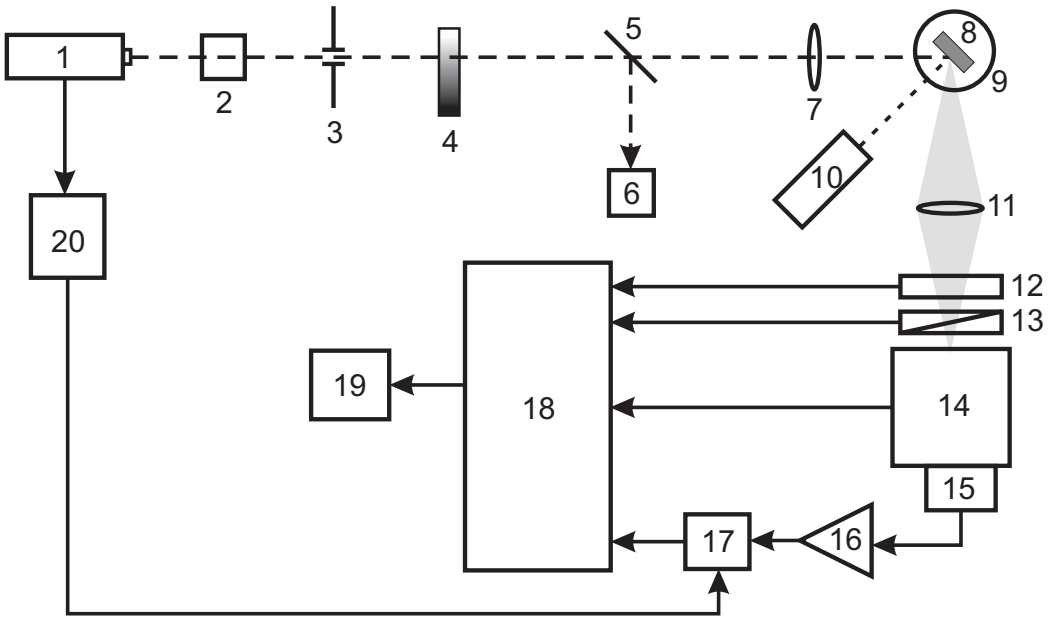

Fig. 2.1. Experimental setup for PL measurements under quasi-steady-state conditions: 1 – laser; 2 – harmonics modules; 3 – pinhole; 4 – attenuator; 5 – beam-splitter; 6 – photodiode gauge; 7 and 11 – spherical quartz lenses; 8 – sample; 9 – cryostat; 10 – telescope; 12 – shutter; 13 – polarizer; 14 – monochromator; 15 – photomultiplier tube; 16 – amplifier; 17 – box-car integrator; 18 – control unit; 19 – computer; 20 – signal generator.

several megawatts. For the III-nitride samples under investigation, frequency-tripled (3.49 eV), quadrupled (4.66 eV) or quintupled (5.82 eV) radiation of the laser fundamental emission line (1.16 eV) was used. Frequency conversion is implemented by nonlinear optical KDP crystals (2). In some cases, when a better spatial homogeneity of the beam cross-section is required, a pinhole (3) is introduced. It also helps to remove residual radiation of lower order harmonics. The excitation intensity is altered either by a set of neutral density filters (4) or by a half-wave plate and Glan prism used as a polarizer and analyzer, respectively. For continuous monitoring of the excitation pulse energy, the laser beam is split and a part of the beam (~10%) is deflected to a photodiode gauge (OPHIR PD-10) (6) using a quartz plate as a beam-splitter (5). The laser beam is focused onto the sample (8) by a quartz spherical lens (7). The area of the excitation spot on the sample surface is estimated by a telescope (10). Thereafter it is used for estimating the excitation power density. A closed-cycle helium cryostat (9) is used for cooling down the samples from room temperature to 8 K. The PL signal is collected by another quartz lens (11) at the entrance slit of a 0.6 m double monochromator (Jobin Yvon HRD-1) (14) with holographic gratings. The dispersed luminescence is detected by using an UV-enhanced photomultiplier tube (Hamamatsu R1463P) (15) with a subsequent amplifier (16) and a box-car integrator (17). The box-car integrator is synchronized by a pulse generator (20) triggered by the laser pulse. The measurement parameters, like the wavelength range, the high-voltage of the photomultiplier tube, the acquisition time, the number of measurement cycles and others, are set through the computer (19), which controls experimental process via the control unit interface (18). The control unit rotates the gratings, triggers the mechanical shutter (12), blocks the scattered light at the laser frequency in order to prevent the photomultiplier from damaging, and also digitizes the analog signal received from the box-car integrator and passes it to the computer. Afterwards, experimental spectra undergo a spectral correction procedure. The raw spectra must be corrected for the spectral distortions caused by the nonuniform response of the detection system.

A similar setup with some minor changes is used to measure PL under continuous wave excitation by a He-Cd laser operating at 325 nm wavelength or LEDs with various wavelengths. In this case, a single-photon counter is used instead of the amplifier (16) and box-car integrator (17).

Figure 2.2 shows two sample excitation geometries, which were exploited in order to distinguish between spontaneous and stimulated emission under pulsed excitation. In the front-surface configuration [see Fig. 2.2.(a)], the excitation beam is focused using a spherical lens to a spot with typical diameter of 0.5 mm. The collected luminescence in this case contains contribution mainly due to spontaneous emission.

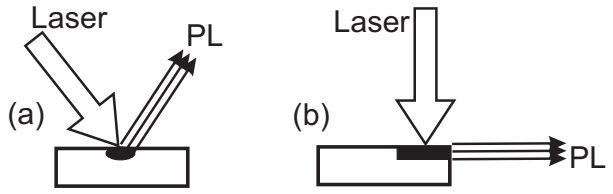

Fig. 2.2. Sample excitation geometries: front-surface (a) and lateral (b).

In the lateral configuration, the excitation beam is focused to a 30 μm wide stripe on the crystal surface by using a cylindrical lens [see Fig. 2.2(b)]. The amplified light propagating along the sample surface is collected from the cleaved edge of the crystal. The lateral excitation configuration [see Fig. 2.2(b)] is also useful for optical gain measurements by using a variable stripe length technique, proposed by Shaklee et al. [80]. The method allows one to estimate the optical gain coefficient as well as the gain spectrum from the lateral stimulated emission spectra, measured at different excitation stripe lengths, provided that the width of the stripe is considerably smaller than its length. The length of the stripe is varied by a blocking screen with the calibrated positioning. The blocking screen is placed very close to the sample surface in order to avoid diffraction effects.

2.2 Setup for time-resolved PL study under high excitation

Time-resolved PL measurements under high-excitations were carried out by using the setup schematically shown in Fig. 2.3. Actively-passively mode-

locked Nd:YAG laser (1) is used as an excitation source. The laser operates at 10 Hz and generates 25 ps-long pulses. The laser contains an amplifier with 10 mm Nd:YAG rod for improved beam profile. The laser is equipped with a harmonics unit (2) to generate harmonics by using nonlinear crystals and separate them from residual radiation. Harmonics up to the 5^{th} (5.82 eV) can be generated in this unit.

The layout of the sample excitation part is analogous to that, described in section 2.1: the excitation laser beam passes a pinhole (3) for spatial filtering, attenuator (4) for intensity variation and is focused onto the sample (8) by a spherical quartz lens (7). A part of the beam (~10%) is reflected by a quartz beam-splitter (5) for continuous monitoring of excitation by a photodiode gauge (OPHIR PD-10) (6). Due to the possible high energy density the use of neutral density filters for excitation attenuator (4) is meaningless, since the filters could easily be damaged. Therefore, Fresnel rhomb and Glan prism are used as a polarizer and analyzer, respectively. The area of the focused excitation spot on the sample surface is estimated by a telescope (9). The PL signal from the sample is collected by a pair of quartz lenses (10,11) and

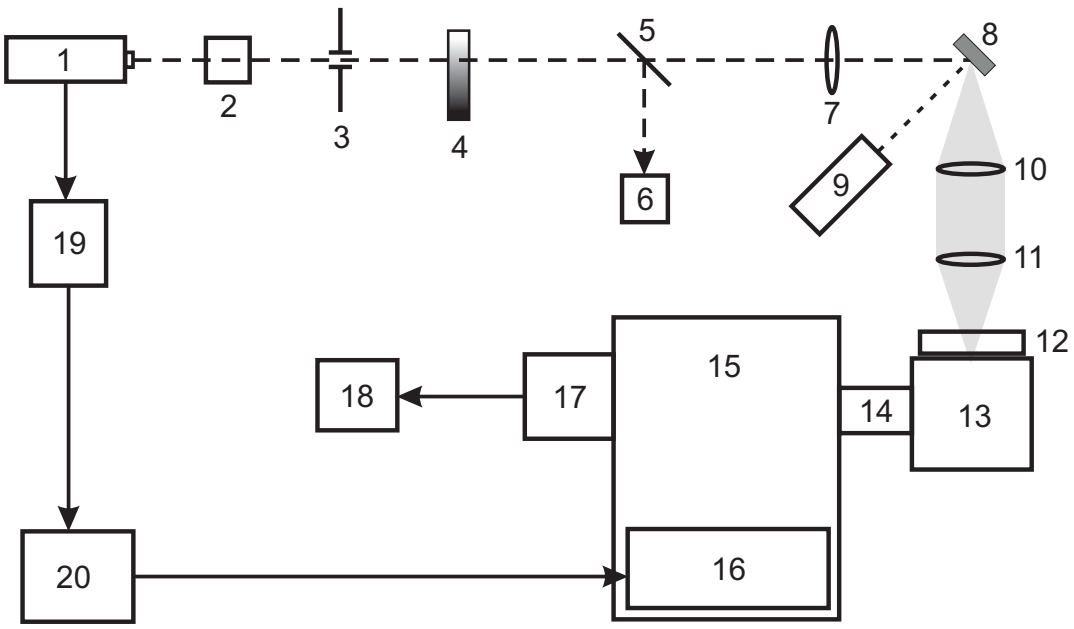

Fig. 2.3. Experimental setup for TRPL measurements:
1 – laser; 2 – harmonics modules; 3 – pinhole; 4 – attenuator; 5 – beam-splitter; 6 – photodiode gauge; 7, 10 and 11 – spherical quartz lenses; 8 – sample; 9 – telescope; 12 – shutter; 13 – monochromator; 14 – collection optics; 15 – streak camera; 16 – sweep unit; 17 – CCD camera; 18 – computer; 19 – Pre-T module; 20 – delay unit.

focused on the entrance slit of the imaging spectrograph (Chromex 250 IS C5904) (13) with internal shutter (12).

The detection and data acquisition system is based on the streak camera (Hamamatsu C5680-34) with UV-enhanced streak tube (N5716-01) (15). The dispersed image is transferred to the streak camera by an optical adapter (14) instead of exit slit on the spectrograph (13). The high speed single-sweep unit (M5676) (16), incorporated in the streak camera, allows measurements with time ranges from 200 ps to 50 ns with the time resolution of 2 ps. However, in our system the time resolution is limited by the laser pulse duration. The digital CCD camera (C4742-95-12) (17) is used as a readout camera, i.e. it reads the streak image and transfers it to the computer (18).

The streak camera is synchronized with the laser by using a special Pre-T synchronization module (19). The advantage of this module over the conventional trigger output of the laser is that it produces triggering pulses with small jitter. A delay unit (C1097-04) (20) is used to adjust the delay time of the trigger signal.

2.3 Light-induced transient grating technique

The sketch of the LITG experimental setup is shown in Fig. 2.4. The mode-locked Nd:YAG laser (1) is used both as an excitation and probe source. The laser operates at 10 Hz and generates 25 ps-long pulses. The laser is equipped with a harmonics unit (2) to generate harmonics by using nonlinear crystals and separate them from residual radiation. For the III-nitride samples under investigation, the 3^{rd} (3.49 eV) or 4^{th} (4.66 eV) harmonics are used for pump beams, while the 2^{nd} (2.33 eV) harmonics is used as a probe beam.

The pump beam is split to two beams of approximately equal intensity by using the 50% beamsplitter (BS3). Both beams are made to overlap on the sample (4) surface by using a set of mirrors (M3-M8). By rotating the mirrors M7 and M8, the angle between pump beams can be changed. The optical paths of both beams are made to be equal, so that they reach the sample at the same

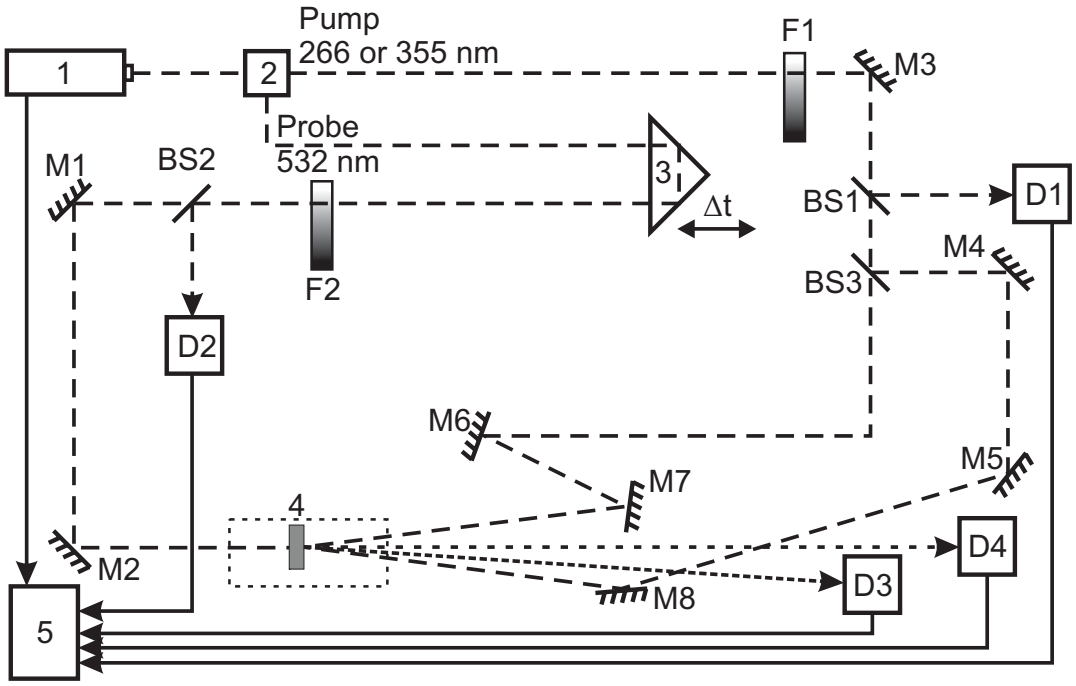

Fig. 2.4. Experimental setup for LITG measurements:
1 – laser; 2 – harmonics modules; 3 – prism; 4 – sample; 5 – computer; M1-M8 – quartz mirrors; BS1-BS3 – beam-splitters; D1-D4 – photodiode detectors.

time. The excitation intensity is varied by using a set of neutral density filters (F1), and monitored by a photodiode (D1) after a fraction of beam (~10%) is reflected by using a beamsplitter (BS1).

The probe beam is brought to the backside of the sample by a set of mirrors (M1-M2) and made to pass the sample (4) at the same point where the pump beams overlap. The probe beam intensity is varied by a set of neutral density filters (F2), and monitored by a photodiode (D2) after a fraction of beam (~10%) is reflected by using a beamsplitter (BS2). The variable delay of probe beam with respect to pump beams is achieved by moving the prism (3). The transmitted and diffracted parts of the probe beam are registered by photodiodes D4 and D3, respectively. The signals from all photodiodes are registered by computer (5), which also controls the probe beam delay by moving the prism (3). Since the pump and probe beam intensities are fluctuating, the intensity gating for one or both beams is used, i.e. only the signal passing the gate conditions is registered by computer (5). From the

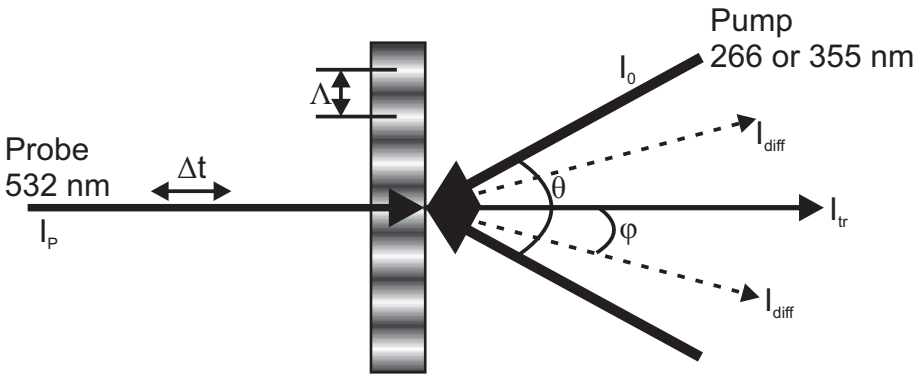

Fig. 2.5. The schematics of the four-wave mixing used in LITG experiments.

measurement results, the diffraction efficiency, which is the ratio of intensities of diffracted and transmitted beams, is calculated:

$$\eta_{diff} = \frac{I_{diff}}{I_{tr}}. \tag{2.1}$$

The light-induced transient grating technique is based on excitation of a semiconductor with a light interference pattern and observation of light diffraction caused by free carrier plasma. The four wave mixing scheme is used in experiments (see Fig. 2.5). Two beams of the same wavelength and similar intensity hit the sample with an angle θ between them. The beams interfere and the resulting light field intensity distribution is described by equation:

$$I(x) = I_o\left(1 + m\cos\left(\frac{2\pi}{\Lambda}x\right)\right), \tag{2.2}$$

where $I_0 = I_1 + I_2$ is the sum intensity of both beams, $m = \frac{2\sqrt{I_1 I_2}}{I_1 + I_2}$ is modulation depth of interference field, and Λ is the fringe spacing, which depends on the excitation wavelength λ and an angle θ between the interfering beams:

$$\Lambda = \frac{\lambda}{2\sin\left(\frac{\Theta}{2}\right)}. \tag{2.3}$$

The pump beams are strongly absorbed, and, thus, create a spatially-modulated distribution of the nonequilibrium carrier density $N(x) = N_0 + \Delta N\cos\left(\frac{2\pi}{\Lambda}x\right)$,

where N_0 and ΔN are the non-modulated and modulated carrier densities, respectively. The modulation of carrier density results in modulation of refractive index change Δn. For strongly absorbed excitation, a thin grating is created, and a direct proportionality $\Delta n \propto \Delta N$ is valid.

A variably delayed probe beam monitors the dynamics of optically induced modulation of the refractive index and, thus, carrier density, by probe beam diffraction on the grating. The diffraction efficiency $\eta(t)$, i.e. the intensity of the diffracted beam normalized to the transmitted probe beam intensity, is shown to be proportional to squared carrier density, and its decay can be expressed as [125]:

$$\eta(t) \propto \exp\left(-\frac{2t}{\tau_G}\right), \tag{2.4}$$

where τ_G is the characteristic time of the experimentally observed grating decay.

The decay of the diffraction grating is caused by two effects: recombination of the nonequilibrium carriers and their diffusion, which tends to homogenize the carrier spatial distribution. The grating decay time, τ_G, can be expressed through the ambipolar diffusion coefficient, D_a, and recombination time, τ_R, as [125]:

$$\frac{1}{\tau_G} = \frac{1}{\tau_R} + \frac{4\pi^2 D_a}{\Lambda^2}. \tag{2.5}$$

Thus, a linear plot of $1/\tau_G$ against $1/\Lambda^2$ allows one to determine both τ_R and D_a simultaneously, provided that the decay of the grating efficiency is measured at several different Λ.

2.4 Luminescence lifetime measurements in frequency domain

Luminescence decay under extremely low excitation was investigated by using luminescence lifetime measurements in frequency domain technique. The sketch of the experimental setup is shown in Fig. 2.6. An LED (1) is used as an excitation source. The intensity of LED emission is modulated in a wide

frequency range from 5 Hz to 200 MHz by using the signal generator (Aeroflex IFR 2023A) (15) or DSP lock-in amplifier (Signal Recovery 7265) (14-15) and bias tee (Picosecond pulse labs 5547) (16), which couples the ac signal from signal generator and dc signal for LED biasing from external power supply (17).

The LED emitted light is collimated by using lens (2), and passes through an optical short-pass filter (3), which cuts off the parasitic long-wavelength tail of LED emission. Afterwards, the excitation beam is reflected by a dichroic mirror (4) and focused onto the sample (6) by another lens (5). A closed-cycle helium cryostat (7) is used for cooling down the samples from room temperature to 8 K. The sample PL emission is collected by the same lens (5), and passes the dichroic mirror (4) and long-pass filter (8). The dichroic mirror (4) is selected in such a way, that it reflects the shorter-wavelength excitation light, while transmitting the longer-wavelength sample PL light. Additionally, the optical long-pass filter further blocks the excitation light from reaching the

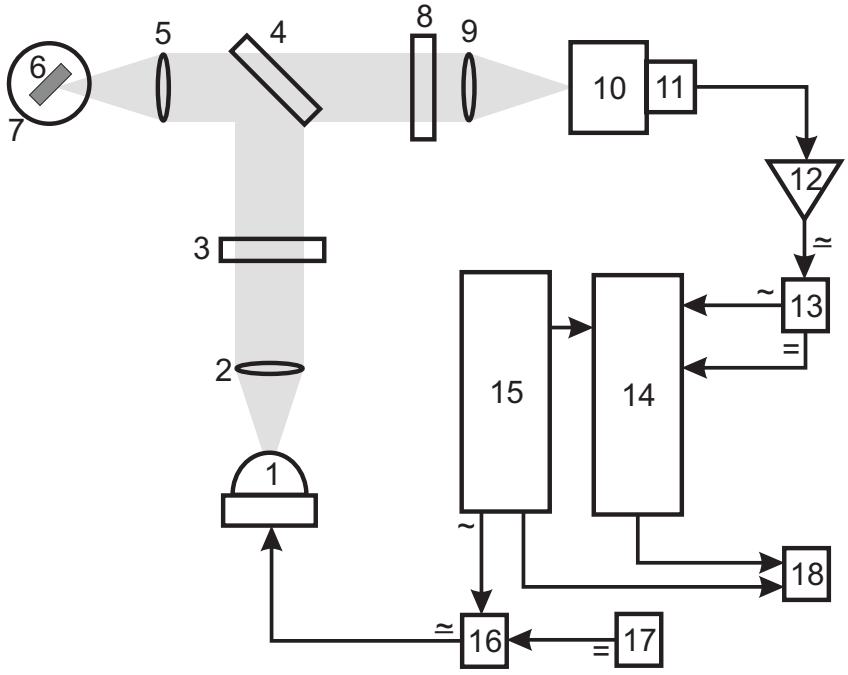

Fig. 2.6. Experimental setup for FDLM measurements:
1 – LED; 2, 5, and 9 – spherical quartz lenses; 3 – short-pass filters; 4 – dichroic mirror; 6 – sample; 7 – cryostat; 8 – long-pass filter; 10 – monochromator; 11 – photomultiplier module; 12 – photomultiplier amplifier; 13, 16 – bias tee; 14 – lock-in amplifier; 15 – signal generator; 17 – dc power supply; 18 – computer.

detection system. The PL signal is focused by lens (9) onto the entrance slit of a single-pass monochromator (Jobin Yvon H10) (10) or straight into high-speed photomultiplier module (Hamamatsu H6780-01) (11) with response time of 0.78 ns. If needed, the electrical signal can be amplified using the PMT amplifier (Hamamatsu C5594-12) (12). Afterwards, by using another bias tee (13) the electrical signal is decoupled into ac and dc components, which are detected by lock-in amplifier (Stanford Research Systems SR844) (14), which is synchronized with the signal generator (15). The signal from the lock-in amplifier is registered by a computer (18).

The sample excited by an LED output modulated at frequency ω emits light modulated at the same frequency. However, due to the finite luminescence decay time, the detected PL signal has a phase shift φ, and its modulation depth becomes lower by a factor of m. For the simplest case of single-exponential luminescence decay with characteristic time τ, the phase shift and modulation depth can be expressed as [126]:

$$\begin{aligned} \varphi(\omega) &= \tan^{-1}(\omega\tau) \\ m(\omega) &= \frac{1}{\sqrt{1+\omega^2\tau^2}} \end{aligned}. \tag{2.6}$$

For any luminescence decay function $I(t)$, the general phase shift and modulation depth dependences can be expressed as [126]:

$$\begin{aligned} \varphi(\omega) &= \tan^{-1}(N_\omega / D_\omega) \\ m(\omega) &= \sqrt{N_\omega^2 + D_\omega^2} \end{aligned}, \tag{2.7}$$

where N_ω and D_ω are Fourier sine- and cosine-transforms of function $I(t)$:

$$\begin{aligned} N_\omega &= \int_0^\infty I(t)\sin(\omega t)\,dt \Big/ \int_0^\infty I(t)dt, \\ D_\omega &= \int_0^\infty I(t)\cos(\omega t)\,dt \Big/ \int_0^\infty I(t)dt. \end{aligned} \tag{2.8}$$

Since the relation between luminescence decay function *I(t)* and phase shift φ is not direct, but is expressed via Fourier transforms, the extraction of characteristic decay times, especially for multiexponential or nonexponential

decay, is performed by assuming the decay function and adjusting its components for the best fit with experimental results.

3. Carrier dynamics in GaN epilayers

Since GaN is a binary compound, there are no properties related to alloy mixing, and it might be considered as a basic material for the development of green-blue-UV optoelectronic devices and for the nitride research in general. However, even though GaN is the mostly studied group III-nitride compound, if compared to AlN or InN, there are still some not completely resolved problems related to the optical properties and carrier dynamics.

In this chapter, the original results on several of such problems will be presented. The "famous" yellow luminescence band and its correlation with carrier lifetime are studied in section 3.1. Section 3.2 covers the investigations of nonequilibrium carrier dynamics both under high and low excitation conditions. The optical gain coefficient in GaN epilayers and its estimation using VSL technique are discussed in section 3.3. The chapter ends with a short summary.

3.1. Correlation between yellow luminescence intensity and carrier lifetimes in GaN epilayers

The yellow luminescence band in GaN has been widely studied [see for example Ref. 45 and references therein], however, even now, its relation to the structural defects is ambiguous: both correlation [54,59-61] and anticorrelation [62-64] have been reported. In this section, the connection between YL and structural defects is investigated by analyzing the correlation between YL intensity and lifetime of nonequilibrium carriers.

GaN samples under investigation were grown and provided by Sensor Electronic Technology, Inc. The GaN epilayers for this study were grown on sapphire and SiC substrates by low-pressure metalorganic chemical vapor deposition. Trimethyl aluminum (TMAl), triethyl gallium (TEGa) and ammonia (NH_3) were used as Al, Ga, and N sources, respectively. For the

samples grown on sapphire substrate, a 200 Å AlN buffer was grown at 550 ˚C. For the samples grown on 6H-SiC substrates, an AlN buffer layer (~0.1 μm) grown at high temperature (1100 ˚C) was deposited. In each case, the buffer was followed by 1.5-μm-thick GaN layer grown at 1000 ˚C. No intentional doping was used except for n-type silicon doped GaN with silane used as the doping source. The N/III ratio was changed from 1000 to 2000 resulting in different YL intensities.

The GaN epilayers grown on sapphire were characterized by oscillating Kelvin probe technique [127], which allowed estimating the Fermi level in the layers. The electron work function in GaN samples was measured with respect to the work function of the purified mercury electrode (4.75±0.05 eV), and the surface band bending was compensated by the sample illumination. The Fermi level was calculated using the electron affinity value of 3.5±0.1 eV [128] for GaN.

The PL spectra of GaN samples were measured at room temperature under cw excitation by a He-Cd laser (3.81 eV). The carrier lifetimes were measured using a standard EKSPLA, Ltd. module HOLO-2, which uses the light-induced transient grating technique [125], described in more detail in section 2.3. The grating was created by two overlapping beams of the 3rd harmonic (3.49 eV) of the mode-locked YAG:Nd laser radiation (pulse duration 25 ps) and probed by tunably delayed pulses of the 2nd harmonic of the radiation (2.33 eV).

The typical PL spectra for three different GaN samples grown on SiC substrates are shown in Fig. 3.1. As shown by solid lines and arrows, the spectra can be divided into 3 spectral regions, corresponding

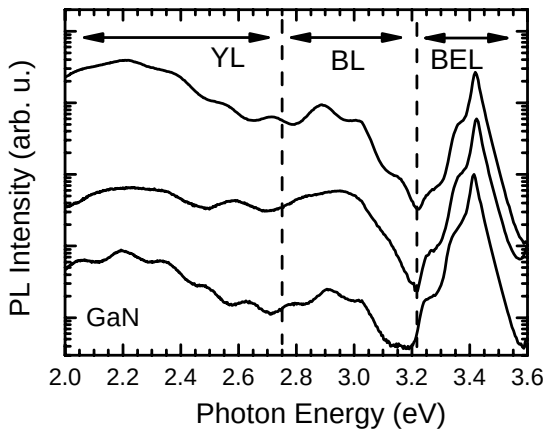

Fig. 3.1. Typical cw PL spectra of three GaN on SiC samples at fixed excitation intensity. The spectra are normalized and arbitrarily shifted for clarity.

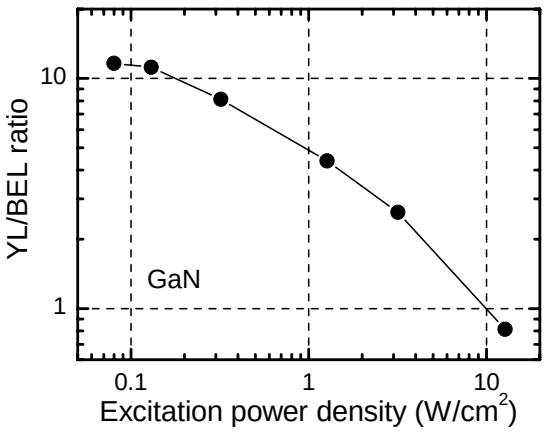

Fig. 3.2. Excitation power density dependence of the ratio of yellow to band edge spectrally integrated luminescence intensities. [After P1]

to different emission bands: the yellow luminescence (YL) band, the blue luminescence (BL) band, and band-edge luminescence (BEL) band. The spectra are normalized with respect to the peak of BEL at ~3.42 eV, and it can be observed that the relative intensity of YL and BL bands is different in different samples. This fact might be related to the difference in growth conditions of GaN epilayers, since the samples were grown under different N/III ratio. For the comparison of different samples, however, a proper care must be taken to ensure that the PL spectra are measured under the same excitation conditions. As can be observed from Fig. 3.2, the ratio of the YL band intensity to that of the BEL band is very sensitive to excitation power density: the YL/BEL ratio rapidly decreases with increasing excitation intensity. Such sensitivity is most probably related to the saturation of recombination centers responsible for YL. Thus, sufficiently low excitation power density should be used for PL measurements.

The diffraction efficiency of the light-induced gratings for several GaN epilayers grown on sapphire is shown in Fig. 3.3. The grating decays exponentially indicating a negligible effect of surface recombination, and the charateristic decay time τ_G, determined by the carrier

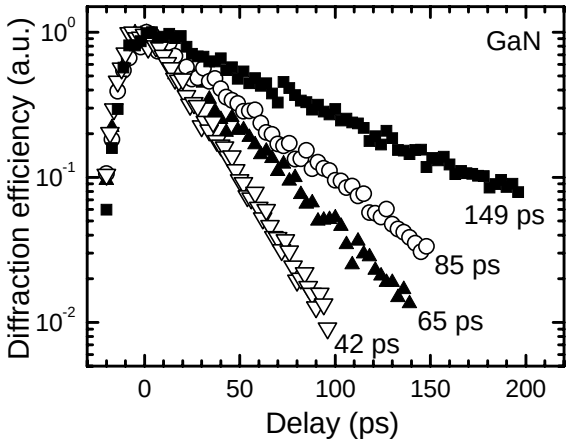

Fig. 3.3. Light induced transient grating decay kinetics in GaN on sapphire samples with different relative YL intensity (corresponding carrier lifetimes are indicated). [P1]

recombination and diffusion, can be expressed through the grating spacing Λ, the ambipolar diffusion coefficient D_a, and the recombination time τ_R by equation (2.5).

Our LITG experiments were performed at comparatively large grating spacing (10.2 μm) ensuring that the influence of diffusion becomes negligible. For such large spacing, the decay is mainly determined by the carrier recombination and the carrier lifetime can be extracted directly from the slope of the decay.

We also studied the distribution of the lifetimes across the sample surface. The estimated error of the lifetime determination is within 10%, which is smaller than the lifetime variation across the sample surface. The observed maximum deviations of the local lifetime from the average lifetime value lay within the range of ~15%, which, in turn, is smaller than the difference in the lifetimes between most of the samples under study. Thus, the carrier lifetime determined by the LITG technique can be attributed to sample characteristics and can be used for comparison of different GaN layers.

The samples under study could be divided into three groups, according to their measured properties: i) GaN layers grown on SiC substrates; ii) GaN semi-insulating samples on sapphire, with the Fermi level close to the middle of the band gap; and iii) *n*-type GaN samples on sapphire, with the Fermi level 500-700 meV below the conduction band.

The epilayers grown on SiC had lifetimes above 100 ps, while most of the semi-insulating YL-containing layers on sapphire had carrier lifetimes shorter than 100 ps. The third group of samples had longer carrier lifetimes in the range from 120 to 150 ps. The YL in the latter samples was negligible with respect to the band edge PL. Such behavior could be explained by the change in the charge state of the defect complexes giving rise to the YL.

The yellow band shape was slightly different in different samples and also had interference fringes caused by multiple reflections within the GaN layers. To minimize the error, the peak intensities of the YL and BL bands were normalized to the peak intensity of the band edge luminescence. Figure 3.4(a)

illustrates a general trend of decreasing YL with increasing lifetimes. A similar dependence was observed for the relative intensity of the blue luminescence [see Fig. 3.4(b)].

For the GaN on SiC samples, we observed a lower relative YL intensity than that for the GaN grown on sapphire under similar growth conditions. However, the decrease in YL/BEL ratio with increasing carrier lifetimes was observed to be similar for the GaN/SiC samples [see Fig. 3.5(a)]. The BL component in GaN/SiC layers is stronger as compared to the YL component than that in GaN grown on sapphire, but the general trend is the same as in Fig. 3.4.

The carrier lifetime in GaN layers at room temperature is determined by nonradiative recombination, and a lower lifetime means higher concentration of nonradiative recombination centers. A lower carrier lifetime in the samples with stronger YL demonstrates that the defects responsible for the *radiative* recombination resulting in the YL band are also involved in *nonradiative* recombination. This is consistent with the assumption that the YL is a result of recombination at complex centers consisting of structural defects and

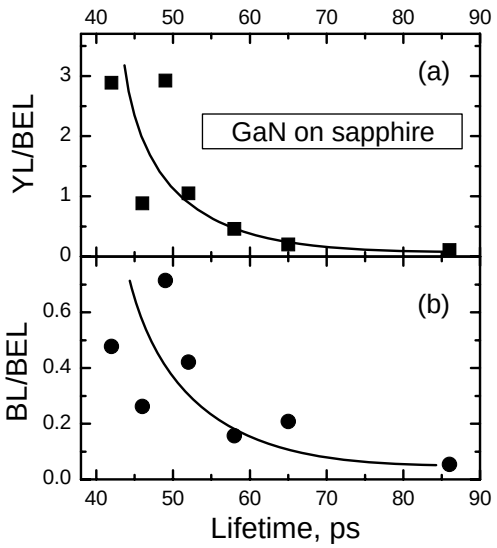

Fig. 3.4. Ratio of yellow (a) and blue (b) luminescence intensity to band-edge luminescence intensity for GaN on sapphire samples with different lifetimes. The lines are a guide for the eye. [P1]

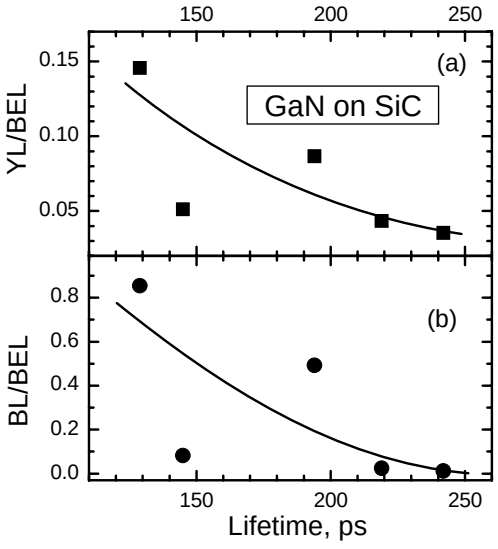

Fig. 3.5. Ratio of yellow (a) and blue (b) luminescence intensity to band-edge luminescence intensity for GaN on SiC samples with different lifetimes. The lines are a guide for the eye. [P1]

impurities [54,59-61], which might form the centers for radiative and nonradiative recombination.

To summarize, the study of GaN epilayers grown on different substrates under different conditions revealed the correlation between carrier lifetime and defect-related luminescence bands (YL and BL). Both for GaN/sapphire and GaN/SiC layers, the samples with a higher YL intensity have a lower carrier lifetime. This implies that structural defects bound into complexes with impurities might be responsible for both the radiative recombination resulting in YL (and BL) and for the nonradiative recombination limiting the lifetime of nonequilibrium carriers.

3.2. Investigations of nonequilibrium carrier dynamics in GaN epilayers

Studies of carrier dynamics strongly depend on the excitation conditions. Therefore, this section is divided into two sub-sections, depending on excitation level used in experiments: in sub-section 3.2.1, carrier dynamics under high excitation conditions are discussed, while results on carrier dynamics under extremely low excitation conditions are presented in sub-section 3.2.2.

3.2.1. Carrier dynamics under high excitation conditions

The high excitation conditions are similar to those in real operating devices: the high densities of injected carriers ensure that the trapping and defect-related recombination centers are saturated and do not significantly affect the carrier lifetimes. The determination of carrier lifetime is most commonly performed by using time-resolved photoluminescence spectroscopy. However, the interpretation of TRPL results is somewhat ambiguous, especially when a multi-exponential PL decay is observed [87,95-98,100,103,105]. In this sub-section, the studies of PL decay by TRPL technique are compared to the results

obtained by another optical method, LITG technique [125], and certain peculiarities of these two methods are revealed.

GaN samples under investigation were grown and provided by Sensor Electronic Technology, Inc. GaN epilayers used in this study were deposited on high-quality AlN buffer layers grown on sapphire using MEMOCVD^{TM} technique. In all the growth runs, trimethyl aluminum, trimethyl gallium, and ammonia were used as Al, Ga, and N sources, respectively. The growth temperature and pressure for the buffer layer were 1100 °C and 40 Torr, respectively. The growth method is described in more details elsewhere [16-18]. The subsequent GaN layers were grown by low-pressure metalorganic chemical vapor deposition at 1000 °C and 76 Torr. The V/III ratio was modified from 750 to 2000, and the growth rate of the GaN was typically 1.5-1.8 μm/h. The higher V/III ratios resulted in higher carrier lifetimes in the epilayers. To reduce the dislocation density in the epilayers, thick GaN layers (up to the thickness of 10 μm) have been grown at higher V/III ratio. These thicker samples show low dislocation densities and the highest carrier lifetimes (>2 ns). All the samples were unintentionally *n*-type doped at typical carrier concentrations of 5×10^{16}-10^{17} cm^{-2}.

All of the measurements have been carried out at room temperature. The PL decay kinetics were measured using the setup described in section 2.2 under excitation by the 4th harmonic (4.66 eV) of the mode-locked YAG:Nd laser (pulse duration 25 ps). The carrier lifetimes were estimated using the LITG technique [125], described in more detail in section 2.3. The grating was created by two overlapping beams of the 4th harmonic (4.66 eV) and probed by tunably delayed pulses of the 2nd harmonic (2.33 eV) of the same YAG:Nd laser.

The diffraction efficiency decay for the GaN epilayer with the longest carrier lifetime is shown in Fig. 3.6 for several grating spacings. As illustrated by the solid lines, the decay can be well described by an exponential function. The grating decays mainly due to carrier recombination and diffusion with the relative contribution of the processes depending on grating spacing Λ,

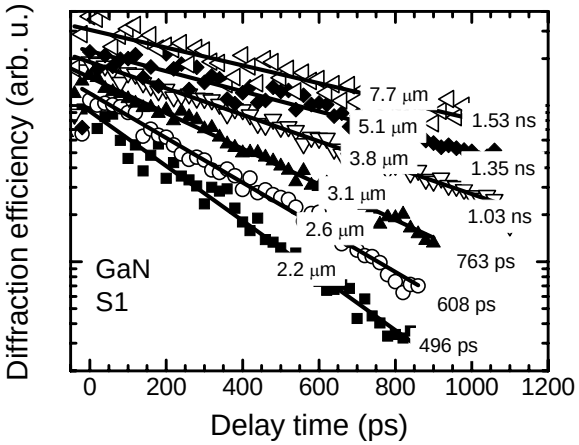

Fig. 3.6. Light induced transient grating decay kinetics for GaN sample S1 at different grating spacings (indicated). The estimated grating decay times is also indicated. [After P4,P5]

according to equation (2.5). As can be observed in Fig. 3.6, the grating decay time changes from ~500 ps at 2.2 μm grating to ~1.5 ns at 7.8 μm grating. The dependence of grating decay time on grating spacing is separately shown in Fig. 3.7. Using the best fit according to Eq. (2.5), both the carrier lifetime and the ambipolar diffusion coefficient were extracted. For the sample S1 shown in Fig. 3.7, the estimated values were τ_R = 2 ns, and D_a = 1.9 cm^2/s.

The PL spectra of GaN samples at room temperature show some narrowing and shift during the PL decay, but do not indicate any changes in the recombination mechanisms. Thus, to analyze the decay, we used a spectrally integrated PL intensity. Figure 3.8 shows typical decay kinetics for several GaN samples. When measured within a large dynamic range, the PL decay is usually nonexponential. Typically, such PL decay was approximated by a sum of two exponential components [87,95,96,98,100,103,105] and assigned to carrier capture into deeper centers followed by recombination [103]. The longer decay time was assumed to reflect the carrier lifetime. Here, in another approach, we show that the

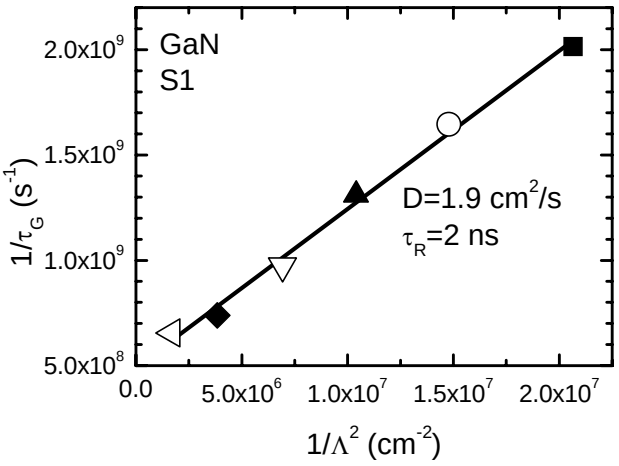

Fig. 3.7. LITG decay time vs grating spacing measured in the GaN sample S1. The diffusion coefficient and carrier lifetime estimated using equation (2.5) are indicated. [After P4,P5]

nonexponentiality of PL decay can be explained without assuming multilevel system, and this assumption is in consistence with LITG results.

The PL decay is mainly governed by the nonequilibrium carrier density dynamics. To simplify our analysis, we assume that the Shockley-Read-Hall recombination centers are saturated, which is a reasonable assumption at the high excitation intensities under our experimental conditions. Thus, the nonequilibrium electron and hole densities can be considered to be equal ($\Delta n = \Delta p$), and the dynamics of the nonequilibrium electron density obeys the rate equation:

$$\frac{d\Delta n}{dt} = G - \frac{\Delta n}{\tau} - B \cdot \Delta n^2, \tag{3.1}$$

where G, τ, and B are the generation rate, the lifetime, and the coefficient of the bimolecular band-to-band recombination, respectively. Since the PL decay rate is different in different samples, it is reasonable to assume that the carrier density decay is dominated by the nonradiative recombination [decribed by the second term on the right-hand side of Eq. (3.1)] rather than by the radiative recombination with the rate defined by the coefficient of the bimolecular recombination, B. Since all the samples were n-type, we can neglect the equilibrium hole density, and luminescence intensity depends on the equilibrium, n_0, and nonequilibrium, Δn, electron densities (with the photogenerated hole density $\Delta p = \Delta n$) as:

$$I_{LUM} \propto B \cdot \Delta n \left(\Delta n + n_0 \right). \tag{3.2}$$

At the very beginning of the decay, the third term on the right-hand side of Eq. (3.1) might play a significant role. Moreover, the carrier heating and stimulated emission [129,130] might also influence the initial decay. However, later on, after the first and the third terms in Eq. (3.1) become negligible, the nonequilibrium carrier density, Δn, decays exponentially, with the characteristic lifetime τ. As long as $\Delta n \gg n_0$, I_{LUM} decay is also exponential with a time constant $\tau/2$. In the opposite limiting case, when Δn becomes negligible compared to n_0, the I_{LUM} decay approaches another exponent with the characteristic time τ. In addition, the saturation of the centers of

nonradiative recombination [131,132] might also influence the transition from $\tau/2$ decay to τ decay. Thus, the PL decay is quite complex, and the extraction of the carrier lifetime is somewhat ambiguous. Moreover, if samples with different n_0 are to be compared, the transition from $\tau/2$ to τ in the exponent of the decay occurs at different Δn and, consequently, at different delays after the excitation, which makes the comparison even more difficult. However, fitting the experimental PL kinetics with the biexponential decay function with decay times of $\tau/2$ and τ:

$$I_{LUM} \propto A\exp\left(-\frac{t}{\tau/2}\right)+B\exp\left(-\frac{t}{\tau}\right), \tag{3.3}$$

where τ is the carrier lifetime extracted from LITG measurements, and A and B are adjustable parameters, results in good agreement. Fitting shown in Fig. 3.8 by solid lines has been carried out using such biexponential approach and the values of τ extracted by applying the LITG technique. The biexponential regime corresponding to an exponential decay of Δn is reached after approximately 1.5 ns for samples S1 and S2, 0.24 ns for sample S3, 0.4 ns for sample S4, and 0.02 ns for sample S9. The two limiting cases of $\Delta n \gg n_0$ and

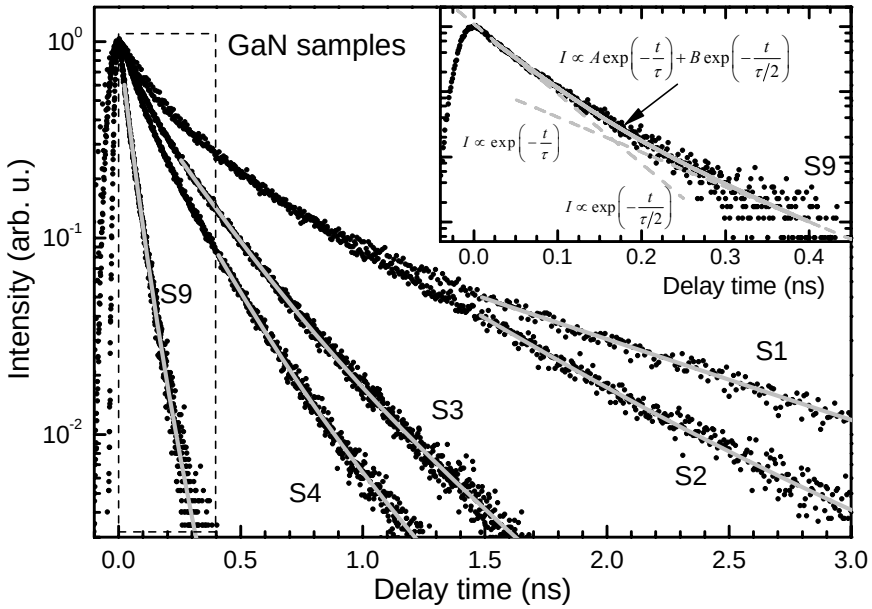

Fig. 3.8. Spectrally integrated PL decay kinetics (points) of five GaN samples and two-exponential fit (solid lines) using Eq. (3.3) with the lifetimes extracted from LITG experiments. The inset shows the expanded PL decay curve (points) for sample S9. The limiting cases of single-exponential decay and the total decay function are shown by solid lines. [After P4,P5]

$\Delta n \ll n_0$ and the total decay function are illustrated in the inset of Fig. 3.8 for the sample S9. The ratio of B/A is sample dependent and ranges from 0.15 for sample S9 to 0.03 for sample S1. Thus, the major part of the fitting range is dominated by the decay with the characteristic time $\tau/2$.

The initial PL decay region, which could not be fitted using this approach, is most probably related to the carrier diffusion to the sample depth and PL reabsorption, since these two processes as well as surface recombination strongly influence the PL decay curves for thick epilayers and/or epilayers having long carrier lifetimes [101,106]. Indeed, as the carrier lifetime decreases, the adequate range of biexponential fit increases (see Fig. 3.8), as the carriers fail to diffuse far enough to the depth.

In addition to the determination of the lifetimes, the LITG technique provides the values of the ambipolar diffusion coefficient. Such simultaneous determination of τ and D enables the estimation of the diffusion length $L_D = \sqrt{D\tau}$. We calculated the diffusion lengths for nine GaN samples under study and revealed the correlation between the lifetime and diffusion coefficient (mobility) of the carriers in GaN. Figure 3.9 shows the correlation between the diffusion length and the carrier lifetime. Except for the samples with the longest carrier lifetimes, the diffusion length L_D in these samples is nearly the

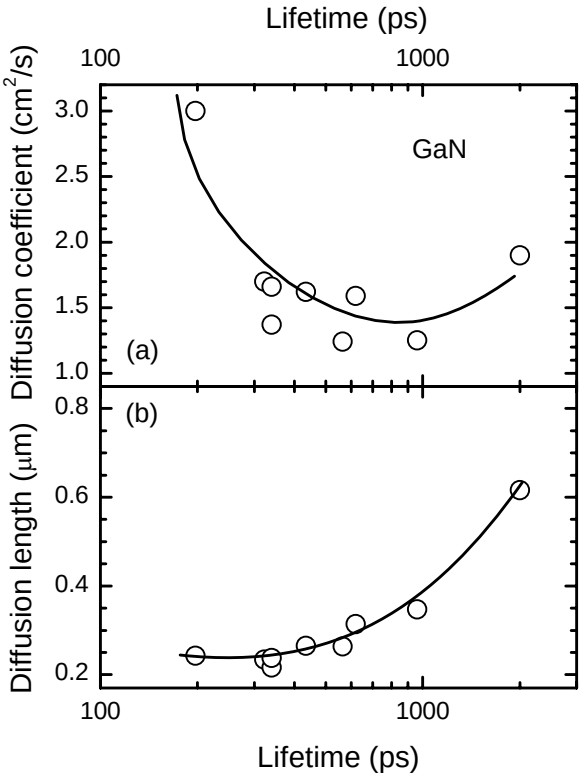

Fig. 3.9. Carrier diffusion coefficient (a) and diffusion length (b) vs carrier lifetime in GaN epilayers on sapphire substrates grown under various conditions. The lines are a guide for the eye. [After P4,P5]

same for all the samples. Apparently, in the samples with a lower mobility (i.e., a lower diffusion coefficient), the carriers need a longer time to reach the recombination centers where they recombine (most likely, nonradiatively). This makes sense if nonradiative recombination occurs at certain defects (most probably, dislocations) having approximately the same density in different samples. Note that the carriers can radiatively recombine while moving towards the dislocations. The longer they move, the more time they have to recombine radiatively. Hence, the PL should be more intense in the samples with a lower mobility (but a longer lifetime). We observe this feature by comparing the PL intensities in the set of the samples with similar diffusion lengths (see Fig. 3.10).

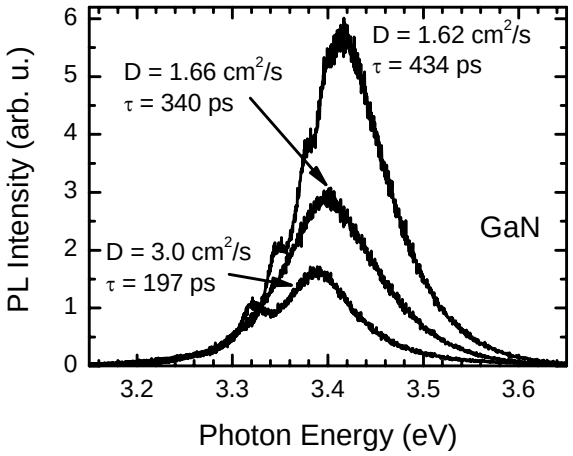

Fig. 3.10. PL spectra for three GaN samples with different diffusion coefficient and carrier lifetime (indicated).

The dislocation densities estimated by the etch pit technique in most of the GaN samples are in the range 3-5×10^9 cm^{-2}. (This is the dislocation density in all of our samples with the exception of sample S1.) Under rough assumption of homogeneous dislocation distribution, the dislocation density $N_{dd} = 4\times10^9$ cm^{-2} corresponds to the average distance between two first-neighbor dislocations $2\cdot r_{dd} \approx 0.2$ μm, according to the simple relation $N_{dd} = 1/\pi r_{dd}^2$. Thus, taking into account a random distribution of the dislocations, the diffusion length of 0.25 μm, which was extracted for most of the samples from our LITG experiments, is quite close to the distance, which the nonequilibrium carriers have to travel to reach the nearest dislocation. This conclusion supports the assumption that the nonradiative recombination occurs in the vicinity of dislocations.

In the samples with lifetimes above ~1 ns, both their carrier lifetime and mobility increase. In sample S1, the dislocation density is reduced down to 10^8 cm^{-2}, and the room temperature lifetime of 2 ns observed in this epilayer is extremely long, well above even the lifetime of 970 ps estimated at room temperature in homoepitaxial GaN [83] or 860 ps in the GaN sample grown by the epitaxial lateral overgrowth [87]. The hole mobility in the sample S1 is also quite high. Under assumption that the diffusion coefficient for electrons, D_e, is much higher than that for holes, D_h, the ambipolar diffusion coefficient $D_a = 2D_h$. The D_a value of 2.1 cm^2/s obtained by LITG technique in the sample S1 corresponds to the hole room-temperature mobility of 41 $cm^2V^{-1}s^{-1}$. These values obtained for sample S1 (and smaller but still high values obtained for other samples under study) indicate a high material quality and certify MEMOCVD^{TM} growth technique as a very fruitful approach for the deposition of high-quality nitride epitaxial layers.

To summarize, the comparison of results on nonequilibrium carrier decay kinetics using TRPL and LITG techniques provides a clear insight into the interpretation of the room-temperature PL decay. Fitting of the decay by two exponents corresponding to the carrier lifetime and to one-half of it is suggested as means to extract the carrier lifetime from the TRPL measurements. The simultaneous determination of the carrier lifetime and of the diffusion coefficient showed that, in the GaN samples, where the carrier lifetime is limited mainly by nonradiative recombination at dislocations, higher carrier mobility shortens the carrier lifetime, since the carriers reach the dislocations faster. We also demonstrated the ability of MEMOCVD growth technique to grow high-quality GaN epilayers with dislocation densities as low as 10^8 $cm^{-2}$and carrier lifetimes exceeding 1 ns.

3.2.2. Carrier dynamics under extremely low excitation

At low densities of nonequilibrium carriers, the recombination centers are not saturated, and carrier trapping or decay via defect levels might strongly impact

carrier dynamics. In this sub-section, the carrier dynamics under extremely low excitation conditions in a high-quality GaN sample is discussed.

The GaN epilayer under study was selected from a set of GaN samples, which were investigated under high excitation conditions and discussed in section 3.2.1. The sample S1 with the highest carrier lifetime of ~2 ns was chosen.

The sample was investigated by photoluminescence spectroscopy and frequency domain lifetime measurements. The PL spectra were measured using the setup described in section 2.1. A He-Cd laser (3.81 eV) and a 280 nm UV LED (4.43 eV) were used for excitation. The same 280-nm-LED was used for excitation also in FDLM experiments, described in more detail in section 2.4. All the measurements were performed in a wide temperature range of 8-300 K.

The primary characterization of the GaN epilayer was performed by examining the PL spectra under very low excitation conditions. The temperature evolution of PL was examined to check the possible appearance of new recombination mechanisms with temperature. Figure 3.11 shows the cw PL spectra of the GaN sample at 8 K temperature and excitation power density ranging from 0.5 mW/cm^2 (UV LED excitation) to 0.1 W/cm^2 (He-Cd laser

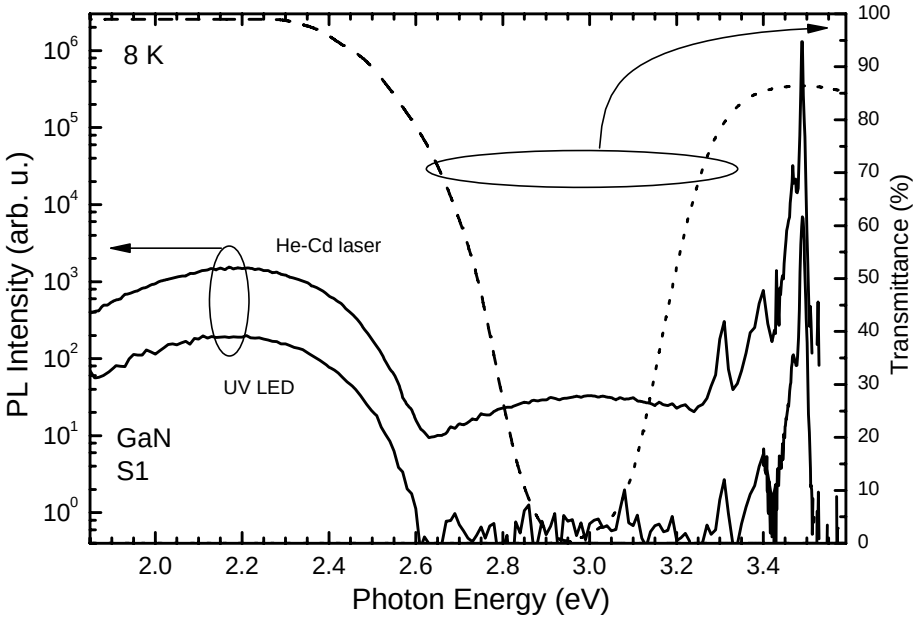

Fig. 3.11. PL spectra of GaN sample S1 measured at 8 K under He-Cd laser excitation (~100 mW/cm^2) and UV LED excitation (~0.5 mW/cm^2). Dashed and dotted lines show the transmission spectra of the filters used to select either the yellow band or UV region. [C10]

excitation). The spectrum can be divided into typical for GaN bands: i) the narrow and sharp band peaked at 3.4895 eV, assigned to the excitonic recombination, followed by two phonon replicas; ii) blue luminescence (BL) band, peaked at ~3 eV; iii) yellow luminescence (YL) band, peaked at ~2.2 eV. As illustrated for 8 and 300 K temperatures, the intensity of the BL band decreases with decreasing excitation power density faster than that of the YL band in the entire measurement temperature range between 8 and 300 K (see Fig. 3.12). As a result, only the YL band and near-band-edge emission are observed in the spectrum of the sample excited by UV LED.

According to the spectral position, at the lowest temperatures the band-edge emission is dominated by bound exciton recombination, switching to free exciton emission at elevated temperatures and, probably, to band-to-band recombination at temperatures close to the room temperature. The intensity of the near-band-edge emission decreases nearly by four orders of magnitude with increasing temperature with the rate of the decrease being independent of the excitation power density [see Fig. 3.13(a)]. Meanwhile, the dynamics of the YL intensity with increasing temperature follow a completely different trend [see Fig. 3.13(b)]. Under the He-Cd laser excitation, the intensity decreases with the temperature increase up to ~50 K, is nearly constant within the temperature range up to ~150 K, and decreases further at higher temperatures. Under the UV LED excitation, the initial temperature increase

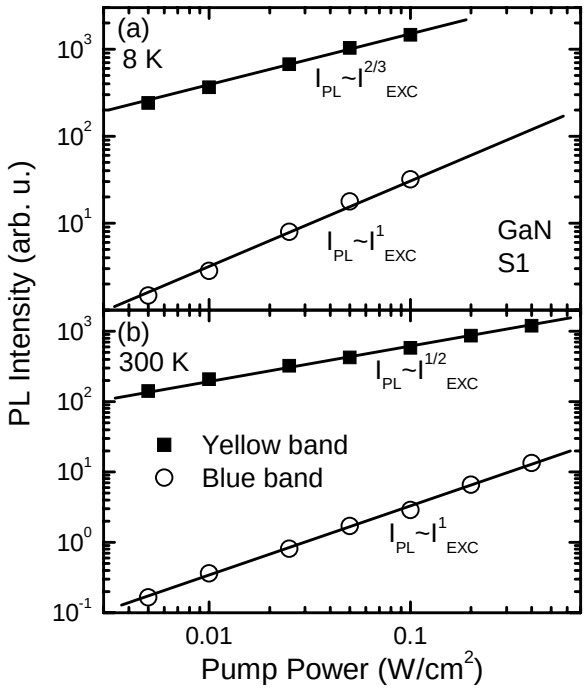

Fig. 3.12. Excitation power density dependences of the yellow and blue band intensities. Dependences were measured under excitation by He-Cd laser at 8 K (a) and 300 K (b) temperatures. [C10]

up to approximately 100 K causes an increase in the YL intensity. A further increase in temperature (up to room temperature) results in the decrease of the YL intensity down to approximately 80% of the level observed at 8 K.

The two spectral regions of the GaN PL were analyzed separately in FDLM experiments. Since FDLM were performed under the same UV LED excitation, the spectrum consisted of only two bands, which were separated using different sets of optical filters. The transmission spectra of the filter sets are shown by dashed and dotted lines in Fig. 3.11. In such a way, we analyzed the decay times associated with YL and near-band-edge (NBE) luminescence separately. To see the competition between the different recombination channels we performed FDLM experiments in the temperature range from 8 to 300 K.

The phase shift frequency dependences for the luminescence in the UV region are shown in Fig. 3.14 for several temperatures. The phase shift curves have two features in the entire temperature range. The phase shift increases with increasing frequency up to ~1 kHz. A further frequency increase results in the phase shift drop due to a faster decay component that starts to dominate but is too fast to show any phase shift in this intermediate frequency range. An increase in the phase shift due to this component is observed in the

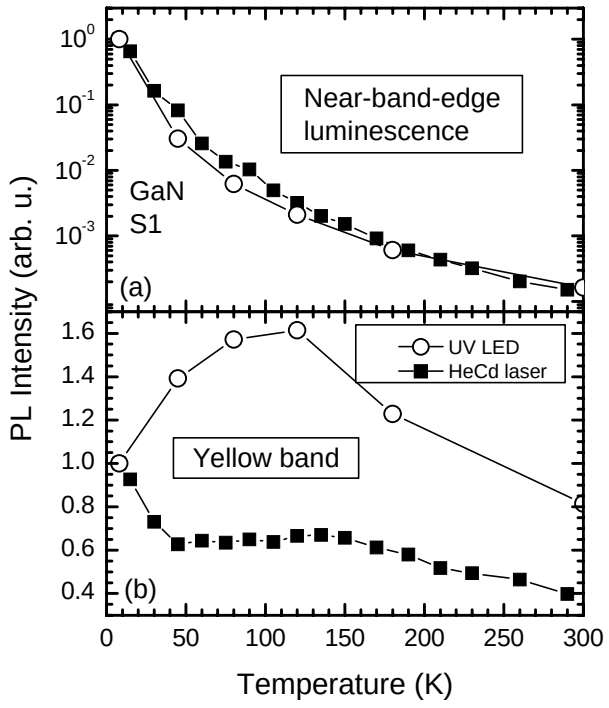

Fig. 3.13. Temperature dependence of the intensities of the near-band-edge luminescence (a) and yellow band (b) under two different excitation conditions (indicated). Excitation power densities were 0.5 mW/cm^2 for UV LED and 50 mW/cm^2 for He-Cd laser. The curves were normalized with respect to their low-temperature intensities. [C10]

high-frequency edge of the frequency range under study. As shown by the solid line in Fig. 3.14, the phase shift frequency dependence in the entire frequency range can be fitted by superposition of two exponential decay functions with decay times of 500 μs and 200 ps. The slow decay component increases with the temperature increase from 8 K to ~100 K, then starts decreasing with a further increase in temperature and disappears below noise level at temperatures above ~140 K. These processes happen in parallel with strong quenching of the NBE PL intensity with increasing temperature {by two orders of magnitude in the range from 8 to 100 K [see Fig. 3.13(a)]}. The fast component stays the same throughout the entire temperature range.

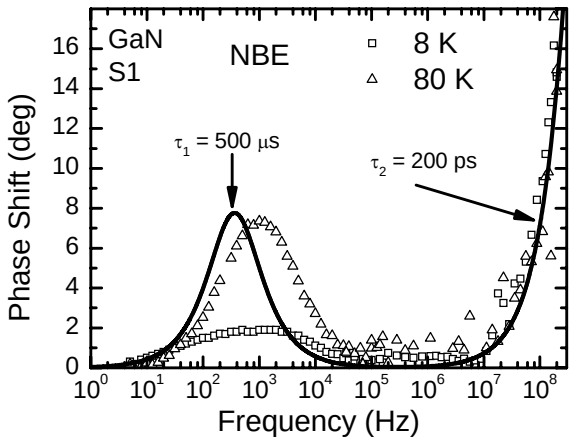

Fig. 3.14. Frequency dependence of the phase shift for luminescence in the NBE region for GaN at different temperatures (indicated). The solid line is a fitted curve (see details in the text).[After P10]

Figure 3.15 presents the phase shift curves for the YL band at several temperatures. The situation is more complicated than for the NBE luminescence case, and three temperature-dependent components can be observed. The phase shift increase in the 5 Hz to 30 kHz range observed at temperatures below ~40 K was too slow to be described by an exponential decay. Thus, we assumed that this feature is caused by donor-acceptor pair (DAP) recombination, which has previously been observed in GaN [88,133]. The luminescence intensity decay in the case of a random distribution of DAPs can be expressed as [89]:

$$I(t) \propto N \exp\left\{4\pi N \int_0^\infty \left[e^{-W(R)t} - 1\right] R^2 dR\right\} \times \int_0^\infty W(R) e^{-W(R)t} R^2 dR, \qquad (3.4)$$

where N is the concentration of the majority constituent in DAPs, and $W(R)$ is separation-dependent radiative recombination rate expressed by equation (1.5). The best fit was achieved for the DAP density $N = 2.2\times10^{17}$ cm^{-3} (close to the

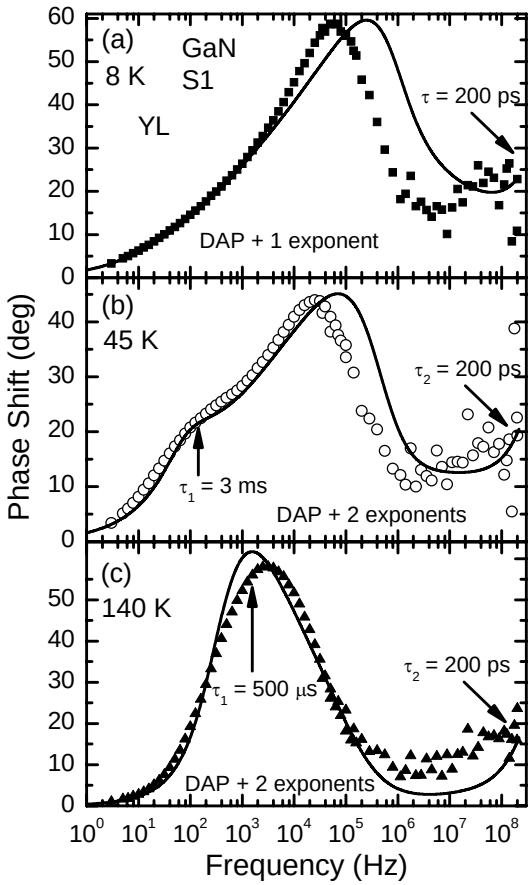

Fig. 3.15. The phase shift frequency dependence of the YL band in GaN (points) for three typical temperatures (indicated). Solid line show the best fit curves (see text). [After P10]

equilibrium carrier concentration at room temperature), $a_D = 24$ Å (which corresponds to a shallow donor with activation energy of 30 meV in the effective mass approximation [90,134]), and $W_{max} = 4\times10^6$ s^{-1} (similar to the values reported previously [90,134]). To reproduce the drop in the phase shift at the high-frequency limit [see Fig. 3.15(a)], a fast exponential decay component with decay time of 200 ps (like for the NBE luminescence) was included in the fitting function. This decay component, which might be even faster than 200 ps, persists throughout the entire temperature range under study (200 ps were close to the time resolution in our experiments).

At elevated temperatures, a new exponential decay component emerges [see Fig. 3.15(b)]. Its decay time decreases from ~10 ms at 30 K to ~500 μs at 100 K. Above 100 K temperature, the decay time shows no significant change and the exponential component with $\tau = 500$ μs dominates over the DAP recombination component [see Fig. 3.15(c)]. It is reasonable to assume that this component is caused by the optical transitions between the conduction band and acceptors. It replaces the DAP recombination when the donor states involved in DAP recombination become thermally ionized. The value of the potential barrier (i.e. the depth of the donor level) extracted from the temperature dependence of τ is ~15 meV. This is close to the values reported previously (20-30 meV) [52,133,135].

The fitting procedure was aimed not at the best fit of particular phase shift frequency dependence but rather at revealing the minimal number of decay components needed to describe the PL decay in both spectral regions and in the entire temperature range under study. As a result, the observed complex behavior of the carrier dynamics at a low density of nonequilibrium carriers can be explained within the band model with experimentally obtained parameters (see Fig. 3.16). The YL at low temperature is caused by DAP. The donor level involved in these transitions ($\Delta E_D \approx 15$ meV below the conduction band) is thermally ionized at elevated temperatures, and the band to acceptor (e-A) recombination becomes dominant in the formation of the YL band. Since the band is broad in comparison with ΔE_D, the change in recombination mechanism is hardly observable in the spectrum, but is obvious in the time-resolved characteristics of the emission.

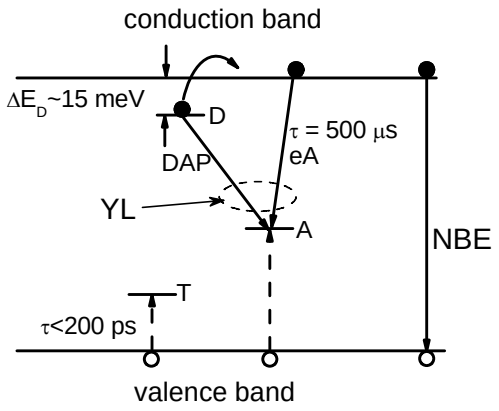

Fig. 3.16. The band model illustrating the carrier dynamics in GaN. D stands for donor, A stands for acceptor, and T is the trap level. Solid lines indicate radiative transitions; dotted lines correspond to nonradiative transitions. [P11]

The fast decay component ($\tau \leq 200$ ps) at low temperatures is probably caused by recombination via bound exciton states. This recombination channel competes with the capture of holes by the DAP centers and, thus, contributes to the YL dynamics. Thermal ionization of bound excitons at intermediate temperatures is the source of free holes and results in the slower component in the NBE recombination. The decay of this weak component is caused by the decay of the electron density due to e-A recombination with the characteristic time of ~500 μs. This component, however, disappears at higher temperatures due to trapping of holes to trapping levels deep enough not to be thermally ionized even at room temperature. Most probably, the density of the traps is low enough to be saturated at higher densities of nonequilibrium

carriers. However, these traps are important at extremely low excitation levels and might affect the carrier dynamics at the late stages of carrier density decay after pulsed excitation.

To summarize, nonequilibrium carrier dynamics was studied in a high-quality GaN epilayer exhibiting a carrier lifetime of 2 ns at room temperature. The FDLM technique enabled us to perform the study at an extremely low excitation power density (~0.5 mW/cm^2) and to reveal the competition between recombination mechanisms responsible for YL in GaN at nonequilibrium carrier densities below the saturation of the energy levels involved in these recombination channels.

3.3. Saturated gain in GaN epilayers studied by variable stripe length technique

The most commonly used technique for estimation of optical gain coefficient is the variable stripe length technique [80]. In this sub-section, the limitations of the VSL technique for measurements of high optical gain values in GaN epilayers are discussed. The optical gain in two GaN samples with different carrier lifetimes is compared.

The two GaN epilayers under study were selected from a set of GaN samples, investigated under high excitation conditions and discussed in section 3.2.1. The samples S1 and S2 were chosen. The estimated carrier lifetimes were ~2 ns and 960 ps in samples S1 and S2, respectively (see section 3.2.1 for more details). The thicknesses of the samples were 11 μm and 2 μm for the samples S1 and S2, respectively. Dislocation densities estimated using the etch pit technique were 10^8 and 4×10^9 cm^{-2} for samples S1 and S2, respectively.

Peculiarities of the optical gain in GaN epilayers have been studied using the VSL technique described in more detail in section 2.1. The 4th harmonic (4.66 eV) of the Nd:YAG laser has been used for sample excitation. The optical gain properties have been first studied in sample S1, and the peak gain

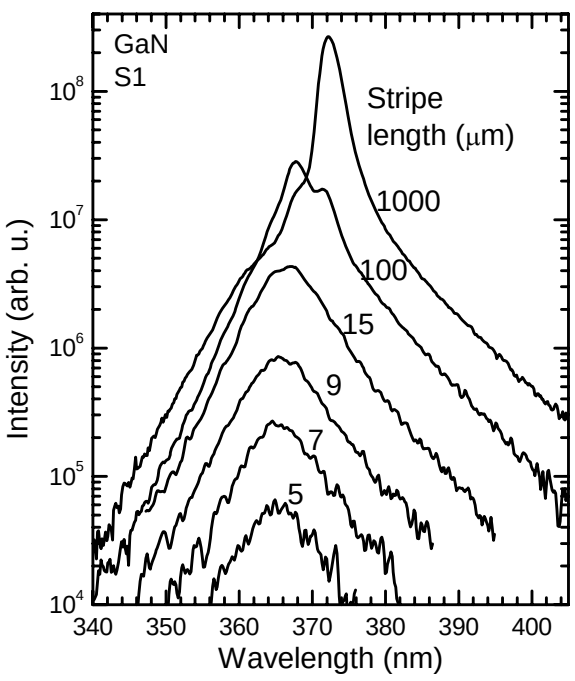

Fig. 3.17. Spectra of the edge emission of sample S1 measured at different stripe lengths (indicated) and constant excitation power density of 2 MW/cm^2. [P6]

values of two samples S1 and S2 (grown in different conditions, as described above) have been compared afterwards. In sample S1, the edge emission amplified along the photoexcited stripe on the surface appears when the excitation power density, I_{ex}, exceeds ~100 kW/cm^2, and its intensity increases with increasing I_{ex} approximately as $I_{em} \propto I_{ex}^3$, which is typical for stimulated emission band.

At high excitation intensities, the emission spectrum depends on the excitation stripe length. Figure 3.17 shows this dependence for the constant excitation power density of 2 MW/cm^2, which is rather high as compared to the threshold for unrecoverable optical damage of the sample surface (~10 MW/cm^2). For short stripe lengths, the edge emission peaks at 365.3 nm (3.393 eV). This position is slightly redshifted with respect to the spontaneous emission band peak at 362 nm (3.42 eV), which is observed in the conventional front-surface configuration.

As the stripe length is increased, the edge emission peak further redshifts, and a new band appears at 372 nm. The existence of several peaks in the spectrum changing with increasing stripe length might be caused by different propagation conditions for different wavelengths, even though the samples under study contained no waveguiding layers. The redshift of the edge emission band we observe with increasing stripe length in GaN is similar to that previously observed in InGaN multiple quantum wells [85]. At long stripe lengths, the stimulated transitions reduce the electron-hole pair density and,

thus, lower the Fermi energy. As a result, the gap between the electron and hole quasi-Fermi-energies becomes lower than the energy of photons in the high-energy tail of emission band. Thus, the optical gain turns to absorption in this spectral region. Meanwhile, the increasing volume of the excitation stripe ensures an increase of the total emission intensity in the spectral regions of the positive gain (the low-energy side of the emission band). Thus, the high-energy side of the emission band is saturated more rapidly than the low-energy side, and the edge emission redshifts.

The gain saturation is obviously revealed by the stripe length dependence of the edge emission intensity. Figure 3.18 presents such dependence for two band peaks seen in the spectra in Fig. 3.17: 365 nm, corresponding to the peak position for the short stripe, while 372 nm is the peak position of the band prevailing at long stripe lengths. The gain saturation is obvious for both peaks, though it occurs at different stripe lengths for 365 and 372 nm peaks. The exponential stripe length dependence of the edge emission intensity predicted by Eq. (1.4) is observed only in a very short range, up to approximately $L = 10$ μm [as shown in more details in Fig. 3.18(b)]. The data for very short stripe lengths (below ~2 μm) are unreliable due to light diffraction at the blocking screen edge and the light scattering at the sample edge. Therefore the range for reliable gain estimation is quite narrow for the observed high gain values. For sample S1, the value of $g = 7300$ cm^{-1} can be estimated from Fig. 3.18 by fitting the experimental data using Eq. (1.4). Higher gain values could probably be observed at higher

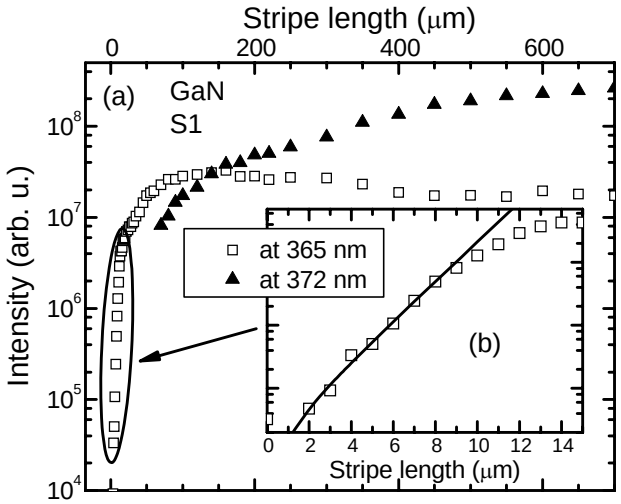

Fig. 3.18. Stripe length dependence of the edge emission intensity of sample S1 at the band peak positions of 365 and 372 nm. In the inset, the initial part of the dependence is fitted by expression (1.4). [After P6]

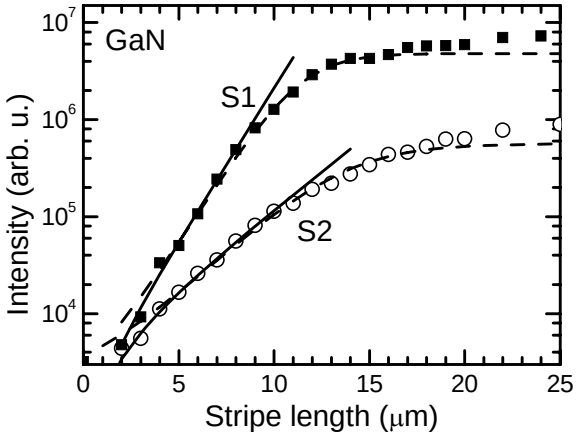

Fig. 3.19. Stripe length dependence of stimulated emission propagating along the sample surface for samples S1 (squares) and S2 (circles). Lines represent the best fit with Eq. (1.4) (solid) and Eq. (3.5) (dashed). [P6]

excitation power densities. However, estimation of the values becomes unreliable.

The intensity of the emission band peaked at 365 nm starts saturating at stripe lengths exceeding ~10 μm (see Fig. 3.18). This occurs at stripe length values when the edge emission spectrum (see Fig. 3.17) starts to redshift. That is consistent with the assumption that the gain at longer wavelengths (though being lower than the gain at shorter wavelength) is sustained for longer stripe lengths, even after the gain on the short-wavelength side is saturated. At the stripe lengths exceeding ~600 μm, the gain is saturated even at the band peak position redshifted to 372 nm.

The gain saturation limits the stripe length range available for fitting the experimental data using Eq. (1.4). For sample S1, a fairly good fit could be obtained only in the range up to ~10 μm, as shown in Fig. 3.19 by a solid line. The range of the stripe lengths, which are suitable for the fitting, might be extended by introducing a gain saturation factor in the rate equation describing light propagation along the excited stripe. Such approach was successfully applied for gain analysis in GaN-based quantum well lasers [86]. The edge luminescence intensity dependence on stripe length in this case is expressed as [86]:

$$I(h\nu,l)=\frac{I_0(h\nu)}{1+C(h\nu)\exp(-g_0 l)}+\frac{I_0(h\nu)}{1+C(h\nu)}, \tag{3.5}$$

where I_0, C, and g_0 are the saturation intensity, saturation coefficient, and unsaturated gain coefficient, respectively. The best fit using this approach is depicted by a dashed line in Fig. 3.19. As seen, the fitting range was extended by a factor of ~2, while the extracted gain value (7500 cm^{-1}) is close to the

value of 7300 cm^{-1} estimated using Eq. (1.4). However, this approach still does not describe the further increase of the edge luminescence intensity at stripe lengths higher than 20 μm.

In principle, the VSL technique allows one to extract the entire gain spectrum, since Eq. (1.4) can be applied for multiple wavelengths. Thus, in the absence of saturation, the gain spectrum can be extracted from two edge emission spectra, measured at stripe lengths L and $2L$, using the following expression:

$$g(h\nu) = \frac{1}{L}\ln\left[\frac{I(h\nu, 2L)}{I(h\nu, L)} - 1\right], \tag{3.6}$$

which follows from Eq. (1.4). To avoid the influence of saturation, the gain spectrum at high excitation intensities has to be extracted using the spectra obtained at short stripe lengths of the order of several micrometers. The gain spectra extracted for sample S1 at L = 3 and 5 μm are shown in Fig. 3.20. The spectra demonstrate evident saturation effect even for the pair of stripe lengths of L = 5 μm and $2L$ = 10 μm. Consequently, the VSL technique is hardly applicable to extract the gain spectrum in highly excited high-quality GaN epilayers. The peak gain value of 6500 cm^{-1} obtained from the gain spectra in Fig. 3.20 is also less reliable than the values obtained by fitting the stripe length dependence of the edge emission intensity at a fixed wavelength.

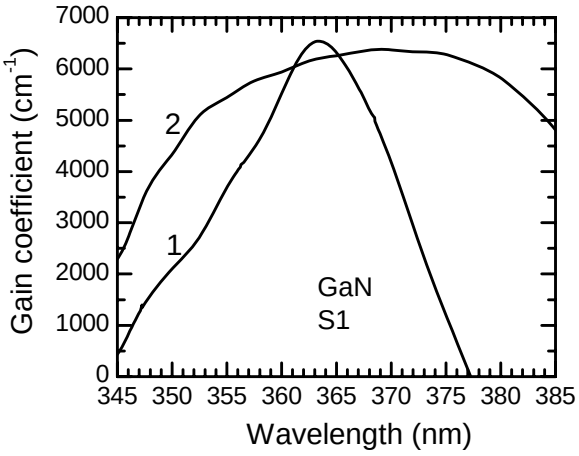

Fig. 3.20. Gain spectra of GaN epilayer S1. The spectra were extracted from the edge emission spectra by using Eq. (3.6) for two pairs of stripe lengths: 3 and 6 μm (1) and 5 and 10 μm (2). [P6]

Since the optical gain increases with increasing excitation intensity, the edge emission, according to Eq. (1.4) should grow faster than spontaneous emission. The excitation power density dependence of the edge

emission intensity is shown in Fig. 3.21 for two extreme stripe lengths. The stripe length of 1 mm corresponded to a long stripe with its length much bigger than its width (30 μm), while the stripe length of the short stripe (10 μm) was smaller than the stripe width (30 μm). For the long stripe, the edge emission intensity I_{em} depends on the excitation intensity I_{ex} approximately as $I_{em} \propto I_{ex}^3$ within four orders of magnitude. The dependence faster than the square of the excitation intensity is usually considered as an indication of stimulated emission. Note, however, that for the short stripe, the dependence is weaker, $I_{em} \propto I_{ex}^2$, though the stripe length dependence of the edge emission intensity evidences the stimulated origin of this emission. The weaker dependence can be explained by taking into account that the stripe width (30 μm) in this case is longer than the stripe length (10 μm). Thus, the carrier density and, consequently, the emission intensity are governed mainly by the light propagating not perpendicular but rather along the sample edge. This light is effectively amplified and might cause the population depletion with increasing excitation intensity. As a result, the pump power dependence of the intensity of

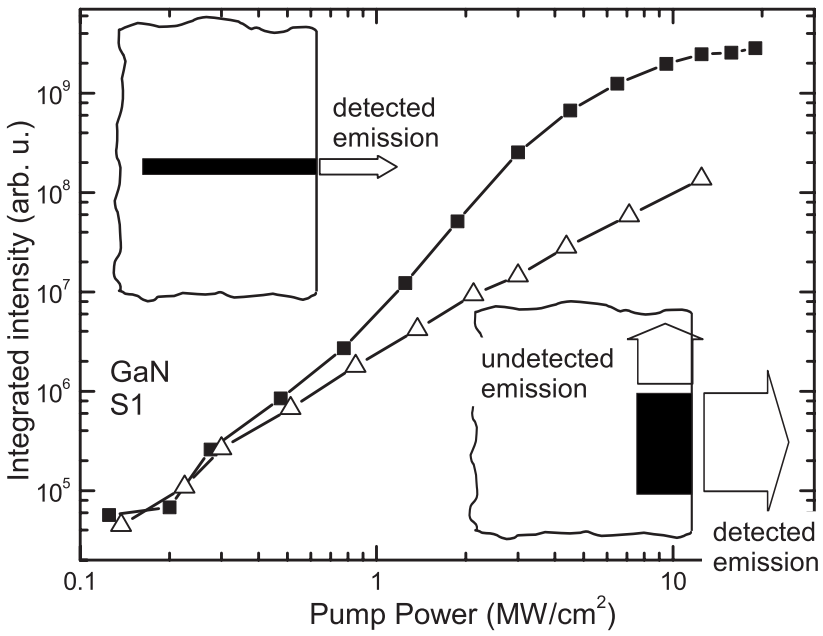

Fig. 3.21. Excitation power density dependence of stimulated emission intensity of sample S1 for 1 mm (squares) and 10 μm stripe lengths (stripe width is 30 μm). In the insets: configurations of "long" and "short" stripes corresponding to the upper and lower curves, respectively (only one propagation direction is highlighted). [P6]

the light propagating perpendicular to the sample edge for short stripe length is weaker than that for the long stripe. Thus, this peculiarity has to be taken into account in VSL experiments and in structures with limited length of the active region, e.g. in vertical cavity surface emitting laser (VCSEL) structures.

Since our samples exhibited strong stimulated emission at the stripe lengths of ~10 μm, which correspond to the epilayer thickness of the sample, we also performed gain experiments in configuration corresponding to the VCSEL configuration [see Fig. 3.22(b)]. In this configuration, the excitation was focused on the sample edge and its length was limited by the thickness of the epilayer (~11 μm for the sample S1). The VCSEL configuration for GaN has a particular advantage over the usual configuration in view of polarization of the emitted light.

In GaN epilayers, the dominant band edge emission is polarized mainly perpendicular to the direction of the crystal axis **c** ($E \perp c$) [26,27,136]. Thus, propagation conditions are different in two excitation configurations used in our experiments (see Fig. 3.22). In the configuration with excitation stripe on the edge of the sample [Fig. 3.22(b)], the light propagation direction is parallel to the **c** axis, and all the photons emitted can propagate along the excited stripe. Meanwhile in the usual configuration [Fig. 3.22(a)], the light travels perpendicular to the **c** axis. Thus, a part of the emitted photons has polarization in parallel with the excitation stripe and cannot propagate along the stripe.

At the lowest excitation intensities, the spectrum of emission propagating perpendicular to the sample surface consists of one band with its peak at 363 nm. This band corresponds to spontaneous band-to-band transitions. The

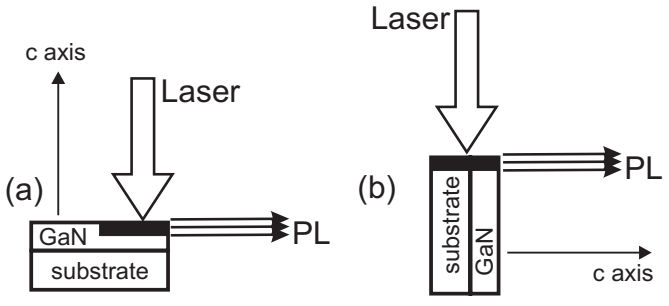

Fig. 3.22. Two modifications of the VSL configuration used in experiments: the usual configuration with the photoexcited stripe on the layer surface (a) and the VCSEL configuration with the photoexcited stripe on the edge of the layer (b).

appearance of the spontaneous emission in this configuration is most probably caused by its scattering due to roughness of the sample edge. As the excitation power density is increased above ~1 MW/cm^2, a new band appears on the long wavelength side. Several spectra of this band after subtraction of the spontaneous emission background are shown in the Fig. 3.23. The band redshifts with increasing excitation power density. This shift could be explained by the band gap renormalization due to many-body interactions in the electron-hole plasma, which increases with increasing excitation intensity.

The stimulated emission band itself consists of several peaks with the distance between them equal to approximately 2.1 nm. This value is consistent with the spacing between Fabry-Perot resonance peaks estimated from the relation $\Delta\lambda = \lambda^2/2nL$ to be 2.3 nm for the cavity length $L = 11$ μm and refraction index $n = 2.6$, which is typical for GaN in this spectral region.

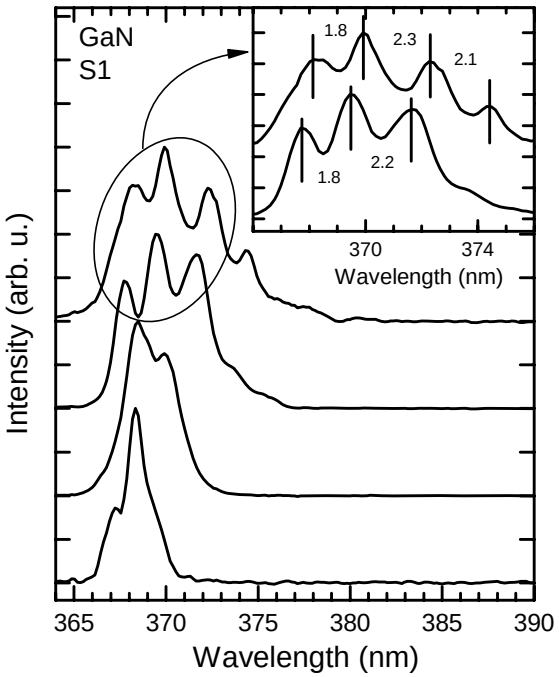

Fig. 3.23. Spectra of sample S1 emission propagating perpendicular to the layer surface when the stripe of excitation light is focused on the sample edge [see Fig. 3.22(b)]. The background due to spontaneous emission is subtracted. The spectra have been shifted along the vertical axis for clarity. The inset shows the expanded section of the two topmost spectra, indicating the distances between peaks. [After P6]

The gain in this configuration can be roughly estimated by using the threshold gain value for the light amplification during the roundtrip within the cavity, which is made of the epilayer surface and epilayer/substrate interface. By using the reflection coefficient of $R_1 = 21\%$ and $R_2 = 4\%$ for GaN/air and GaN/sapphire interfaces, respectively, the threshold gain, $g_{thr} = (2L)^{-1}\ln(R_1R_2)^{-1}$, equals 2200 cm^{-1} for the epilayer thickness of 11 μm. This value

means that the gain for light propagating perpendicular to the layer surface is equal to ~2200 cm^{-1} at excitation power density of 1 MW/cm^2 (excitation at which the stimulated band appears). This gain coefficient value is smaller than that for the light propagating along the sample surface (~7300 cm^{-1}). However, assuming a logarithmic increase of the gain with the excitation intensity [85], values up to ~7000 cm^{-1} may be expected at higher excitations reached in our experiments (~9 MW/cm^2, just below the damage threshold). In that case, the gain coefficient values would be comparable both for light propagating along and perpendicular to the **c** axis.

The influence of gain saturation imposes limitations for application of the VSL technique to study the optical gain in highly-excited GaN. However, despite the problems in determining the peak gain values, the technique might still be a useful tool for comparing GaN epilayers to be employed as active medium in laser diodes. An example of such comparison is presented in Fig. 3.19. The gain was compared in two GaN samples with different dislocation densities and exhibiting different carrier lifetimes. The dislocation densities determined for samples S1 and S2 using the etch pit technique were 10^8 and 4×10^9 cm^{-2}, respectively. The lifetime of nonequilibrium carriers in these GaN epilayers was estimated from the LITG experiments (see section 3.2.1 for more details). The estimated carrier lifetime values for samples S1 and S2 were 2 ns and 960 ps, respectively.

The edge emission dependence on the stripe length for both GaN samples is shown in Fig. 3.19. Two fitting procedures were used for analyzing the dependences and extracting the gain value: using Eq. (1.4) (solid lines in Fig. 3.19) and using Eq. (3.5), which takes into account gain saturation [86] (dashed lines in Fig. 3.19). The gain values for samples S1 and S2 extracted using Eq. (1.4) were 7300 and 3600 cm^{-1}, respectively. The corresponding values extracted using Eq. (3.5) were 7500 and 4000 cm^{-1}. The values obtained by these two fitting methods are consistent and show almost the same ratio of optical gain coefficients between the two samples under study. Furthermore, the gain values correlate with the carrier lifetimes in the epilayers, with the

ratio of lifetimes (~2) being close to the ratio of the gain coefficients (~1.9) in the two samples with different dislocation densities. The dislocations increase the density of nonradiative recombination centers and thus lower the carrier lifetime and, consequently, the carrier density. Moreover, the dislocations might impose the additional optical loss. These results demonstrate the applicability of the VSL technique for comparison of peak values of optical gain in different GaN samples, provided that the measurements are carried out in identical conditions.

To summarize, gain values as high as ~7500 cm^{-1} have been observed in high-quality MEMOCVD^{TM}-grown GaN epilayers with low dislocation density and long carrier lifetimes. This value has been extracted for light propagating perpendicular to the **c** axis of GaN epilayers. Similar gain values were estimated also for the light propagating in parallel with the **c** axis. Gain saturation limits the applicability of the VSL technique for studies of higher gains, which can be achieved by increasing excitation power density or by further improvement of the epilayer quality. However, the VSL technique is useful for comparison of different GaN samples.

3.4. Short summary

1. The correlation between the carrier lifetime and intensity of the defect-related luminescence bands (YL and BL) implies that structural defects bound into complexes with impurities might be responsible for both the radiative recombination resulting in YL and for the nonradiative recombination limiting the carrier lifetime.
2. The comparison of TRPL and LITG results provides a new insight into the interpretation of the room temperature PL decay: fitting of the decay by two exponents corresponding to the carrier lifetime and to one-half of it is suggested as means to extract the carrier lifetime from the TRPL measurements.

3. The simultaneous determination of the carrier lifetime and of the diffusion coefficient showed that, in the GaN samples with similar dislocation densities, higher carrier mobility shortens the carrier lifetime, since the carriers reach the dislocations faster.
4. The FDLM technique enabled us to study the carrier dynamics at an extremely low excitation power density (~0.5 mW/cm^2) and to reveal the competition between recombination mechanisms responsible for YL in GaN at nonequilibrium carrier densities below the saturation of the energy levels involved.
5. High optical gain coefficient values up to ~7500 cm^{-1} have been observed in high-quality GaN epilayers both for light propagating perpendicular and parallel to the **c** axis. Gain saturation limits the applicability of the VSL technique for studies of very high gains, however, the VSL technique is useful for comparison of different GaN samples.
6. MEMOCVD^{TM} growth technique enabled the growth of high-quality GaN epilayers with dislocation densities as low as 10^8 cm^{-2}, exhibiting carrier lifetimes at room temperature up to 2 ns, and optical gain values as high as ~7500 cm^{-1}.

4. Carrier dynamics in AlGaN epilayers

The AlGaN compounds, obtained by the alloying GaN and AlN, are essential for the development of deep UV optoelectronic devices. The AlGaN layers are the basic component of any UV device structure. The alloy mixing, however, introduces an additional factor determining the carrier dynamics, which becomes Al-content-dependent. The growth of AlGaN layers is also more complicated compared to GaN, especially for high aluminum content layers, and results in poorer quality of the layers.

In this chapter, the original results on the investigation of carrier dynamics in AlGaN epilayers will be presented. The carrier lifetime dependence on aluminum content is studied in section 4.1. In section 4.2, the band potential fluctuations profile is compared in two AlGaN epilayers with the same amount of aluminum, but grown by different growth techniques. The chapter ends with the short summary.

4.1. Lifetime of nonequilibrium carriers in high-Al-content AlGaN epilayers

In this section, we compare the optical properties of AlGaN epilayers with different Al content in terms of lifetimes of photogenerated nonequilibrium carriers and PL intensity.

AlGaN epilayers under study were grown and provided by Sensor Electronic Technology, Inc. All the AlGaN epilayers were deposited on basal plane sapphire using low pressure metalorganic chemical vapor deposition and by MEMOCVD^{TM} [16-18] techniques. Trimethyl aluminum, triethyl gallium, and ammonia were used as precursors for Al, Ga, and N, respectively. In set A samples, an initial low temperature AlN buffer (~200 Å) followed by ~2.5 μm thick AlGaN layers with aluminum content of 17%, 26%, 33%, 43%, and 50% for samples from A1 to A5, respectively, was grown using conventional

MOCVD method. In set B samples, 0.1 μm thick AlN buffer layer was first grown using MEMOCVD^{TM} followed by defect filtering AlN/AlGaN superlattice [13,138]. Then, 2.5 μm thick AlGaN layers with aluminum composition of 26% (B1) and 65% (B2) were grown using conventional MOCVD.

All the measurements have been carried out at room temperature. The PL spectra were measured under quasi-steady-state excitation by the 5th harmonic (5.82 eV) of the Q-switched Nd:YAG laser (pulse duration 4 ns). The details of the PL setup are described in section 2.1. The carrier lifetimes were estimated using the LITG technique [125], described in more detail in section 2.3. The grating was created by two overlapping beams of the 4th harmonic (4.66 eV) and probed by tunably delayed pulses of the 2nd harmonic (2.33 eV) of the mode-locked Nd:YAG laser (pulse duration 25 ps).

The diffraction efficiency decay for several AlGaN samples with different aluminum content is shown in Fig. 4.1. The solid lines in Fig. 4.1 demonstrate a good approximation of the decay by an exponential function, and therefore, we suppose that it is caused only by carrier diffusion and recombination. According to Eq. (2.5), grating decay kinetics, measured at several different grating spacings, enable estimation of both the carrier lifetime and diffusion coefficient of the sample. However, for the set A samples, the grating decay times were too short to observe any sufficient effect of diffusion when varying the grating spacing. At a large enough grating spacing Λ, diffusion can be neglected, and the decay time τ_G provides a good

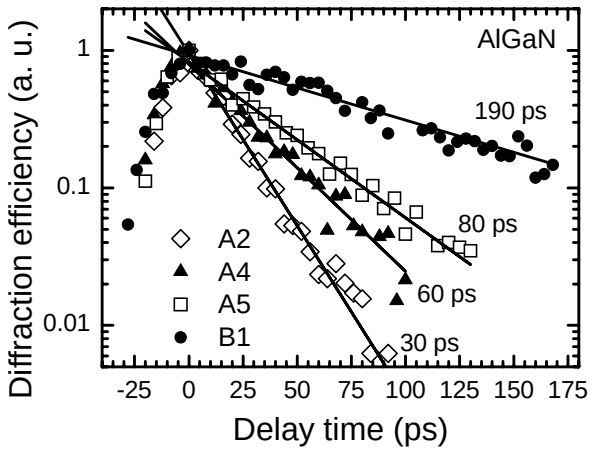

Fig. 4.1. Light induced transient grating decay kinetics in AlGaN samples with different Al content (points) and the best fit to experimental points (lines). Corresponding carrier lifetimes are indicated. [P2]

estimate for the carrier lifetime τ_R, which is indicated near the corresponding grating decay curves in Fig. 4.1.

The induced grating decay time was long enough to observe the effect of diffusion for the sample B1, and the grating decay time changed when the grating spacing was varied. The dependence of grating decay time on grating spacing is shown in Fig. 4.2. The best fit using Eq. (2.5) is also shown there. From the fit, both the diffusion coefficient and carrier lifetime were estimated for the sample B1 (see Fig. 4.2). Since the sample was highly doped *n*-type, the photoexcited holes are minority carriers, and the ambipolar diffusion coefficient, D_a, should be equal to the hole diffusion coefficient, D_p. Simultaneous determination of lifetime and diffusion coefficient enables an estimation of the diffusion length, $L_D = \sqrt{D\tau_R}$. For the measured values of $D = 1.1\pm0.3$ cm^{2}s^{-1} and $\tau_R = 196\pm4$ ps, the diffusion length equals 0.15 ± 0.03 μm. This L_D value was considerably larger than 7.5 nm reported for $Al_{0.27}Ga_{0.73}N$ by another research group [138].

The obtained value of $L_D = 0.15$ μm is close to the average distance between two first-neighbor dislocations, $r_{dd} = 0.13$ μm, which was roughly estimated using a simple relation $N_{dd} = \frac{1}{\pi r_{dd}^2}$ for the dislocation density of 2×10^9 cm^{-2} obtained by the etch pit technique. Thus, it is reasonable to assume that the carrier diffusion and lifetime are dislocation-limited in our AlGaN samples. Such dislocation-limited minority-carrier lifetime has been previously observed in GaP [139]. This mechanism was shown to be an important

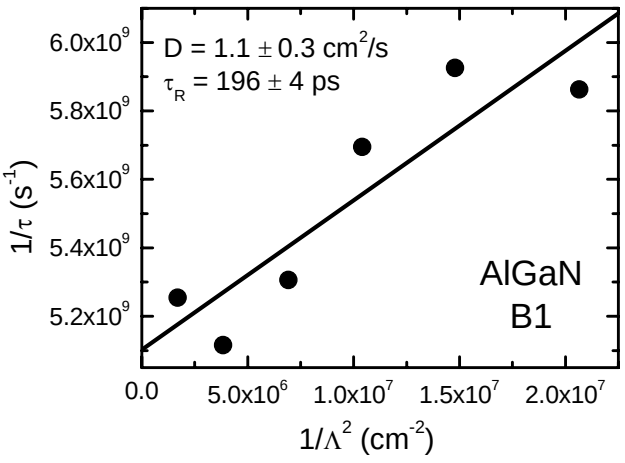

Fig. 4.2. Light induced transient grating decay time versus grating spacing measured in the AlGaN sample B1. The solid line shows the best fit using Eq. (2.5). The estimated diffusion coefficient and carrier lifetime are indicated. [P2]

factor limiting the carrier lifetimes in GaN [140-142] and AlGaN [143]. A quantitative comparison of experimentally obtained lifetime with the dislocation-limited lifetime model of Ref. [139], τ_{scat}, is impeded by a lack of reliable data on effective dislocation radius (i.e. of the radius of the area around the dislocation, where effective carrier recombination occurs). However, the general proportionality $\tau_{scat} \propto N_{dd}^{-1}$ is consistent with our results. In particular, the lifetime in the sample B1 is 196 ps, while the lifetime in the sample A2, which contains the same amount of aluminum, equals 30 ps, i.e. is smaller by a factor of 6.5. The ratio of dislocation density for these two samples is 5. Taken into account that the effective dislocation radius might be comparable with the distance between dislocations in the sample A2 with higher dislocation density of 10^{10} cm^{-2}, the agreement between these two ratios can be treated as satisfactory. Thus, our results imply that nonradiative recombination at dislocations is the dominant mechanism limiting the carrier lifetime in AlGaN samples under study. This conclusion is in agreement with results obtained in AlGaN layers by spatially-resolved techniques showing that screw dislocations act as nonradiative recombination centers [143,144].

The PL spectra of AlGaN samples with different Al content, measured under identical experimental conditions, are presented in Fig. 4.3. The lifetimes estimated by the LITG technique are also indicated there (except for the sample B2, with its bandgap being too large for our LITG experiments). Samples B1 and A2 contain the same amount of aluminum, but B1 is grown on low-defect AlN/AlGaN superlattice buffer acting as a filter, which decreases the dislocation density down to 2×10^{9} cm^{-2} (from 10^{10} cm^{-2} for A2). The decreased dislocation density results in the increase of PL intensity by a factor of 6, which is very close to the ratio of the lifetimes in the two samples (6.5) determined by using LITG technique. This is reasonable, since the radiative emission proceeds at a constant and much lower rate than that of the nonradiative recombination, which limits the lifetime.

The PL intensity decreases with increasing aluminum content in the AlGaN epilayers with similar carrier lifetimes (compare samples A1, A3, A4, and A5).

Since the carrier lifetime in AlGaN epilayers is limited by nonradiative recombination, it is reasonable to assume that the decrease of PL intensity with an increase of the Al content at constant lifetime is caused by a decreased rate of radiative recombination. Such decrease is consistent with the results of the rate calculation of the free carrier and exciton recombination in AlGaN [145]. However, the experimentally observed decrease of PL proceeds faster than could be expected from the calculated radiative recombination rates. This discrepancy can be explained by the change of luminescence polarization with respect to **c** axis from $E \perp c$ to $E \| c$ when aluminum content in AlGaN increases, which inhibits escape of emission from the layer surface of high-aluminum-content-samples [27].

To summarize, the PL, LITG, and etch pit results for AlGaN layers with different Al content show that the lifetime of nonequilibrium carriers in these epilayers is primarily limited by the carrier diffusion to the dislocations, where the nonradiative recombination occurs. The radiative recombination proceeds at the same rate in AlGaN samples with the same Al content (but different dislocation densities) and decreases with increasing Al content. The

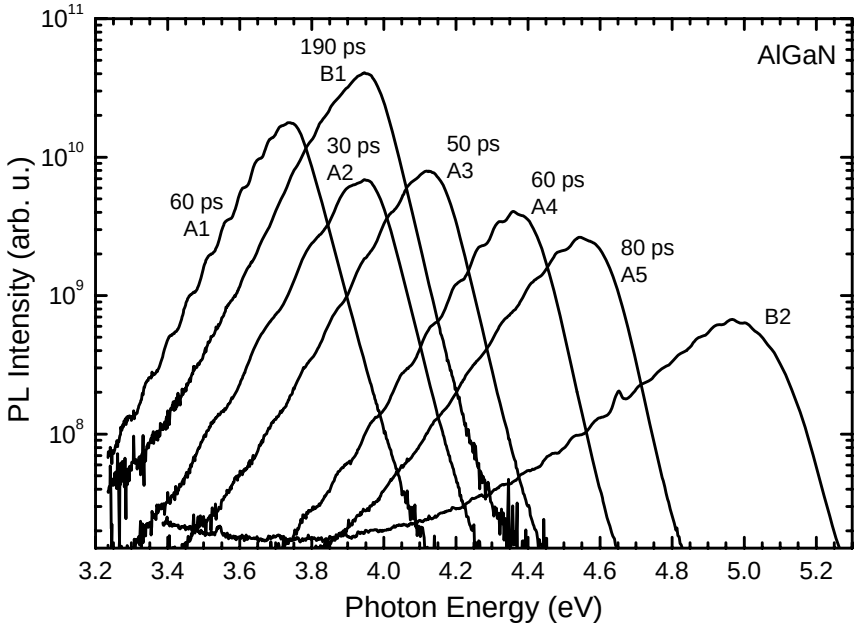

Fig. 4.3. Photoluminescence spectra of AlGaN epilayers with different Al content at room temperature. The carrier lifetimes and sample numbers are indicated. Aluminum content is 17, 26, 33, 43, and 50% for samples A1 to A5; 26 and 65% for samples B1 and B2. [P2]

MEMOCVD^{TM} growth technique enabled an increase of the PL intensity for the AlGaN epilayers grown on sapphire substrates by at least up to a factor of 6, compared to the epilayers grown by conventional MOCVD.

4.2. Exciton hopping and nonradiative decay in AlGaN epilayers

Statistical fluctuations in the composition of a random alloy lead to potential fluctuations capable of spatially localizing excitons. Even though the theoretical estimations predict no phase separation for AlGaN alloys [108,109], compositional fluctuations and Al segregation, in particular around the dislocations [110], have been directly evidenced by transmission electron microscopy and spatially resolved cathodoluminescence [110,111].

In this section, the band potential fluctuations profile in AlGaN is compared for two AlGaN epilayers with the same amount of aluminum, but grown by different growth techniques.

The AlGaN epilayers under study were from the same set of samples investigated in section 4.1. Two AlGaN epilayers with a similar amount of aluminum (~26%) grown by using different techniques, conventional MOCVD (sample A2) and MEMOCVD^{TM} (sample B1), were selected. More details on sample growth are given in section 4.1.

The temperature evolution of the PL bands of AlGaN epilayers in the range of 10-300 K was studied at a low excitation power density (10 kW/cm^2) using the 5th harmonic (5.82 eV) of a Q-switched Nd:YAG laser (pulse duration 4 ns). The details of the PL setup are described in section 2.1.

The carrier dynamics in AlGaN epilayers was investigated at room temperature by TRPL and LITG techniques, described in sections 2.2 and 2.3, respectively. The 5th harmonic (5.82 eV) of the mode-locked Nd:YAG laser (pulse duration 25 ps) was used for excitation in TRPL measurements. In LITG experiments, the 4th harmonic (4.66 eV) of the same mode-locked Nd:YAG laser was used for excitation, and the 2nd harmonic (2.33 eV) for probe.

As was already shown in section 4.1, the grating decay transients of samples A2 and B1 could be well approximated by single-exponential functions. Since the grating spacing Λ was large enough to neglect diffusion in Eq. (2.5), the carrier lifetimes were directly estimated. The grating decay curves and solid line approximations are repeated for clarity in Fig. 4.4 for the samples A2 and B1 only. The estimated carrier lifetimes were 30 and 190 ps in samples A2 and B1, respectively.

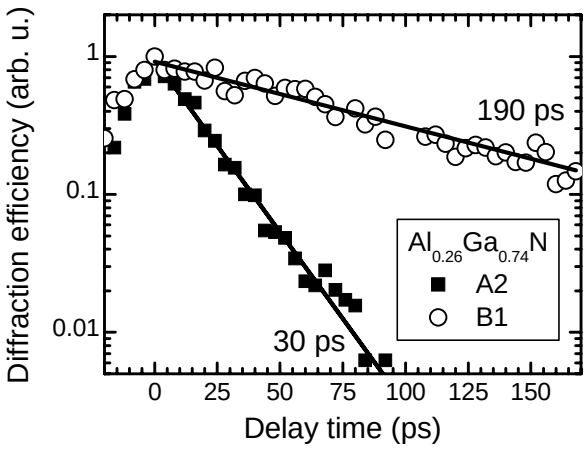

Fig. 4.4. LITG decay transients for $Al_{0.26}Ga_{0.74}N$ epilayers grown on MOCVD (sample A2) and MEMOCVD (sample B1) buffer layers. Solid lines are the best fit by single-exponential functions. The estimated carrier lifetimes are indicated. [P3]

The difference in carrier dynamics in the two AlGaN epilayers under study was also observed in PL intensity decay kinetics shown in Fig. 4.5. Similar to LITG decay kinetics, the PL decayed faster for the sample A2. However, the measured PL kinetics for both samples were nonexponential (see Fig. 4.5). The initial fast decay might be strongly affected by finite excitation pulse duration (20 ps), and possibly, by many-body effects due to the high carrier density. Surface recombination and diffusion of carriers to the sample depth might also have some effect on the decay curves [101,106], however in this case, the carrier lifetime and epilayer thickness are too small for the diffusion to have any considerable effect. However, even the further decay after the faster initial decay proceeds nonexponentially, making the extraction of carrier lifetimes from TRPL results quite uncertain [131,132]. Assuming the equal densities of nonequilibrium electrons and holes, the nonequilibrium carrier density is expected to decay exponentially with the lifetime τ. Consequently, the luminescence intensity for band-to-band transitions $I_{LUM}(t)$ should decrease

with a characteristic decay time $\tau/2$ asymptotically transforming to τ, as Δn approaches equilibrium carrier density, n_0:

$$I_{LUM}(t) \propto \Delta n(t)\left[\Delta n(t) + n_0\right] \propto A\exp\left(-\frac{t}{\tau/2}\right) + B\exp\left(-\frac{t}{\tau}\right). \qquad (4.1)$$

Here, A and B are freely adjustable parameters. See section 3.2.1 for more details.

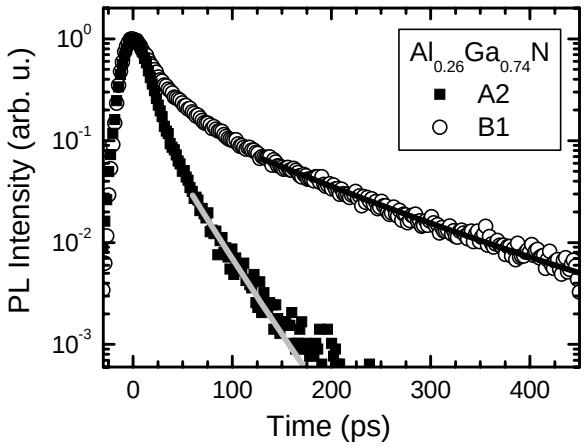

Fig. 4.5. PL decay transients for $Al_{0.26}Ga_{0.74}N$ epilayers grown on MOCVD (sample A2) and MEMOCVD (sample B1) buffer layers. Lines indicate two-exponential fits according to Eq. (4.1). [P3]

To evade the uncertainty in the extraction of carrier lifetimes from the TRPL experiments, the two-exponential PL decay fit was performed by substituting τ by τ_R extracted from LITG data. The fit is shown by solid lines in Fig. 4.5. This self-consistent fit of TRPL and LITG decay was fairly good and confirmed the estimation of the carrier lifetimes of 30 and 190 ps in samples A2 and B1, respectively.

The large difference in room-temperature carrier lifetimes might be caused by differences in the densities of nonradiative recombination sites or in the amplitude of the potential fluctuations, which prevent carriers from reaching those recombination sites. To distinguish between these two effects, we employed the Monte Carlo simulation of exciton hopping to describe the temperature dynamics of the PL spectra measured at low excitation.

The temperature dynamics of the PL spectrum is demonstrated in Fig. 4.6 for both samples. The spectra for the MOCVD-grown sample A2 are dominated by the band at ~4.0 eV, attributed to band-to-band transition in AlGaN epilayers, and additional smaller peaks at the lower energy side, distanced ~100 and ~200 meV from the main peak and attributed to the phonon replicas of the main band. In the MEMOCVD^{TM}-grown sample B1 spectra, the

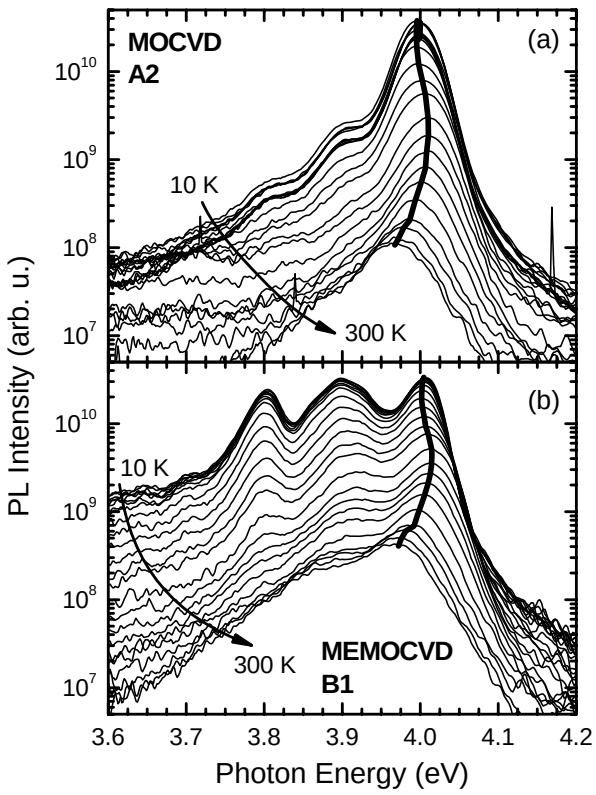

Fig. 4.6. PL spectra of AlGaN epilayers A2 (a) and B1 (b) as a function of temperature. Solid lines indicate the peaks of the PL spectra and serve as a guide for the eye. [After P7]

phonon-replica-bands become very strong and are of similar intensity as the main peak. This fact already indicates a higher quality of MEMOCVD^{TM}-grown sample.

The peak positions of the main band are highlighted by solid line in Fig. 4.6. The peaks exhibit a well-established S-shaped temperature behavior [113-118]. For clarity, temperature behavior of the PL peak position for both samples is shown in a separate figure (see Fig. 4.7). Both peaks slightly redshift in the range from 10 to 60 K, then blueshift in the range from 60 up to 140 K, and redshift again at higher temperatures. The slight difference in the absolute value of peak positions (~15 meV) can be attributed to the slight difference in the Al content or its distribution in the epilayers or strain difference in samples grown by different techniques. The temperature dependence of the PL band FWHM is shown by points in Fig. 4.8. The FWHM dependence is W-shaped with the characteristic kink at ~100 K. Such nonmonotonous temperature behavior of the PL band parameters have been previously observed in InGaN [146], AlInGaN [147], and AlGaN [113,114,148] alloys and are known to indicate phonon-assisted exciton "hop-like" motion through the randomly distributed localized states.

To quantitatively describe the W-shaped temperature dependences of the PL linewidth in AlGaN epilayers under study, we performed Monte Carlo simulation of localized exciton hopping (see Ref. 147 for details). Since the

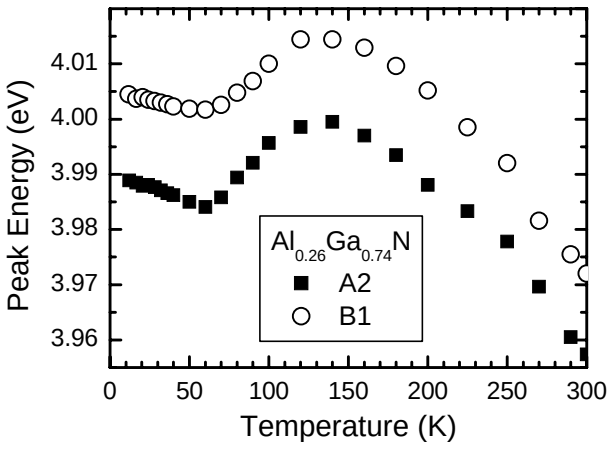

Fig. 4.7. Temperature dependences of the peak position of the PL band in two $Al_{0.26}Ga_{0.74}N$ epilayers grown on MOCVD (sample A2) and MEMOCVD (sample B1) buffer layers. [C3]

epilayer thickness was ~2.5 μm, the simulation was performed in three dimensions. The localized states were considered to have a Gaussian-like density of states with a standard deviation σ, whereas their spatial 3D-distribution was assumed to be completely random. The rate of the exciton hopping from a localized state i to a state j separated by the distance R_{ij} was described by Miller-Abrahams expression,

$$\nu_{ij} = \nu_0 \exp\left\{-\frac{2R_{ij}}{\alpha} - \frac{E_j - E_i + \left|E_j - E_i\right|}{2kT}\right\}, \qquad (4.2)$$

where E_i and E_j are the energies of the ith and jth states, respectively, α is the decay length of the exciton wave function, and ν_0 is the attempt-to-escape frequency. The exciton in any localized state could either hop to another state or annihilate by emitting a photon. One of these two events was selected randomly by taking into account the rate of the radiative recombination as well as all the possible hopping rates described by Eq. (4.2). The energies of the localized states at which the exciton recombined were recorded to compile the emission spectrum.

The simulation was performed for two spatial distributions of the potential fluctuations profile: single scale and double scale. The single-scale simulations qualitatively reproduced the experimental W-shaped dependence of the bandwidth (except for the temperature range above 200 K, where the increase of the bandwidth is caused by the extended states, which are not described by this model). However, the single-scaled potential fluctuation profile model was insufficient for a quantitative fit of the simulation and experimental results.

The simulated FWHM appeared to be considerably narrower than the measured values. The quantitative description (solid lines in Fig. 4.8) of FWHM dependences was achieved only by introducing a double-scaled potential profile model, which is schematically illustrated in the inset of Fig. 4.8. This model assumes exciton hopping through the potential fluctuations (on the scale σ) in the individual, possibly Al-poor, regions with different average Al content resulting in dispersion of the average exciton energy (on the scale Γ). A similar model (based on In-rich regions) was succesfully applied for III-N alloys containing indium (InGaN and AlInGaN) [146,147]. A rapid increase of the PL linewidth up to 100 K and subsequent saturation above this temperature indicates a thermal population of the higher-energy localized states and exciton thermalization over the localized states, respectively. A further increase above 200 K is caused by the influence of extended states, which are not taken into account in the model. The scales of potential fluctuations, as yielded by the double-scaled potential profile model, were found to be quite similar in both $Al_{0.26}Ga_{0.74}N$ epilayers: $\sigma = 19$ meV, $\Gamma = 20$ meV in A2 and $\sigma = 18$ meV, $\Gamma = 18.5$ meV in B1. Note that the fluctuation scales are lower than the thermal energy at room temperature. This justifies the dominance of free carrier

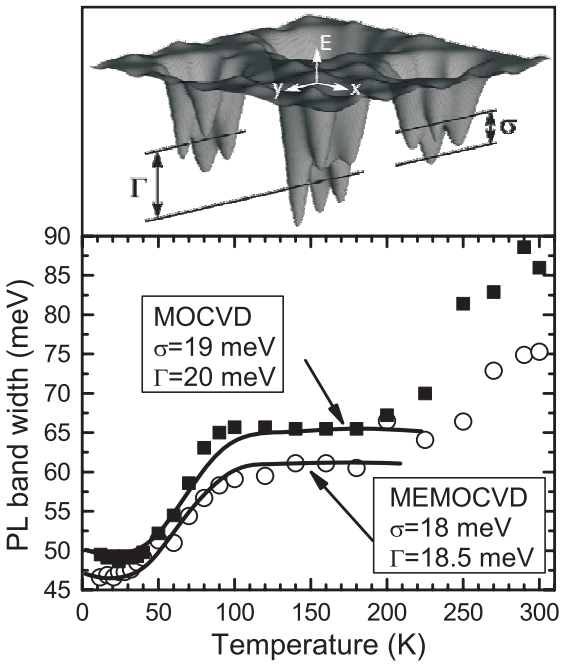

Fig. 4.8. Temperature dependences of the PL linewidth in $Al_{0.26}Ga_{0.74}N$ epilayers grown on MOCVD (A2, solid points) and MEMOCVD (B1, open points) buffers. Lines show results of Monte Carlo simulation of exciton hopping for different scales of random potential fluctuations σ and Γ (indicated). The inset depicts the sketch of the double-scaled potential profile in AlGaN alloy, where σ indicates dispersion of the localized states within isolated Al-poor regions and Γ indicates dispersion of the average exciton energy in these regions. [P3]

recombination assumed in the interpretation of the room-temperature time-resolved PL and LITG experiments.

The lack of significant difference in band potential fluctuations profile between the two AlGaN epilayers under study indicates that the six-fold difference in carrier lifetimes is caused by a different density of nonradiative recombination centers due to the different growth techniques. As discussed in more detail in section 4.1, the dislocation density was 10^{10} cm^{-2} in sample A2 and $2 \cdot 10^{9}$ cm^{-2} in sample B1, with the ratio of 5 being very close to the ratio in the carrier lifetimes.

To summarize, quantitative description of nonmonotonous temperature dependence of the PL linewidth in AlGaN alloy using Monte Carlo simulation of localized exciton hopping revealed the double-scaled potential fluctuations similar to those found in InGaN and AlInGaN alloys. We found that excitons in AlGaN hop within the random potential fluctuations (on the scale σ) in the isolated low-band-potential regions dispersed in the average localization energy (on the scale Γ). Most likely, these regions have a lower Al content which, possibly, is influenced by dislocations and strain in the AlGaN epilayers. We propose that the six-fold difference in carrier lifetimes estimated in $Al_{0.26}Ga_{0.74}N$ epilayers is caused not by potential fluctuations (estimated to be $\sigma \approx \Gamma \approx 19$ meV), but rather by a different density of nonradiative recombination centers due to the different growth techniques used for the deposition of their buffer layers.

4.3. Short summary

1. The PL, LITG, and etch pit results for AlGaN layers with different Al content shows that the carrier lifetime in AlGaN is primarily limited by the carrier diffusion to the dislocations, where the nonradiative recombination occurs. The radiative recombination proceeds at the same rate in AlGaN samples with the same Al content (but different dislocation densities) and decreases with increasing Al content.

2. A quantitative description of PL linewidth in AlGaN alloy was achieved by using Monte Carlo simulations by introduction of double-scaled potential profile model. The excitons hop within the random potential fluctuations (on the scale σ) in the isolated low-band-gap regions dispersed in the average localization energy (on the scale Γ). Most likely, these regions have a lower Al content.
3. Both potential profile scales were found to be similar ($\sigma \approx \Gamma \approx 19$ meV) and independent of the growth technique. A six-fold increase of carrier lifetime in MEMOCVD^{TM}-grown AlGaN epilayer is caused not by potential fluctuations, but by a reduced density of nonradiative recombination centers.
4. The MEMOCVD^{TM} growth technique enabled an increase of the PL intensity (by a factor of 6) and of carrier lifetime (by a factor of 6.5) for the AlGaN epilayers grown on sapphire substrates, compared to the epilayers grown by conventional MOCVD.

5. Carrier dynamics in AlGaN/AlGaN multiple quantum wells

The AlGaN/AlGaN multiple quantum well (MQWs) structures are the next step towards the deep UV devices. To improve the performance of AlGaN-heterostructures-based devices, the processes determining the device operation have to be analyzed and understood. As compared to the epilayers, in quantum well structures the well width strongly affects the carrier dynamics. Moreover, in nitride heterostructures, the built-in electric field due to spontaneous and piezoelectric polarization plays a significant role.

In this chapter, the original results on the investigations of carrier dynamics in AlGaN/AlGaN MQWs will be presented. The well-width dependence of carrier lifetime is studied in section 5.1. In section 5.2, the photoluminescence dynamics in AlGaN MQWs and the influence of built-in electric field and localized states on PL dynamics will be discussed. The chapter ends with the short summary.

5.1. Well-width dependence of carrier lifetime in AlGaN/AlGaN MQWs

In this section, we investigate the carrier dynamics in a set of AlGaN MQWs structures with different well widths.

The AlGaN MQWs structures under study were grown and provided by Sensor Electronic Technology, Inc. The AlGaN MQWs used in this study were grown by metalorganic chemical vapor deposition on a sapphire substrate with a 1.2-μm-thick buffer layer of *n*-AlGaN with 55% of aluminum. The quantum well structures consisted of ten periods of $Al_xGa_{1-x}N$ barriers with $x = 0.49$ and wells with $x = 0.35$. The well thicknesses in five different samples ranged from 1.65 nm to 5.0 nm, while the barrier width was constant (11.5 nm).

All the measurements were performed at room temperature. The PL decay kinetics were measured using the setup described in section 2.2 under excitation by the 5th harmonic (5.82 eV) of the mode-locked YAG:Nd laser (pulse duration 25 ps). The carrier lifetimes were estimated using the LITG technique [125], described in more detail in section 2.3. The grating was created by two overlapping beams of the 4th harmonic (4.66 eV) and probed by tunably delayed pulses of the 2nd harmonic (2.33 eV) of the same YAG:Nd laser.

The PL decay kinetics for several MQWs samples with different well thicknesses are shown in Fig. 5.1. The PL spectra of the structures do not change significantly during the decay therefore the spectrally-integrated PL intensity decay is analyzed. The observed PL decay kinetics is strongly nonexponential for all the samples. The slowing down of the PL decay rate can be interpreted by involvement of more localized carriers (excitons) with a lower probability to reach the nonradiative recombination centers and, thus, having longer lifetimes. However, experimental evidence presented below led us to conclude that the nonexponential behavior of the luminescence intensity decay is dominated by two effects: the decay of the carrier density and a decrease of the radiative recombination rate due to the built-in electric field getting unscreened at low carrier concentrations.

At room temperature, the decay of the carrier density is mainly governed by *nonradiative* carrier recombination even in the initial stage of the PL decay. Thus, the carrier density should decrease exponentially with characteristic lifetime determined by nonradiative recombination. However, the rate of *radiative* recombination in AlGaN QWs is influenced by the built-in electric field in the QWs created by spontaneous and piezoelectric polarization. As a consequence, the wells have a tilted bottom [40]. At low carrier densities, electrons and holes are spatially separated in such triangular well, thus the probability of their recombination is decreased. The nonequilibrium carriers screen the field and, consequently, increase the radiative recombination rate. Under intense photoexcitation (as in our experiment), the built-in field is

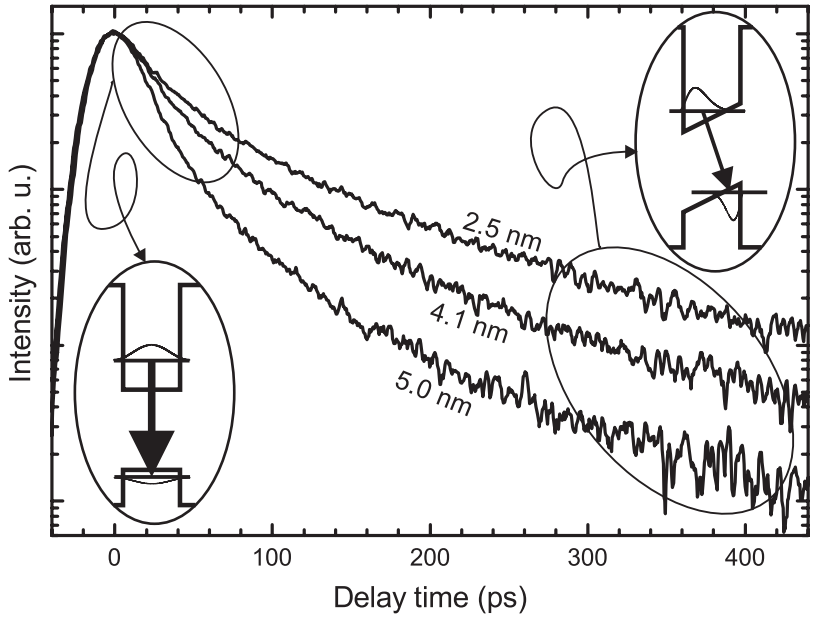

Fig. 5.1. Normalized PL decay kinetics for AlGaN MQWs structures with different well widths (indicated). Measurements were performed under excitation energy density of 25 mJ/cm^2. Insets show two limiting cases of the built-in field screening/recovery processes. They are attributed to corresponding regions on PL decay curves. [After P9]

initially screened, but recovers with decreasing carrier density after the end of the excitation pulse. This causes a decrease in radiative recombination rate and makes the PL intensity decay faster than the decay of the carrier density. However, the radiative recombination rate becomes constant once the QW completely regains its triangular shape. Thereafter, the decay proceeds at a slower and constant rate, as observed experimentally (see Fig. 5.1). The contribution of the initial fast decay increases with the well width, since the electron-hole separation is more pronounced in broader wells. This is clear evidence indicating the influence of the screening-recovery effect on the PL decay. The screening/recovery processes and their effect on PL decay curve are schematically shown in Fig. 5.1.

The range of pump pulse energy density causing an increase in contribution of the fast initial decay (see Fig. 5.2) corresponds to the range of increased rate of PL intensity growth (see inset in Fig. 5.2). This agrees with the interpretation that increasing influence of screening plays a role. The further increase in pump pulse energy density above ~20 mJ/cm^2 does not change the

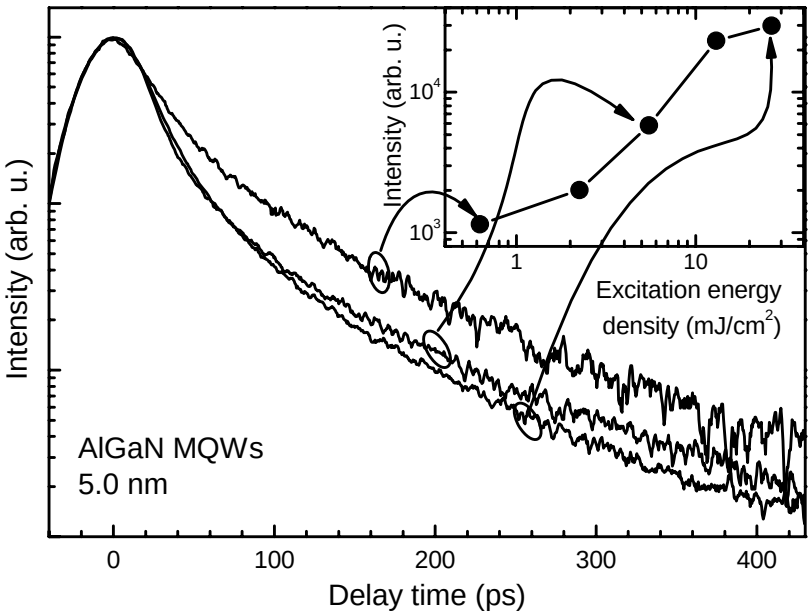

Fig. 5.2. Normalized PL decay kinetics for AlGaN MQWs structure with well width of 5 nm at different excitation energy densities. Inset shows the excitation energy density dependence of the PL intensity at time zero for the same AlGaN MQW structure. [After P9]

decay kinetics and corresponds to a slower rate of growth in PL intensity, since the built-in field is totally screened at such high pump energy densities.

Since the nonexponentiality of PL decay strongly obscures the determination of carrier lifetime from TRPL data, we estimated the carrier lifetime (which is determined by nonradiative recombination, as discussed above) using a more straightforward LITG technique. Figure 5.3 shows the measured decay curves of the induced transient grating efficiencies for several MQW samples with different well widths. The decay of the induced grating efficiency can be approximated by a single exponent (see solid lines in Fig. 5.3) in accordance with Eq. (2.4). The grating decay curves measured at several grating spacings did not show

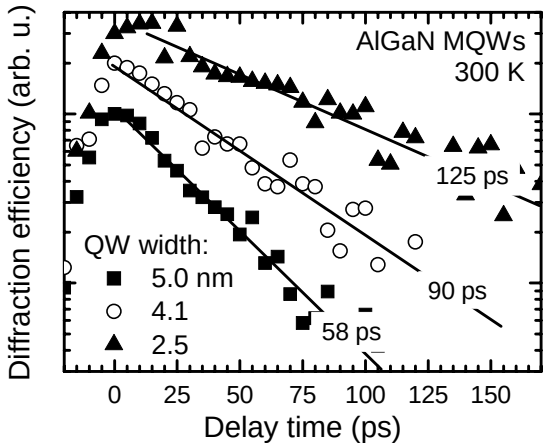

Fig. 5.3. Decay of induced transient grating efficiency for AlGaN MQW structures with different well widths (indicated). The curves were shifted along the vertical axis for clarity. Solid lines show the best fit using a single exponential function. [P9]

any significant difference, and therefore the effect of diffusion was neglected. Thus, the carrier lifetime τ_R was equal to the grating decay time τ_G determined experimentally.

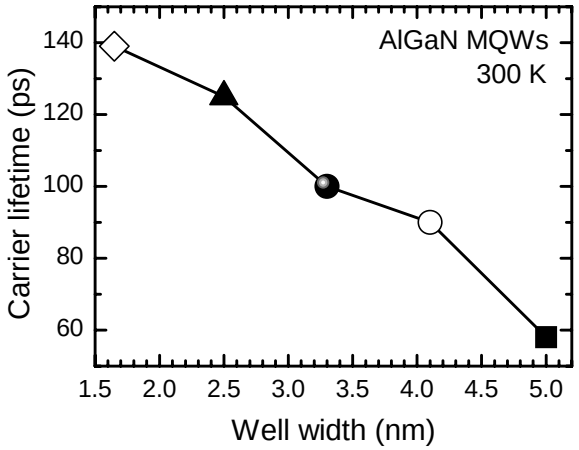

Fig. 5.4. Well-width dependence of carrier lifetimes for AlGaN MQW structures at excitation energy density of 70 μJ/cm^2. [After P9]

The LITG efficiency is proportional to carrier density squared and is not influenced directly by the rate of radiative recombination. This allows us to compare the nonradiative decay rates in QWs with different well widths. The comparison presented in Fig. 5.4 indicates a decrease of the carrier lifetime in broader wells. This result is due to the lifetime being caused primarily by nonradiative carrier recombination. This behavior is in contrast to what is expected when radiative recombination is dominant because of a stronger spatial electron-hole separation in wider QWs (also compare with the previous studies of InGaN/GaN [149,150] or AlGaN/GaN [151] showing an opposite trend). The dependence depicted in Fig. 5.4 can be explained by the carrier localization. It is most probable that in narrow QWs like in our experiments, the localization is mainly caused by well-width fluctuations. The potential fluctuations in the plane of the QW due to the thickness fluctuations are larger in narrower QWs. For example, the difference in the energy of the lowest energy transition in rectangular QWs due to well-width fluctuation by 1 monolayer are 47 and 7 meV for 1.65- and 5-nm-thick QWs, respectively; see Fig. 5.5. The schematic sketch of such localization due to well width fluctuations is shown in the inset in Fig. 5.5. The localization inhibits the carrier migration to nonradiative recombination centers and increases the carrier lifetime. The deeper are the carriers localized, the longer is their lifetime. Thus, the lifetime increases with the decreasing well width.

The decrease of the carrier lifetime in broader QWs can also be influenced by increasing dislocation density, which becomes more pronounced when the

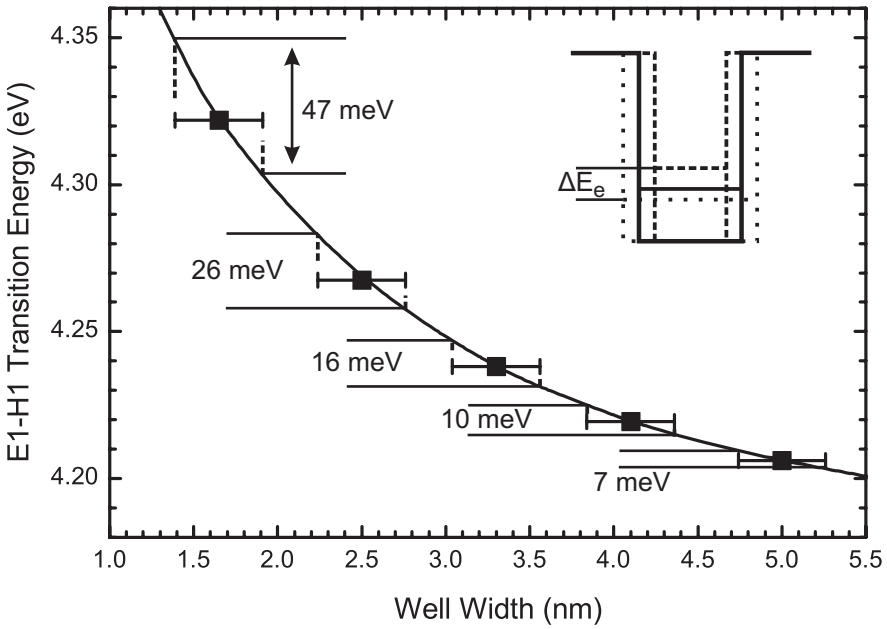

Fig. 5.5. Calculated dependence of optical transition energies in rectangular quantum well on well width. Solid points indicate well widths corresponding to investigated structures; error bars show the possible well width fluctuation by 1 monolayer. The fluctuations in transition energy due to well width fluctuations are indicated. Inset shows a sketch of the QW width fluctuations.

well width approaches the critical thickness. Previously, the increase in density of nonradiative recombination centers due to increasing dislocation density in broader wells was pointed out as an origin of carrier lifetime decrease in AlGaN/GaN QWs. [151].

It is worth noting that the initial carrier density in LITG experiments is considerably lower than that in TRPL experiments. The carrier densities used in LITG experiments correspond to the carrier density in TRPL experiments approximately from 100 to 200 ps after the PL excitation pulse. In this time window, the PL decay slope is consistent with the lifetimes extracted more accurately in the LITG experiments and follows the same trend with increasing the well width.

To summarize, a set of AlGaN/AlGaN MQWs structures with well width varying from 1.65 to 5.0 nm was investigated by TRPL and LITG techniques. The fast component in PL intensity decay is attributed to a decrease of radiative recombination rate due to vanishing screening of the built-in electric field, which recovers with decreasing nonequilibrium carrier density. The

LITG technique enabled us to estimate and compare the carrier lifetimes in the QWs with different well widths. A decrease of carrier lifetime with increasing well width is observed and attributed to differences in potential profile in the plane of the quantum well, which affects the carrier localization, and quantum well quality.

5.2. Effect of built-in electric fields and localized states on photoluminescence dynamics in AlGaN MQWs

In this section, we investigate the influence of built-in electric field and localized states on the photoluminescence dynamics in AlGaN/AlGaN MQWs.

The samples under study were the same as in section 5.1, more details can be found there. The PL dynamics in MQWs structures was investigated under quasi-steady-state conditions using a setup described in section 2.1. The 4th harmonic (4.66 eV) of the Q-switched YAG:Nd laser (pulse duration 4 ns) was used for excitation. The temperature evolution of the PL bands was measured in the range of 8-300 K, whereas the excitation power density was changed by more than three orders of magnitude up to a few MW/cm^2.

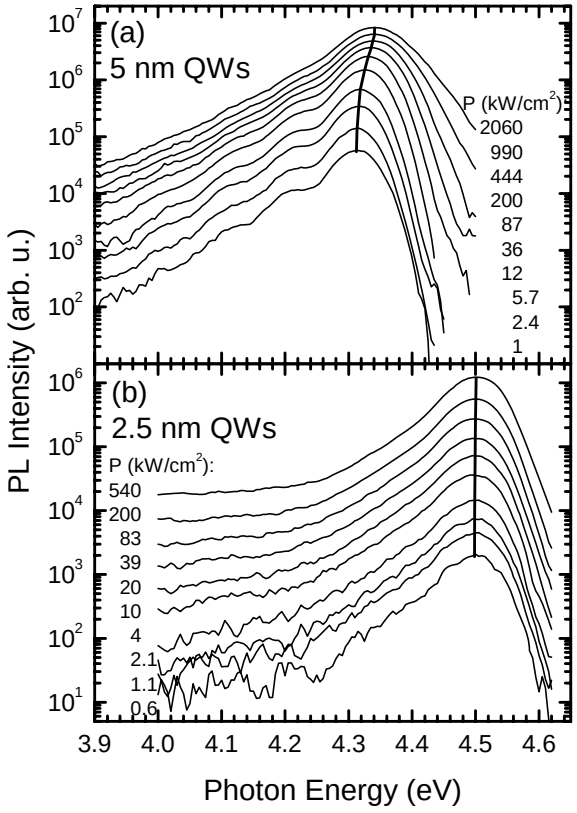

Fig. 5.6. PL spectra of two AlGaN/AlGaN MQWs with well width of 5.0 nm (a) and 2.5 nm (b) at $T = 8$ K under different excitation power densities. PL band peak position is traced by solid lines. [P15]

The PL spectra measured under different excitation power densities at 8 K for two AlGaN/AlGaN MQW samples with the well thickness of 5 nm and 2.5 nm are shown in

Fig. 5.6(a) and (b), respectively. All the PL spectra consist of one broad band. With increasing excitation power density, the PL band peak position considerably shifts to the short-wavelength side in broad QWs but the shift becomes less pronounced in narrower QWs and is negligible in 2.5 nm-wide QWs [see Fig. 5.6(b)].

The PL band peak shift for three different well widths is presented as a function of excitation power density by dots in Fig. 5.7(a) and (b) at 8 K and 300 K, respectively. The blue shift is usually interpreted by two possible processes: i) gradual population of the deepest localized states in the tail of the density of states [152,153], which are formed below the average band gap due to inhomogeneous composition of the ternary compound AlGaN and/or well width fluctuations; ii) screening of the built-in electric field by nonequilibrium carriers and, consequently, shifting the lowest energy states further apart in energy as the QW transforms from triangular towards rectangular shape [41,154]. The absence of the PL band shift in narrow QWs indicates that the second process is predominantly responsible for the shift, since the built-in electric field has less important effect on the energy states for electron and hole in narrower QWs. Moreover, as shown by time-resolved PL study discussed in section 5.1, the carriers are more strongly localized in narrower QWs. Thus, the PL band shift should be even more pronounced in narrower QWs, if caused by filling-in of the localized states. The experiments show the opposite tendency.

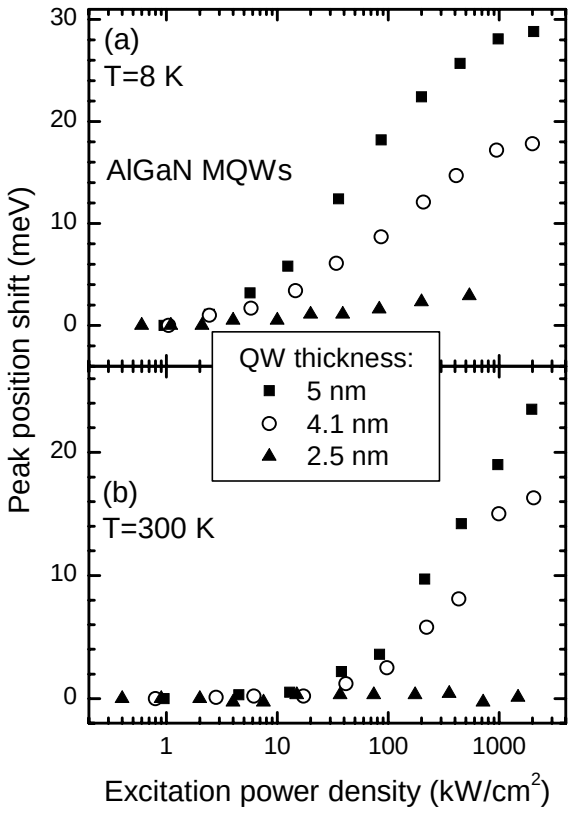

Fig. 5.7. Shift of PL peak position as a function of excitation power density in AlGaN/AlGaN MQWs with well widths of 2.5 nm, 4.1 nm, and 5.0 nm at T = 8 K (a) and T = 300 K (b). [P15]

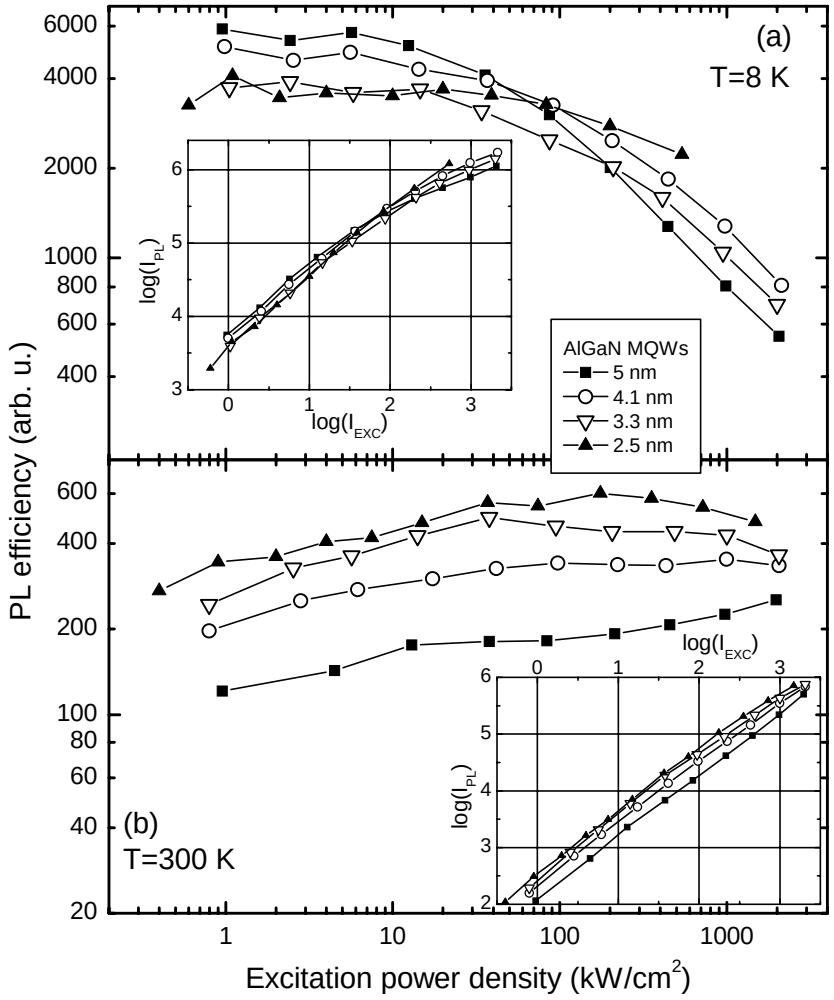

Fig. 5.8. Ratio of PL intensity to excitation power density as a function of excitation power density in AlGaN/AlGaN MQWs at $T = 8$ K (a) and 300 K (b). The insets show corresponding integrated PL intensity dependences on excitation power density. [P15]

We have tried to fit the observed PL band shift with the shift calculated under assumption that it is predominantly caused by the screening of the built-in electric field. This was done by simultaneously solving the stationary Schrödinger equation and the Poisson equation describing the asymmetric space charge distribution in the well. This solution yields the PL band peak position dependence on the carrier density. To fit the calculated band shift as a function of carrier density to the measured band shift dependence on excitation power density, we used the experimental PL intensity dependence on excitation power density [see insets in Fig. 5.8(a) and (b)]. Since both the radiative recombination of localized electron-hole pairs or excitons, which

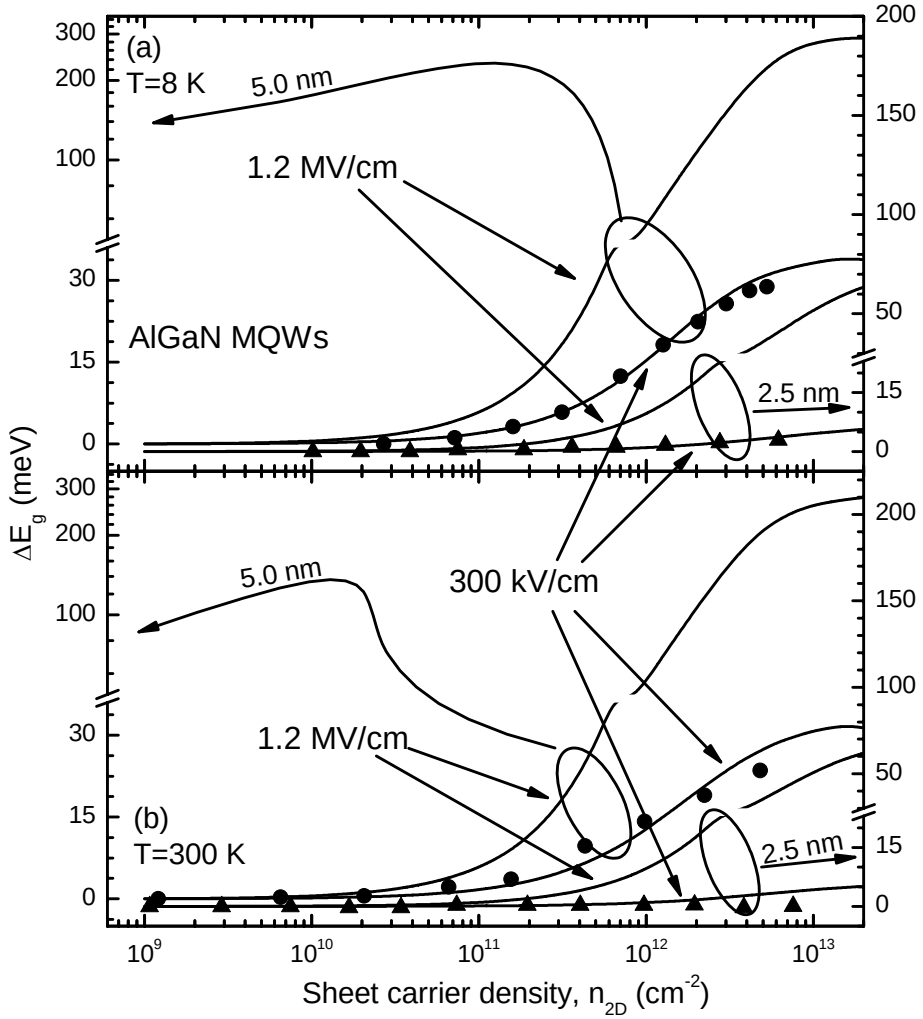

Fig. 5.9. Comparison of experimental PL band peak position dependences on sheet carrier density (dots) and corresponding theoretical curves in AlGaN/AlGaN MQWs at T=8 K (a) and 300 K (b). Well thicknesses are indicated. Theoretical curves were calculated for two field values: 300 kV/cm (the best-fit value) and 1.2 MV/cm (the value obtained from material parameters).

dominates in our QWs, and the nonradiative recombination are linear, we assumed that the PL intensity is directly proportional to the carrier density. The carriers might be localized along the well plane but they are still able to screen the built-in electric field in perpendicular direction, just as the carriers, which are free to move in the well plane. Therefore, all the carriers, either localized or free, contributed to the screening and were accounted for in our calculations. The fitting results are presented by solid lines in Fig. 5.9. All the dependences were calculated by using typical material parameters, listed in Table 5.1, with the built-in electric field being the only adjustable parameter. Since the field depends on the spontaneous polarization at the heterojunction and the

Table 5.1. Material parameters of AlGaN/AlGaN MQW structure, which were used in calculations

Parameter	$Al_{0.55}Ga_{0.45}N$ buffer	$Al_{0.49}Ga_{0.51}N$ barrier	$Al_{0.35}Ga_{0.65}N$ well
a (Å)	3.147	3.151	3.162
E_g (eV)		4.532	4.166
m_e^*/m_0		0.27	0.25
m_{hh}^*/m_0		2.63	2.38
P_{sp} (C/m^2)		-0.054	-0.047
e_{31} (C/m^2)		-0.45	-0.42
e_{33} (C/m^2)		1.09	0.97
C_{13} (GPa)		107	106.7
C_{33} (GPa)		386	389
ε		9.8	10

* All the parameters were taken from ref. [155] for GaN and AlN and linearly interpolated. For E_g, the bowing parameter value $b = 1$ was used.

piezoelectric polarization in the well material, its value was maintained constant in the calculations for all the QWs under study. The value of the built-in electric field corresponding to the best fit was equal to 300 kV/cm. This is a considerably lower value than that obtained for AlGaN/AlGaN structures under study by using the expression for an undistributed field:

$$F_{w\max} = \frac{P_{barr} - P_{well}}{\varepsilon\varepsilon_0}, \tag{5.1}$$

where P_{barr} and P_{well} are the total polarizations, consisting of spontaneous and piezoelectric components, of the barrier and well regions, respectively. The spontaneous polarization is the material constant, while the piezoelectric component is calculated using Eq. (1.3). The material constants used for the field estimation are given in Table 5.1. The calculations according to Eq. (5.1) yield the field value of 1.2 MV/cm. The PL band shift calculated using this field value is also shown by solid lines in Fig. 5.9. A similar difference between best-fit field and the field calculated from material constants has been previously obtained for dynamic PL band shift after short-pulse excitation [42]. A possible contribution of the band-tail-filling effect can only increase the PL band blue-shift with increasing pump power density. Consequently, the band-

tail filling cannot explain why the experimentally observed band shift is smaller than that corresponding to the calculated built-in electric field of 1.2 MV/cm. Moreover, as mentioned above, there was no observable shift of the PL maximum for narrow QWs. Meanwhile, our study of the PL intensity dependence on excitation power density at different temperatures evidences considerable localization. Useful information can be obtained from the analysis of the excitation-induced change of the PL efficiency defined as the ratio of the PL intensity to the excitation intensity. The PL efficiency is different at low and elevated temperatures [see Fig. 5.8(a) and (b) for 8 K and room temperature, respectively]. The observed dependences cannot be explained merely by the built-in electric field screening effect, which should increase the PL efficiency with increasing carrier density up to the total screening of the built-in field. At low temperatures, the PL efficiency is independent on excitation at low excitation intensities and starts to drop at higher pumping. The critical excitation power density for the drop to occur shifts to higher values as the well width becomes narrower. This drop can be explained by increasing population of the lowest localized states, where carriers (excitons) cannot move. With increasing excitation power density, these deepest localized states are gradually filled in, and an increasing number of delocalized states becomes populated. The delocalized carriers reach the nonradiative recombination centers and recombine there nonradiatively. Such a delocalization is more pronounced in wider QWs, where the localization is weaker, as shown by the time-resolved PL study discussed in section 5.1. The localization depth difference in wide and narrow QWs was also confirmed by the PL intensity dependences on temperature as shown in Fig. 5.10. From the Arrhenius plots, the localization depths were estimated by using the expression of single thermally-activated channel:

$$I_{LUM}(T) = \frac{I_0}{1 + C\exp\left(-\frac{E_A}{kT}\right)}, \tag{5.2}$$

where I_0 is the intensity at low temperatures, E_A – localization depth, and C is the adjustable parameter. The best fits are shown by solid lines in Fig. 5.10, and the estimated localization depth energies were equal to 48 meV and 85 meV for 5.0 nm and 2.5 nm QWs, respectively, indicating an increase of localization depth for narrower QWs.

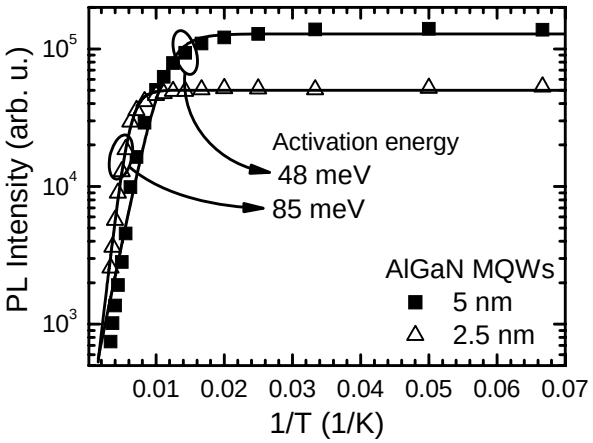

Fig. 5.10. The PL intensity dependence on inverse temperature for two AlGaN/AlGaN MQWs structures with different well widths (indicated). The solid lines show the best fit by Eq. (5.2). Estimated activation energies are indicated.

The room temperature PL efficiency results show a considerable decrease of the PL efficiency, which is probably caused by thermal delocalization and increasing contribution of nonradiative recombination. The effect is more pronounced for wider QWs [see Fig. 5.8(b)]. With temperature increase from 8 K to 300 K, the PL efficiency at low excitation power densities decreases approximately by factors of 50 and 10 for 5 nm and 2.5 nm-wide QWs, respectively. This is an indication that certain fraction of localized carriers still exists even at room temperature and the number of the localized carriers is larger in narrower QWs (again confirmed by PL intensity temperature dependences shown in Fig. 5.10, since the obtained localization depths are larger than kT at room temperature). The increase in the PL efficiency experimentally observed with increasing excitation power density at room temperature can be explained both by the saturation of the nonradiative recombination centers, which determines decrease of the nonradiative recombination rate, as well as by screening, which results in an increase of the radiative recombination rate. However, the latter effect should be less important at low excitation power densities and narrower QWs.

The observed decrease of the PL efficiency at excitation power densities above ~100 kW/cm^2 is difficult to interpret unambiguously. One of the

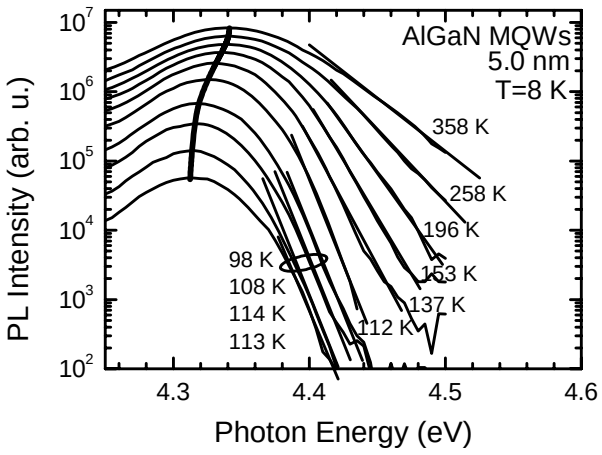

Fig. 5.11. PL spectra of AlGaN/AlGaN MQW structure with 5.0 nm width wells at 8 K temperature. Carrier temperatures estimated from the high-energy slope (solid lines) are indicated.

possible explanations of this decrease might be carrier heating. The heating has some experimental evidence: at elevated excitation power densities we observe a decrease in the high-energy slope of the PL band (see Fig. 5.6), which is a strong indication of the heating effect in the carrier system. It is generally believed that the carriers are captured at the nonradiative recombination center via a potential barrier. The probability of such a capture exponentially increases with temperature.

The carrier temperature was estimated from the high-energy slope of the PL band as shown in Fig. 5.11. At low excitation power densities, the slope corresponded to temperature, which was higher than the ambient temperature, indicating a PL band broadening due to localization. With increase of excitation power density above ~100 kW/cm^2, the carrier temperature starts also increasing, indicating carrier

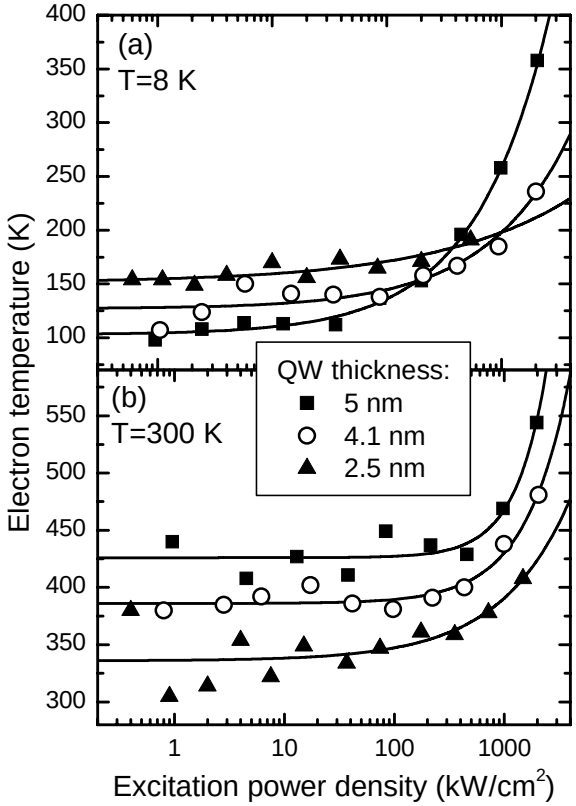

Fig. 5.12. Dependence of carrier temperature on excitation power density for AlGaN MQWs with different well width (indicated) at T = 8 K (a) and 300 K (b). Carrier temperatures were estimated from high-energy slope of PL spectra as shown in Fig. 5.11. Solid lines show the polynomial fit.

heating. As shown in Fig. 5.12 for wide and narrow QWs, the temperature increase is higher for wider QWs; however, the effect of the carrier heating in broad QWs might be compensated by screening effect, which increases the PL efficiency.

The obtained experimental results show that the carrier localization is quite strong in the QWs under study, especially at low temperatures. Filling-in of the localized states under increasing excitation power density should increase the blue shift of the PL band. However, the absence of this shift in narrow QWs, as well as low value of the built-in electric field extracted from fitting of theoretical and experimental data point out to other effects partially compensating the blue shift caused by screening and band-tail filling. One of the possible mechanisms of a decreased built-in field might be band gap renormalization (BGR) due to many-body interactions. The red shift due to BGR was approximately estimated by using the expression for bulk crystals [156]:

$$\Delta E_g = E_{ex}^b \cdot \left\{ \left[1 - \frac{1}{g} \right] \cdot \left[\Theta(1-g) + \left[1 - \frac{1}{g} \right] \cdot \Theta(g-1) \right] - 1 \right\}. \qquad (5.3)$$

Here E_{ex}^b is the exciton binding energy, $\Theta(x)$ is the Heaviside function. The parameter $g = 12/\left(\pi^2 a_B \kappa\right)$, where a_B is the exciton Bohr radius, is determined by the inverse screening length $\kappa = \sqrt{2e^2 n/\varepsilon\varepsilon_0 kT_c}$, where n is the carrier density and T_c is the carrier temperature.

The calculated PL band shift due to BGR is shown in Fig. 5.13. In the calculations, the exciton binding energy was equal to 35 meV, the

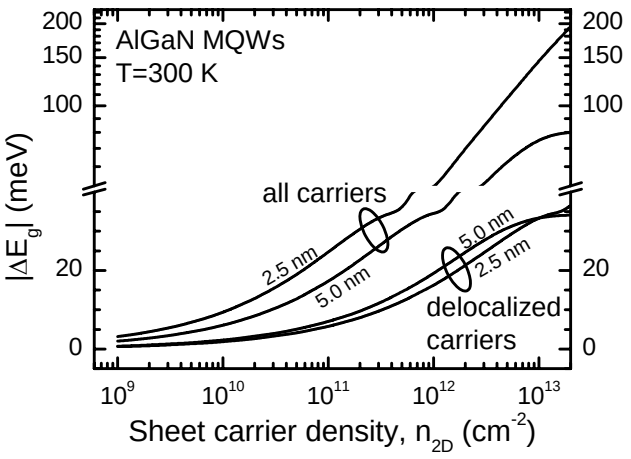

Fig. 5.13. Sheet carrier density dependence of the absolute value of the PL band red shift due to band gap renormalization at room temperature for two AlGaN/AlGaN MQW structures (indicated). Two cases were considered: i) BGR is caused by all photogenerated carriers; ii) BGR is caused only by delocalized carriers.

Bohr radius $a_B = 25$ Å, while the carrier temperature was taken from the polynomial approximation of experimentally obtained carrier temperature (shown by solid lines in Fig. 5.12). Under the assumption that all photogenerated carriers interact and cause BGR, the calculated red shift was very large. For narrow QWs it was even larger than the blue shift due to the field screening. Meanwhile, the large localization depth (see Fig. 5.10) means that a large part of photogenerated carriers is localized even at room temperature. Therefore, it is reasonable to assume that only free carriers cause BGR. The ratio of free and localized carriers was taken as $n_{free}/n_{loc} = \exp\left(-E_A/kT\right)$. The red shift due to BGR calculated for this case is also shown in Fig. 5.13.

The overall PL band shift, thus, occurs due to the sum of contributions from three effects: i) screening of built-in electric field (calculated by simultaneously solving Schrödinger and Poisson equations); ii) carrier heating (can be evaluated by expression $\Delta E_g = k\left(T_c - T_0\right)/2$, where T_0 is the carrier temperature at low excitation); and iii) band gap renormalization [calculated using Eq. (5.3)]. The calculated overall PL band shift for narrow and wide QWs is shown in Fig. 5.14. As can be clearly seen, the inclusion of many-body effects still cannot adequately describe the experimentally observed PL band shift. Consequently, other explanations of small PL band blue shift must be sought. The possible explanations might include the inaccurate material parameters available for AlGaN heterostructures. Another possible mechanism of a decreased built-in field might be related to small-scale composition fluctuations in the layer plane. Such fluctuations might cause carrier localization, and the localization might decrease the built-in electric field due to in-plane spreading of the electric field lines outside the localization area. A rough estimate based on results reported for grained nitride materials [157] shows that the field reduction by a factor of two or so might occur due to this effect.

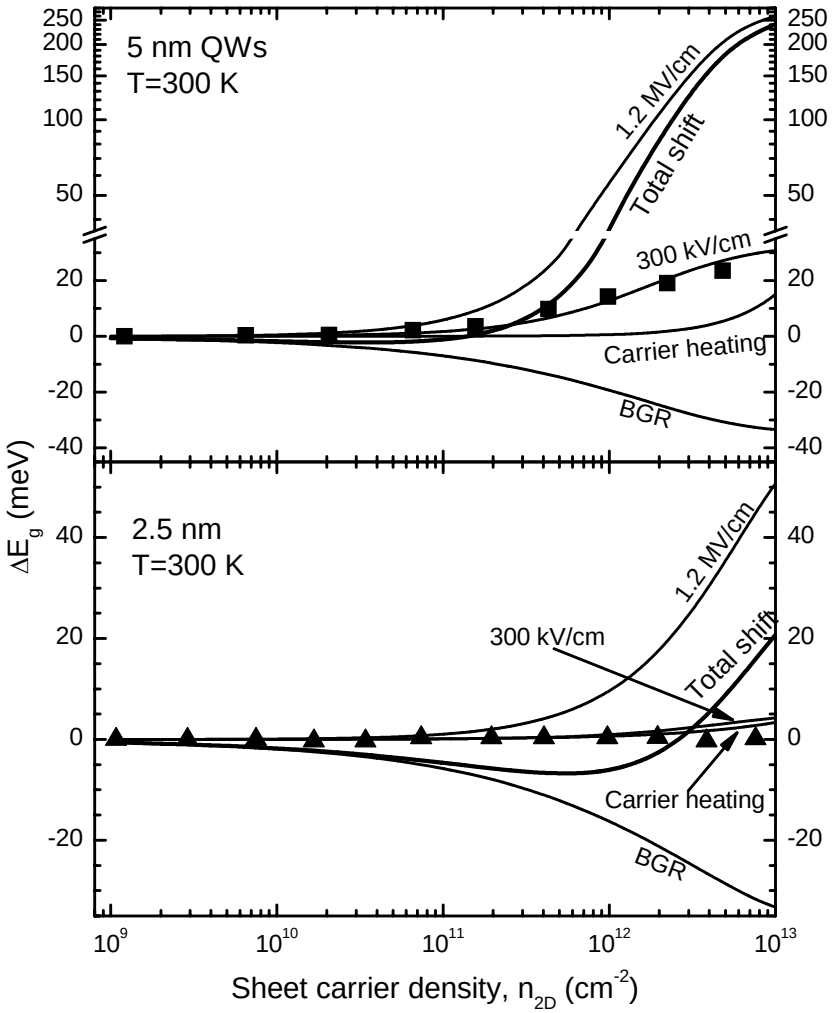

Fig. 5.14. Dependence of total peak shift on sheet carrier density for AlGaN/AlGaN MQWs with 5.0 nm (a) and 2.5 nm (b) well widths. Contributions from different effects are indicated (see text for more details).

To summarize, we have investigated AlGaN-based MQWs with different well width by combining excitation-dependent PL spectroscopy results and PL efficiency analysis, as well as theoretical modeling. The study showed that PL dynamics is strongly determined by localization of carriers (excitons), however, the processes of competition between radiative and nonradiative recombination, localization and release of carriers from localized states are complicated and depend on temperature, carrier density, well thickness, built-in electric field, and its screening. The PL under strong excitation gives evidence for involvement of filling-in of the local states by carriers and screening of the built-in electric field. The experimentally observed blue shift of the PL band due to increasing carrier density is considerably smaller than

that obtained by calculations. The many-body effects such as carrier heating and band gap renormalization cannot explain the small blue shift, and it might be interpreted by diminished built-in field due to in-plane spreading of the electric field outside the localization area.

5.3. Short summary

1. The fast initial component in PL intensity decay of AlGaN/AlGaN MQWs is caused by vanishing screening of the built-in electric field, which recovers with decreasing nonequilibrium carrier density.
2. The lifetime of carriers localized in narrow AlGaN/AlGaN MQWs decreases with increasing well width due to decreasing potential fluctuations causing the carrier localization.
3. The PL dynamics under strong excitation gives evidence for involvement of filling-in of the local states by carriers and screening of the built-in electric field. The best fit of the calculation blue shift of the PL band to the shift observed experimentally yielded the value of 300 kV/cm, which was considerably lower than that obtained from material parameters (1.2 MV/cm).

Concluding summary

1. The correlation between the carrier lifetime and intensity of the defect-related luminescence bands (YL and BL) implies that structural defects bound into complexes with impurities might be responsible for both the radiative recombination resulting in YL and for the nonradiative recombination limiting the carrier lifetime.
2. The comparison of TRPL and LITG results provides a new insight into the interpretation of the room temperature PL decay: fitting of the decay by two exponents corresponding to the carrier lifetime and to one-half of it is suggested as means to extract the carrier lifetime from the TRPL measurements.
3. The simultaneous determination of the carrier lifetime and of the diffusion coefficient showed that, in the GaN samples with similar dislocation densities, higher carrier mobility shortens the carrier lifetime, since the carriers reach the dislocations faster.
4. The FDLM technique enabled us to study the carrier dynamics at an extremely low excitation power density (~0.5 mW/cm^2) and to reveal the competition between recombination mechanisms responsible for YL in GaN at nonequilibrium carrier densities below the saturation of the energy levels involved.
5. High optical gain coefficient values up to ~7500 cm^{-1} have been observed in high-quality GaN epilayers both for light propagating perpendicular and parallel to the **c** axis. Gain saturation limits the applicability of the VSL technique for studies of very high gains, however, the VSL technique is useful for comparison of different GaN samples.
6. The PL, LITG, and etch pit results for AlGaN layers with different Al content shows that the carrier lifetime in AlGaN is primarily limited by

the carrier diffusion to the dislocations, where the nonradiative recombination occurs. The radiative recombination proceeds at the same rate in AlGaN samples with the same Al content (but different dislocation densities) and decreases with increasing Al content.

7. A quantitative description of PL linewidth in AlGaN alloy was achieved by using Monte Carlo simulations by introduction of double-scaled potential profile model. The excitons hop within the random potential fluctuations (on the scale σ) in the isolated low-band-gap regions dispersed in the average localization energy (on the scale Γ). Most likely, these regions have a lower Al content. Both potential profile scales were found to be similar ($\sigma \approx \Gamma \approx 19$ meV) and independent of the growth technique. A six-fold increase of carrier lifetime in MEMOCVD^{TM}-grown AlGaN epilayer is caused not by potential fluctuations, but by a reduced density of nonradiative recombination centers.
8. The fast initial component in PL intensity decay of AlGaN/AlGaN MQWs is caused by vanishing screening of the built-in electric field, which recovers with decreasing nonequilibrium carrier density. The slow decay component is determined by recombination of localized carriers with the localization occuring due to well width fluctuations. The lifetime of carriers localized in narrow AlGaN/AlGaN MQWs decreases with increasing well width due to decreasing potential fluctuations causing the carrier localization.
9. The PL dynamics under strong excitation gives evidence for involvement of filling-in of the local states by carriers and screening of the built-in electric field. The best fit of the calculation blue shift of the PL band to the shift observed experimentally yielded the value of 300 kV/cm, which was considerably lower than that obtained from material parameters (1.2 MV/cm).
10. MEMOCVD^{TM} growth technique enabled: i) the growth of high-quality GaN epilayers with dislocation densities as low as 10^8 cm^{-2}, exhibiting

carrier lifetimes at room temperature up to 2 ns, and optical gain values as high as ~7500 cm^{-1}; and ii) an increase of the PL intensity (by a factor of 6) and of carrier lifetime (by a factor of 6.5) for the AlGaN epilayers grown on sapphire substrates, compared to the epilayers grown by conventional MOCVD.

References

[1] W.Utsumi, H.Saitoh, H.Kaneko, T.Watanuki, K.Aoki, and O.Shimomura, Nature Materials 2, 735 (2003).

[2] I.Grzegory, M.Bockowski, B.Lucznik, S.Krukowski, Z.Romanowski, M.Wroblewski, and S.Porowski, J. Crystal Growth 246, 177 (2002).

[3] M.Bockowski, Cryst. Res. Technol. 42, 1162 (2007).

[4] J.C.Rojo, G.A.Slack, K.Morgan, B.Raghothamachar, M.Dudley, and L.J.Schowalter, J. Crystal Growth 231, 317 (2001).

[5] R.T.Bondokov, S.G.Mueller, K.E.Morgan, G.A.Slack, S.Schujman, M.C.Wood, J.A.Smart, and L.J.Schowalter, J. Crystal Growth 310, 4020 (2008).

[6] E.J.Thrush and A.R.Boyd, in *III Nitride Semiconductor Materials*, edited by Z.C.Feng (Imperial College Press, London, 2006), pp.73-116.

[7] H.Amano, N.Sawaki, I.Akasaki, and T.Toyoda, Appl. Phys. Lett. 48, 353 (1986).

[8] P.Gibart, Rep. Prog. Phys. 67, 667 (2004).

[9] M.A.Khan, M.Shatalov, H.P.Maruska, H.M.Wang, and E.Kuokstis, Jpn. J. Appl. Phys. 44, 7191 (2005).

[10] S.Kamiyama, M.Iwaya, N.Hayashi, T.Takeuchi, H.Amano, I.Akasaki, S.Watanabe, Y.Kaneko, and N.Yamada, J. Crystal Growth 223, 83 (2001).

[11] J.Han, K.E.Waldrip, S.R.Lee, J.J.Figiel, S.J.Hearne, G.A.Petersen, and S.M.Myers, Appl. Phys. Lett. 78, 67 (2001).

[12] A.D.Bykhovski, B.L.Gelmont, and M.S.Shur, J. Appl. Phys. 81, 6332 (1997).

[13] J.P.Zhang, H.M.Wang, M.E.Gaewski, C.Q.Chen, Q.Fareed, J.W.Yang, G.Simin, and M.A.Khan, Appl. Phys. Lett. 80, 3542 (2002).

[14] M.A.Khan, R.A.Skogman, J.M.Van Hove, D.T.Olson, and J.N.Kuznia, Appl. Phys. Lett. 60, 1366 (1992).

[15] M.A.Khan, J.N.Kuznia, R.A.Skogman, D.T.Olson, M.MacMillan, and W.J.Choyke, Appl. Phys. Lett. 61, 2539 (1992).

[16] R.S.Qhalid Fareed, R.Jain, R.Gaska, M.S.Shur, J.Wu, W.Walukiewicz, and M.A.Khan, Appl. Phys. Lett. 84, 1892 (2004).

[17] J.Zhang, X.Hu, A.Lunev, J.Deng, Y.Bilenko, T.M.Katona, M.S.Shur, R.Gaska, and M.A.Khan, Jpn. J. Appl. Phys. 44, 7250 (2005).

[18] Q.Fareed, R.Gaska, and M.S.Shur, Methods of Growing Nitride-Based Film Using Varying Pulses, US patent 7,192,849, March 20 (2007).

[19] R.Jain, W.Sun, J.Yang, M.Shatalov, X.Hu, A.Sattu, A.Lunev, J.Deng, I.Shturm, Y.Bilenko, R.Gaska, and M.S.Shur, Appl. Phys. Lett. 93, 051113 (2008).

[20] J.H.Edgar (ed), *Properties of Group III Nitrides* (EMIS Datareviews Series 11) (INSPEC, IEE, London, 1994).

[21] I.Vurgaftman, and J.R.Meyer, J. Appl. Phys. 94, 3675 (2003).

[22] F.Bernardini, V.Fiorentini, and D.Vanderbilt, Phys. Rev. B 56, R10024 (1997).

[23] A.V.Rodina, M.Dietrich, A.Goldner, L.Eckey, A.Hoffmann, Al.L.Efros, M.Rosen, and B.K.Meyer, Phys. Rev. B 64, 115204 (2001).

[24] M.Suzuki, T.Uenoyama, A.Yanase, Phys. Rev. B 52, 8132 (1995).

[25] J.Li, K.B.Nam, M.L.Nakarmi, J.Y.Lin, H.X.Jiang, P.Carrier, and S.-H.Wei, Appl. Phys. Lett. 83, 5163 (2003).

[26] G.D.Chen, M.Smith, J.Y.Lin, H.X.Jiang, S.-H.Wei, M.A.Khan, and C.J.Sun, Appl. Phys. Lett. 68, 2784 (1996).

[27] K.B.Nam, J.Li, M.L.Nakarmi, J.Y.Lin, and H.X.Jiang, Appl. Phys. Lett. 84, 5264 (2004).

[28] D.Y.Fu, R.Zhang, B.G.Wang, Z.Zhang, B.Liu, Z.L.Xie, X.Q.Xiu, H.Lu, Y.D.Zheng, and G.Edwards, Appl. Phys. Lett. 94, 191907 (2009).

[29] S.Wieczorek, W.W.Chow, S.R.Lee, A.J.Fischer, A.A.Allerman, and M.H.Crawford, Appl. Phys. Lett. 84, 4899 (2004).

[30] R.G.Banal, M.Funato, and Y.Kawakami, Phys. Rev. B 79, 121308(R) (2009).

[31] B.Monemar, P.P.Paskov, J.P.Bergman, A.A.Toropov, and T.V.Shubina, phys. stat. sol. (b) 244, 1759 (2007).

[32] S.R.Lee, A.F.Wright, M.H.Crawford, G.A.Petersen, J.Han, and R.M.Biefeld, Appl. Phys. Lett. 74, 3344 (1999).

[33] K.B.Nam, J.Li, K.H.Kim, J.Y.Lin, and H.X.Jiang, Appl. Phys. Lett. 78, 3690 (2001).

[34] E.Silveira, J.A.Freitas, Jr., O.J.Glembocki, G.A.Slack, and L.J.Schowalter, Phys. Rev. B 71, 041201(R) (2005).

[35] F.Bernardini and V.Fiorentini, Phys. Rev. B 64, 085207 (2001).

[36] V.Fiorentini, F.Bernardini, and O.Ambacher, Appl. Phys. Lett. 80, 1204 (2002).

[37] F.Bernardini, and V.Fiorentini, Phys. Rev. B 57, R9427 (1998).

[38] D.A.B.Miller, D.S.Chemla, T.C.Damen, A.C.Gossard, W.Wiegmann, T.H.Wood, and C.A.Burrus, Phys. Rev. Lett. 53, 2173 (1984); Phys. Rev. B 32, 1043 (1985).

[39] P.Lefebvre, J.Allegre, B.Gil, H.Mathieu, N.Grandjean, M.Leroux, J.Massies, and P.Bigenwald, Phys. Rev. B 59, 15363 (1999).

[40] V.Fiorentini, F.Bernardini, F.D.Sala, A.Di Carlo, and P.Lugli, Phys. Rev. B 60, 8849 (1999).

[41] E.Kuokstis, W.H.Sun, C.Q.Chen, J.W.Yang, and M.A.Khan, J. Appl. Phys. 97, 103719 (2005).

[42] A.Pinos, S.Marcinkevicius, K.Liu, M.S.Shur, E.Kuokstis, G.Tamulaitis, R.Gaska, J.Yang, and W.Sun, Appl. Phys. Lett. 92, 061907 (2008).

[43] R.Kajitani, K.Kawasaki, M.Takeuchi, Mat. Sc. and Eng. B 139, 186 (2007).

[44] M.D.Craven, P.Waltereit, J.S.Speck, and S.P.DenBaars, Appl. Phys. Lett. 84, 496 (2004).

[45] M.A.Reshchikov and H.Morkoc, J. Appl. Phys. 97, 061301 (2005).

[46] T.Ogino and M.Aoki, Jpn. J. Appl. Phys. 19, 2395 (1980).

[47] E.R.Glaser, T.A.Kennedy, K.Doverspike, L.B.Rowland, D.K.Gaskill, J.A.Freitas, Jr., M.A.Khan, D.T.Olson, J.N.Kuznia, and D.K.Wickenden, Phys.Rev. B 51, 13326 (1995).

[48] D.G.Chtchekine, L.P.Fu, G.D.Gilliland, Y,Chen, S.E.Ralph, K.K.Bajaj, Y.Bu, M.C.Lin, F.T.Bacalzo, and S.R.Stock, J. Appl. Phys 81, 2197 (1996).

[49] F.K.Koschnick, K.Michael, J.-M.Spaeth, B.Beaumont, and P.Gibart, Appl. Phys. Lett. 76, 1828 (2000).

[50] T.Lai, J.Wen, and W.Lin, Appl. Phys. Lett. 86, 041102 (2005).

[51] H.Wang and A.-B.Chen, J. Appl. Phys. 87, 7859 (2000).

[52] C.B.Soh, S.J.Chua, H.F.Lim, D.Z.Chi, S.Tripathy, and W.Liu, J. Appl. Phys. 96, 1341 (2004).

[53] J.Neugebauer, C.G.Van de Walle, Appl. Phys. Lett. 69, 503 (1996).

[54] L.Polenta, A.Castaldini, and A.Cavallini, J. Appl. Phys. 102, 063702 (2007).

[55] W.You, X.D.Zhang, L.M.Zhang, Z.Yang, H.Bian, Q.Ge, W.X.Guo, W.X.Wang, Z.M.Liu, Phys. B 403, 2666 (2008).

[56] R.Armitage, Q.Yang, and E.R.Weber, J. Appl. Phys. 97, 073524 (2005).

[57] A.Armstrong, A.R.Arehart, D.Green, U.K.Mishra, J.S.Speck, and S.A.Ringel, J. Appl. Phys. 98, 053704 (2005).

[58] A.Castaldini, A.Cavallini, and L.Polenta, Appl. Phys. Lett. 87, 122105 (2005).

[59] J.Elsner, R.Jones, M.I.Heggie, P.K.Sitch, M.Haugk, Th.Frauenheim, S.Oberg, and P.R.Briddon, Phys. Rev. B 58, 12571 (1998).

[60] D.G.Zhao, D.S.Jiang, H.Yang, J.J.Zhu, Z.S.Liu, S.M.Zhang, J.W.Liang, X.Li, X.Y.Li, and H.M.Gong, Appl. Phys. Lett. 88, 241917 (2006).

[61] G.Li, S.J.Chua, S.J.Xu, W.Wang, P.Li, B.Beaumont, and P.Gibart, Appl. Phys. Lett. 74, 2821 (1999).

[62] L.Macht, J.L.Weyher, A.Grzegorczyk, and P.K.Larsen, Phys. Rev. B 71, 073309 (2005).

[63] I.Yonenaga, H.Makino, S.Itoh, and T.Yao, phys. stat. sol. (c) 2, 1817 (2005).

[64] X.Li, P.W.Bohn, and J.J.Coleman, Appl. Phys. Lett. 75, 4049 (1999).

[65] R.Dingle, K.L.Shaklee, R.F.Leheny, and R.B.Zetterstrom, Appl. Phys. Lett. 19, 5 (1971).

[66] J.M.Hvam and E.Ejder, J. Lumin. 12/13, 611 (1976).

[67] R.Dai, W.Zhuang, K.Bohnert, and C.Klingshirn, Z. Phys. B: Condens. Matter 46, 189 (1982).

[68] I.M.Catalano, A.Cingolani, M.Ferrara, M.Lugara, and A.Minafra, Solid State Commun. 25, 349 (1978).

[69] S.Bidnyk, T.J.Schmidt, B.D.Little, and J.J.Song, Appl. Phys. Lett. 74, 1 (1999).

[70] W.D.Herzog, G.E.Bunea, M.S.Unlu, B.B.Goldberg, and R.J.Molnar, Appl. Phys. Lett. 77, 4145 (2000).

[71] K.Kazlauskas, G.Tamulaitis, A.Zukauskas, T.Suski, P.Perlin, M.Leszczynski, P.Prystawko, and I.Grzegory, Phys. Rev. B 69, 245316 (2004).

[72] R.A.Taylor, S.Hess, K.Kyhm, J.Smith, J.F.Ryan, G.P.Yablonskii, E.V.Lutsenko, V.N.Pavlovskii, and M.Heuken, phys. stat. sol. (b) 216, 465 (1999).

[73] O.Gluschekov, J.M.Myoung, K.H.Shim, K.Kim, Z.G.Figen, J.Gao, and J.G.Eden, Appl. Phys. Lett. 70, 811 (1996).

[74] T.Malinauskas, R.Aleksiejunas, K.Jarasiunas, B.Beaumont, P.Gibart, A.Kakanakova-Georgieva, E.Janzen, D.Gogova, B.Monemar, and M.Heuken, J. Crystal Growth 300, 223 (2007).

[75] K.Domen, K.Kondo, A.Kuramata, and T.Tanahashi, Appl. Phys. Lett. 69, 94 (1996).

[76] Y.Kawakami, Y.Narukawa, K.Omae, and S.Fujita, Appl. Phys. Lett. 77, 2151 (2000).

[77] K.Omae, Y.Kawakami, Y.Narukawa, Y.Watanabe, T.Mukai, and S.Fujita, phys. stat. sol. (a) 190, 93 (2002).

[78] B.W.Hakki and T.L.Paoli, J. Appl. Phys. 44, 4113 (1973).

[79] U.T.Schwarz, E.Sturm, W.Wegscheider, V.Kummler, A.Lell, and V.Harle, phys. stat. sol. (a) 200, 143 (2003).

[80] K.L.Shaklee, R.E.Nahory, and R.F.Leheny, J. Lumin. 7, 284 (1973).

[81] D.Wiesmann, I.Brener, L.Pfeiffer, M.A.Khan, and C.J.Sun, Appl. Phys. Lett. 69, 3384 (1996).

[82] P.Ramvall, Y.Aoyagi, A.Kuramata, P.Hacke, K.Domen, and K.Horino, Appl. Phys. Lett. 76, 2994 (2000).

[83] S.Jursenas, N.Kurilcik, G.Kurilcik, S.Miasojedovas, A.Zukauskas, T.Suski, P.Perlin, M.Leszczynski, P.Prystawko, and I.Grzegory, Appl. Phys. Lett. 85, 952 (2004).

[84] M.Vehse, P.Michler, O.Lange, M.Rowe, J.Gutowski, S.Bader, H.-J.Lugauer, G.Bruderl, A.Weimar, A.Lell, and V.Harle, Appl. Phys. Lett. 79, 1763 (2001).

[85] K.Kyhm, R.A.Taylor, J.F.Ryan, T.Someya, and Y.Arakawa, Appl. Phys. Lett. 79, 3434 (2001).

[86] M.Vehse, J.Meinertz, O.Lange, P.Michler, J.Gutowski, S.Bader, A.Lell, V.Harle, phys. stat. sol. (c) 0, 43 (2002).

[87] S.F.Chichibu et al., Appl. Phys. Lett. 74, 1460 (1999).

[88] R.Y.Korotkov, M.A.Reshchikov, and B.W.Wessels, Physica B 325, 1 (2003).

[89] D.G.Thomas, J.J.Hopfield, and W.M.Augustyniak, Phys. Rev. 140, A202 (1965).

[90] R.Y.Korotkov, M.A.Reshchikov, and B.W.Wessels, Physica B 273-274, 80 (1999).

[91] B.Monemar, P.P.Paskov, J.P.bergman, A.A.Toropov, T.V.Shubina, T.Malinauskas, and A.Usui, phys. stat. sol. (b) 245, 1723 (2008).

[92] J.S.Im, A.Moritz, F.Steuber, V.Harle, F.Scholz, and A.Hangleiter, Appl. Phys. Lett. 70, 631 (1997).

[93] A.V.Sampath, G.A.Garrett, C.J.Collins, P.Boyd, J.Choe, P.G.Newman, H.Shen, M.Wraback, R.J.Molnar, and J.Caissie, J. Vac. Sci. Technol. B 22, 1487 (2004)

[94] G.E.Bunea, W.D.Herzog, M.S.Unlu, B.B.Goldberg, and R.J.Molnar, Appl. Phys. Lett. 75, 838 (1999).

[95] H.K.Kwon, C.J.Eiting, D.J.H.Lambert, M.M.Wong, R.D.Dupuis, Z.Liliental-Weber, and M.Benamara, Appl. Phys. Lett. 77, 2503 (2000).

[96] T.Izumi, Y.Narukawa, K.Okamoto, Y.Kawakami, Sg.Fujita, and S.Nakamura, J. Lumin. 87-89, 1196 (2000).

[97] S.Jursenas, N.Kurilcik, G.Kurilcik, A.Zukauskas, P.Prystawko, M.Leszcynski, T.Suski, P.Perlin, I.Grzegory, and S.Porowski, Appl. Phys. Lett. 78, 3776 (2001).

[98] U.Ozgur, X.Ni, Y.Fu, H.Morkoc, and H.O.Everitt, Appl. Phys. Lett. 89, 262117 (2006).

[99] S.Jursenas, S.Miasojedovas, and A.Zukauskas, J. Crystal Growth 281, 161 (2005).

[100] S.F.Chichibu, A.Uedono, T.Onuma, T.Sota, B.A.Haskell, S.P.DenBaars, J.S.Speck, and S.Nakamura, Appl. Phys. Lett. 86, 021914 (2005).

[101] T.Malinauskas, K.Jarasiunas, S.Miasojedovas, S.Jursenas, B.Beaumont, and P.Gibart, Appl. Phys. Lett. 88, 202109 (2006).

[102] S.Miasojedovas, M.Butkus, S.Jursenas, B.Lucznik, I.Grzegory, and T.Suski, Micron 40, 118 (2009).

[103] U.Ozgur, Y.Fu, Y.T.Moon, F.Yun, H.Morkoc, H.O.Everitt, S.S.Park, and K.Y.Lee, Appl. Phys. Lett. 86, 232106 (2005).

[104] S.Jursenas, S.Miasojedovas, A.Zukauskas, B.Lucznik, I.Grzegory, and T.Suski, Appl. Phys. Lett. 89, 172119 (2006).

[105] J.Xie, U.Ozgur, Y.Fu, X.Ni, H.Morkoc, C.K.Inoki, T.S.Kuan, J.V.Foreman, and H.O.Everitt, Appl. Phys. Lett. 90, 041107 (2007).

[106] E.Kuokstis, G.Tamulaitis, K.Liu, M.S.Shur, J.W.Li, J.W.Yang, and M.A.Khan, Appl. Phys. Lett. 90, 161920 (2007).

[107] S.Chichibu, T.Azuhata, T.Sota, and S.Nakamura, Appl. Phys. Lett. 69, 4188 (1996).

[108] T.Takayama, M.Yuri, K.Itoh, and J.S.Harris, Jr., J. Appl. Phys. 90, 2358 (2001).

[109] J.Adhikari and D.A.Kofke, J. Appl. Phys. 95, 6129 (2004).

[110] L.Chang, S.K.Lai, F.R.Chen, and J.J.Kai, Appl. Phys. Lett. 79, 928 (2001).

[111] G.Steude, B.K.Meyer, A.Goldner, A.Hoffmann, F.Bertram, J.Christen, H.Amano, and I.Akasaki, Appl. Phys. Lett. 74, 2456 (1999).

[112] M.Gao, S.T.Bradley, Y.Cao, D.Jena, Y.Lin, S.A.Ringel, J.Hwang, W.J.Schaff, and L.J.Brillson, J. Appl. Phys. 100, 103512 (2006).

[113] Y.-H.Cho, G.H.Gainer, J.B.Lam, J.J.Song, W.Yang, and W.Jhe, Phys. Rev. B 61, 7203 (2000).

[114] H.S.Kim, R.A.Mair, J.Li, J.Y.Lin, and H.X.Jiang, Appl. Phys. Lett. 76, 1252 (2000).

[115] A.Bell, S.Srinivasan, C.Plumlee, H.Omiya, F.A.Ponce, J.Christen, S.Tanaka, A.Fujioka, and Y.Nakagawa, J. Appl. Phys. 95, 4670 (2004).

[116] E.Kuokstis, W.H.Sun, M.Shatalov, J.W.Yang, and M.A.Khan, Appl. Phys. Lett. 88, 261905 (2006).

[117] N.Nepal, J.Li, M.L.Nakarmi, J.Y.Lin, and H.X.Jiang, Appl. Phys. Lett. 88, 062103 (2006).

[118] H.Murotani, Y.Yamada, Y.Taguchi, A.Ishibashi, Y.Kawaguchi, and T.Yokogawa, J. Appl. Phys. 104, 053514 (2008).

[119] J.Li, K.B.Nam, J.Y.Lin, and H.X.Jiang, Appl. Phys. Lett. 79, 3245 (2001).

[120] T.Onuma, S.F.Chichibu, A.Uedono, T.Sota, P.Cantu, T.M.Katona, J.F.Keading, S.Keller, U.K.Mishra, S.Nakamura, and S.P.DenBaars, J. Appl. Phys. 95, 2495 (2004).

[121] H.Murotani, T.Saito, N.Kato, Y.Yamada, T.Taguchi, A.Ishibashi, Y.Kawaguchi, T.Yokogawa, Appl. Phys. Lett. 91, 231910 (2007).

[122] S.Marcinkevicius, A.Pinos, K.Liu, D.Veksler, M.S.Shur, J.Zhang, and R.Gaska, Appl. Phys. Lett. 90, 081914 (2007).

[123] R.Kajitani, M.Takeuchi, and Y.Aoyagi, Jpn. J. Appl. Phys 47, 47 (2008).

[124] H.Murotani, T.Saito, N.Kato, Y.Yamada, and T.Taguchi, phys. stat. sol. (c) 5, 2274 (2008).

[125] A.Miller, in *Nonlinear Optics in Semiconductors II, Semiconductors and Semimetals*, edited by E.Garmire and A.Kost (Academic, New York, 1999), Vol. 59, Chap. 5, pp. 287, 292.

[126] J.R.Lakowicz, *Principles of Fluorescence Spectroscopy*, Kluwer Academic, Plenum, New York, 1999.

[127] S.Sakalauskas and A.Sodeika, Rev. Sci. Instrum. 69, 466 (1998).

[128] G.Koley and M.G.Spencer, J. Appl. Phys. 90, 337 (2001).

[129] G.Tamulaitis, A.Zukauskas, J.W.Yang, M.A.Khan, M.S.Shur, and R.Gaska, Appl. Phys. Lett. 75, 2277 (1999).

[130] J.Y.Duboz, J. Appl. Phys. 92, 4312 (2002).

[131] S.Jursenas, S.Miasojedovas, G.Kurilcik, A.Zukauskas, and P.R.Hageman, Appl. Phys. Lett. 83, 66 (2003).

[132] O.Brandt, H.Yang, and K.H.Ploog, Phys. Rev. B 54, R5215 (1996).

[133] Y.-H.Kwon, S.K.Shee, G.H.Gainer, G.H.Park, S.J.Hwang, and J.J.Song, Appl. Phys. Lett. 76, 840 (2000).

[134] M.A.Reshchikov, M.Zafar Iqbal, H.Morkoc, S.S.Park, and K.Y.Lee, Appl. Phys. Lett. 83, 266 (2003).

[135] M.A.Reshchikov, H.Morkoc, S.S.Park, K.Y.Lee, Appl. Phys. Lett. 78. 2882 (2001).

[136] D.C.Reynolds, D.C.Look, B.Jogai, A.W.Saxler, S.S.Park, and J.Y.Hahn, Appl. Phys. Lett. 77, 2879 (2000).

[137] H.Wang, J.Zhang, C.Chen, Q.Fareed, J.Yang, and M.A.Khan, Appl. Phys. Lett. 81, 604 (2002).

[138] J.Barjon, J.Brault, B.Daudin, D.Jalabert, and B.Sieber, J. Appl. Phys. 94, 2755 (2003).

[139] W.R.Harding, I.D.Blenkinsop, and D.R.Wright, Electron. Lett. 12, 502 (1976).

[140] Z.Z.Bandic, P.M.Bridger, E.C.Piquette, and T.C.McGill, Solid-State Electron. 44, 221 (2000).

[141] L.Chernyak, A.Osinsky, and A.Schulte, Solid-State Electron. 45, 1687 (2001).

[142] M.Albrecht, H.P.Strunk, J.L.Weyher, I.Grzegory, S.Porowski, and T.Wosinski, J. Appl. Phys. 92, 2000 (2002).

[143] M.Albrecht, A.Cremades, J.Krinke, S.Christiansen, O.Ambacher, J.Piqueras, H.P.Strunk, and M.Stutzmann, phys. stat. sol. (b) 216, 409 (1999).

[144] A.Cremades, M.Albrecht, J.Krinke, R.Dimitrov, M.Stutzmann, and H.P.Strunk, J. Appl. Phys. 87, 2357 (2000).

[145] A.Dmitriev and A.Oruzheinikov, J. Appl. Phys. 86, 3241 (1999).

[146] K.Kazlauskas, G.Tamulaitis, P.Pobedinskas, A.Zukauskas, M.Springis, C.-F.Huang, Y.-C.Cheng, and C.C.Yang, Phys. Rev. B 71, 085306 (2005).

[147] K.Kazlauskas, G.Tamulaitis, A.Zukauskas, M.A.Khan, J.W.Yang, J.Zhang, G.Simin, M.S.Shur, and R.Gaska, Appl. Phys. Lett. 83, 3722 (2003).

[148] Y.-H.Cho, G.H.Gainer, J.B.Lam, J.J.Song, and W.Yang, phys. stat. sol. (a) 188, 815 (2001).

[149] P.Lefebvre, S.Anceau, P.Valvin, T.Taliercio, L.Konczeiwcz, T.Suski, S.P.Lepkowski, H.Teisseyre, H.Hirayama, and Y.Aoyagi, Phys. Rev. B 66, 195330 (2002).

[150] X.H.Zhang, W.Liu, and S.J.Chua, J. Cryst. Growth 268, 521 (2004).

[151] K.C.Zeng, J.Li, J.Y.Lin, and H.X.Jiang, Appl. Phys. Lett. 76, 3040 (2000).

[152] P.G.Eliseev, P.Perlin, J.Lee, and M.Osinski, Appl. Phys. Lett. 71, 569 (1997).

[153] T.Y.Lin, J.C.Fan, and Y.F.Chen, Semicond. Sci. Technol. 14, 406 (1999).

[154] F.Della Sala, A.Di Carlo, P.Lugli, F.Bernardini, V.Fiorentini, R.Scholz, and J.-M.Jancu, Appl. Phys. Lett. 74, 2002 (1999).

[155] A.Zukauskas, *Puslaidininkiniai šviestukai* (in Lithuanian) (Progretus, Vilnius, 2008), p.85.

[156] L.Banyai and S.W.Koch, Z. Phys. B 63, 283 (1986).

[157] V.Yu.Kachorovskii and M.S.Shur, Appl. Phys. Lett. 86, 012101 (2005).